Pontifícia Universidade Católica
do Rio de Janeiro

Thiago Fabricius Konopka

Two-Phase Flow Modeling in Highly Heterogeneous Porous Media Using Brinkman Equation and Single and Dual continuum Darcy Models

Tese de Doutorado

Thesis presented to the Programa de Pós–graduação em Pós-Graduação em Engenharia Mecânica, do Departamento de Engenharia Mecânica da PUC-Rio in partial fulfillment of the requirements for the degree of Doutor em Pós-Graduação em Engenharia Mecânica.

Advisor: Prof. Dr. Márcio da Silveira Carvalho

Rio de Janeiro
April 2024

Pontifícia Universidade Católica
do Rio de Janeiro

Thiago Fabricius Konopka

Two-Phase Flow Modeling in Highly Heterogeneous Porous Media Using Brinkman Equation and Single and Dual continuum Darcy Models

Thesis presented to the Programa de Pós–graduação em Pós-Graduação em Engenharia Mecânica da PUC-Rio in partial fulfillment of the requirements for the degree of Doutor em Pós-Graduação em Engenharia Mecânica. Approved by the Examination Committee:

Prof. Dr. Márcio da Silveira Carvalho
Advisor
Departamento de Engenharia Mecânica – PUC-Rio

Prof. Dr. Ivan Fabio Mota de Menezes
Departamento de Engenharia Mecânica – PUC-Rio

Dr. Eng. José Sérgio de Araújo Cavalcante Filho
Petrobras

Prof. Dr. Marcio Arab Murad
LNCC

Dr. Eng. Marcos Vitor Barbosa Machado
Petrobras

Rio de Janeiro, April the 2nd, 2024

Thiago Fabricius Konopka

Graduou-se em Engenharia Mecânica pela Universidade Federeal do Paraná. Fez mestrado no Departamento de Engenharia de Mecânica da PUC-Rio, com Especialização em Sistemas Térmicos. Fez Doutorado no Departamento de Engenharia de Mecânica da PUC-Rio, especializando em Petróleo e Energia. Atualmente é Engenheiro de Reservatórios da Petrobras.

Bibliographic data

Konopka, Thiago Fabricius

Two-Phase Flow Modeling in Highly Heterogeneous Porous Media Using Brinkman Equation and Single and Dual continuum Darcy Models / Thiago Fabricius Konopka; advisor: Márcio da Silveira Carvalho. – 2024.

179 f: il. color. ; 30 cm

Tese (doutorado) - Pontifícia Universidade Católica do Rio de Janeiro, Departamento de Engenharia Mecânica, 2024.

Inclui bibliografia

1. Engenharia Mecânica – Teses.
2. Modelo de Brinkman. 3. Escoamento bifásico. 4. Curvas de permeabilidade relativa equivalente. 5. Macroposidades. 6. Upscale. I. Carvalho, Márcio da Silveira. II. Pontifícia Universidade Católica do Rio de Janeiro. Departamento de Engenharia Mecânica. III. Título.

CDD: 621

A minha esposa Sindy e a minha filha Helena,
sem o carinho, amor e compreensão de vocês,
não teria chegado até aqui.

Acknowledgments

First and foremost, this work could not have been performed without the unconditional dedication of my wife Sindy, who has always supported and encouraged me throughout this journey. To my daughter Helena, who is the light of my life and inspires and encourages me to continue on my journey. It was difficult for me to trade living with you for dedicating myself to this work. This thesis is dedicated to you two, my dearest loves.

My parents, Irene and Gilberto (*in memoriam*), who had the most important responsibility of educating and guiding me throughout my life. My success would not have been possible without their support and encouragement.

My sincere thanks go to Norma and Wilson for their encouragement and support over the years.

I would like to thank my advisor, Prof. Marcio Carvalho, for his dedication and partnership throughout this study. I wish I had the same enthusiasm for science and engineering as you do. My sincere thanks go out to the LMMP team, especially Monique Feitosa, who helped me with the code several times.

In appreciation of the opportunity provided by PUC-Rio as well as the assistance provided, without which this work would not have been possible. My sincere gratitude goes out to the professors who have taught me valuable lessons and contributed to my education. Additionally, I would like to thank the entire administration team of this institution.

My sincere thanks go out to all the teachers who have influenced me throughout my life. All of them have contributed to paving the way for today. None of this would be possible without them.

I would like to thank Petrobras for the partial release necessary to attend this graduate course, as well as my managers Daniel Dargan and João Henrique for their continued support. Additionally, I would like to thank Andre Modenessi for the discussions and assistance with developing the models at CMOST, as well as Tiago Amorin for his suggestions for improving the work. In addition, I wish to thank my Sépia teammates. Guilherme has made a significant contribution to my development as a reservoir engineer over the last five years. I would also like to thank the geologists Alexandre, Midori, Renato, Mellissa, and Caroline for their valuable lectures on the geology of carbonate reservoirs. These discussions provided special insight into this study. In addition, I would like to thank Luiz Antonio, Marinho, Pedro, Giselle, Olivia, Stella, and Paula for their valuable daily discussions. Special thanks to my friend, Leonardo Murilo Nepomuceno.

This study was financed in part by the Coordenação de Aperfeiçoamento de Pessoal de Nível Superior - Brasil (CAPES) - Finance Code 001.

Abstract

Konopka, Thiago Fabricius; Carvalho, Márcio da Silveira (Advisor). **Two-Phase Flow Modeling in Highly Heterogeneous Porous Media Using Brinkman Equation and Single and Dual continuum Darcy Models**. Rio de Janeiro, 2024. 179p. Tese de Doutorado – Departamento de Engenharia Mecânica, Pontifícia Universidade Católica do Rio de Janeiro.

Multiphase flow in highly heterogeneous porous media holds substantial importance in the petroleum industry since there are large oil volumes in vuggy and fractured reservoirs. In this study, Brinkman equation is employed to model two-phase flow in highly heterogeneous porous media. Brinkman model represents flow dynamics through the porous matrix and vugs using a single differential equation without the need for interfacial conditions. However, accurately characterizing the vugular and porous matrix regions remains a challenging task, especially in reservoir-scale models that typically represent geological formations with large areas. Reservoir simulations often involve models discretized into computational cells, each with dimensions on the order of several meters that are not fine enough do describe in detail the geometry of the vugs and fractures embedded in the porous matrix. This investigation explores two distinct approaches for generating equivalent properties of vugular media. The first approach uses results from the Brinkman model to derive equivalent properties for the single-continuum Darcy model at the same level of discretization. The second approach employs upscaling by numerical optimization to generate equivalent properties on a coarse scale. This method is applied to both single-continuum and dual-continuum Darcy models. Single-continuum models can effectively describe vugular structures characterized by dispersed vugs in the porous matrix without strong fluid channeling. However, for systems exhibiting substantial channeling, upscaling can only be achieved through dual-continuum models. In both proposed approaches, the determination of equivalent absolute permeability and equivalent absolute permeability curves is imperative for an efficient upscaling process.

Keywords

Brinkman model; Two-phase flow; Equivalent relative permeability curves; Macroporosity; Upscale.

Resumo

Konopka, Thiago Fabricius; Carvalho, Márcio da Silveira. **Modelagem de Fluxo Bifásico em Meios Porosos Altamente Heterogêneos Utilizando a Equação de Brinkman e os Modelos de Simples e Duplo Contínuo**. Rio de Janeiro, 2024. 179p. Tese de Doutorado – Departamento de Engenharia Mecânica, Pontifícia Universidade Católica do Rio de Janeiro.

O fluxo bifásico em meios porosos altamente heterogêneos possui grande importância na indústria do petróleo devido aos desafios apresentados pelas características de permeoporosidade, fraturas e cavidades incorporadas na matriz porosa. Neste estudo, a equação de Brinkman é utilizada para modelar o fluxo bifásico em meios porosos altamente heterogêneos. O modelo de Brinkman representa a dinâmica do fluxo através da matriz porosa e das cavidades usando uma única equação diferencial, sem a necessidade de condições interfaciais. No entanto, caracterizar com precisão as regiões de cavidades e matriz porosa permanece uma tarefa desafiadora, especialmente em modelos em escala de reservatório que normalmente representam formações geológicas com grandes áreas. Simulações de reservatório frequentemente envolvem modelos discretizados em células computacionais, cada uma com dimensões da ordem de vários metros que não descrevem a geometria das cavidades e fraturas presentes na matriz porosa. Esse estudo explora duas abordagens distintas para gerar propriedades equivalentes para meios vugulares. A primeira abordagem utiliza resultados do modelo de Brinkman para derivar propriedades equivalentes para o modelo de Darcy $1\phi1k$ na mesma escala. A segunda abordagem emprega a teoria de homogeneização para gerar propriedades equivalentes em uma escala mais grosseira. Essa teoria é aplicada a modelos de Darcy $1\phi1k$ e $2\phi2k$. Modelos $1\phi1k$ podem descrever efetivamente estruturas com cavidades dispersas na matriz porosa sem uma canalização forte de fluido. No entanto, para sistemas que exibem canalização substancial, a homogeneização só pode ser alcançada por meio de modelos de contínuo duplo. Em ambas as abordagens propostas, a determinação da permeabilidade absoluta equivalente e das curvas de permeabilidade absoluta equivalentes é imperativa para um processo de homogeneização eficiente.

Palavras-chave

Modelo de Brinkman; Escoamento bifásico; Curvas de permeabilidade relativa equivalente; Macroposidades; Upscale.

Table of contents

List of figures

List of tables

List of Symbols

Greek alphabet

α_{BJ} = slip coefficient

η = direction normal to the interface

α = fracture surface per unit of rock volume (m^{-1})

ρ = fluid density

λ = phase mobility

Ω = domain

Ω_M = porous matrix domain

Ω_V = vug domain

Γ_1 = inlet boundary

Γ_2 = outlet boundary

Γ_3 = impermeable wall

ϕ_V^ϵ = vug porosity on the fine scale

ϕ_M^ϵ = matrix porosity on the fine scale

$\phi_{1\phi 1k}^{eq}$ = matrix porosity on the coarse scale

μ = dynamic viscosity $[Pa \cdot s]$

μ^* = effective Brinkman's viscosity $[Pa \cdot s]$

λ_n = phase mobility

λ_T = total phase mobility

τ_h = triangular mesh element

ε_h = set of all faces of τ_h

ϵ = fine scale parameter

χ = fine scale characteristic length

X = fine scale characteristic length

σ = width of fissure aperture

Roman alphabet

B_o = oil formation volume

B_w = water formation volume

B_g = gas formation volume

c_{tm} = porous matrix total compressibility

c_{tf} = fracture total compressibility

E^n = LET parameter for the n phase

E_D = Displacement efficiency

f_w = water fractional flow

f_o = oil fractional flow

^{f} = denomination of fracture grid on coarse scale on $2\phi 2k$ model

g = gravity acceleration $(m \cdot s^{-2})$

h_E = is the diameter of the circle circumscribed in τ_h.

L = length (m)

L^n = LET parameter for the n phase

K = absolute permeability (mD)

K_{Vug} = Vug absolute permeability (mD)

k^0_{rw} = water relative permeabilty at the irreducible oil saturation

k^0_{ro} = oil relative permeability at the initial water saturation

K^m = matrix absolute permeability on the coarse scale of the $2\phi 2k$ model (mD)

K^f = fracture absolute permeability on the coarse scale of the $2\phi 2k$ model (mD)

k_{rw} = water relative permeability

k_{ro} = oil relative permealibity

$\mathbf{K}$ = Tensor absolute permeability (mD)

^{m} = denomination of porous matrix grid on coarse scale on $2\phi 2k$ model

$n_w = n_o$ = Corey water and oil exponent

p = pressure [atm]

p_c = capillary pressure (Pa)

R_s = solution gas oil ratio

o = oil

p_h = pressure approximation function [atm]

$\mathbf{v}$ = weight functions for velocity $[\frac{m}{s}]$

q = weight functions for pressure [atm]

q = source / sink term

r = weight functions for saturation

S = saturation

S_{wi} = initial water saturation

S_{or} = oil residual saturation

S_h = saturation approximation function

t = time [s]

T^n = LET parameter for the n phase

t_D = dimensionless porous volume injected

u_t = tangential velocity $(\frac{m}{s})$

$\mathbf{u}$ = velocity vector $[\frac{m}{s}]$

$\mathbf{u}_h$ = velocity vector approximation function $[\frac{m}{s}]$

u_D = Darcy velocity $(\frac{m}{s})$

q = source / sink term $(m^3 \cdot s^{-1})$

z = depth (m)

x_D = dimensionless length

v_{S_w} = velocity of the saturation front $(\frac{m}{s})$

w = water

Mathematical Symbols

$\mathcal{T}$ = Cauchy tensor

$\mathcal{P}_\kappa$ = bivariate polynomials of degree κ

$[\cdot]$ = jump operator

$\{\cdot\}$ = average operator

List of Abreviations

ALG = Adaptive Local–Global Upscaling Method

BJ = Beavers and Joseph interfatial condition

BL = Buckley-Leverett

BMD = Brezzi-Douglas-Marini

DECE = Designed Exploration and Controlled Evolution

DFVN = Discrete Fracture-Vug Network

DFVE = Discontinuous Finite Volume Element

EDFM = Embedded Discrete Fracture Model

DG = Discontinuous Galerkin

Dof = degrees of freedom

FEM = Finite Element Method

HM = History Matching

IMPES = Implicit Pressure Explicit Saturation

LDA = Laser Doppler Anemometry

LET = Model of Relative Permeabilty Curve Proposed by LOMELAND, F.;

EBELTOFT, E. ; THOMAS, W. H.

MFEM = Mixed Finite Element Method

MHD = Magnetic-Hydrodynamic

PDE = Partial Differential Equation

Re = Reynolds number

REV = Representative Elementar Volume

RKDG = Runge–Kutta Discontinuous Galerkin

RSME = root mean square error function

RT = Raviart-Thomas

SCAL = Special Core Analysis

SDA = Single domain approach

TDA = Two domain approach

WDU = Well Drive Upscaling

$1\phi 1k$ = Single Porosity Model

$2\phi 1k$ = Dual Porosity Model

$2\phi 2k$ = Dual Porosity and Dual Permeability Model

No. Try not. Do, or do not.
There is no try.

Master Yoda, *Episode V (1980).*

1
Introduction

1.1
Motivation

Fluid flow within a porous matrix with free-flow regions has extensive significance across different sectors, including industry, environmental, and biological systems. Examples of applications include filtration process [1, 2], interactions between surface water and subterranean aquifers [3, 4], fluid dynamics within textile materials [5], as well as the delivery of healing agents within the intricate network of blood vessels and organic tissues [6]. Multiphase flow in porous media with fractures and vugs of different sizes embedded in a porous matrix is essential in petroleum production. Modeling multiphase flow is challenging because free-flow regions, represented by fractures and vugs, interact with porous regions. The development of accurate models that describe the complex coupling of two-phase flow in the porous matrix and vugs is very important in oil production optimization.

A significant portion of the world's oil reserves are contained in carbonate reservoirs. Among them, karstified carbonate reservoirs represent a subgroup of the carbonate reservoirs with a significant role in oil production. Karstified carbonate reservoirs are widespread in different regions around the world, like Russia [7], China [8], the Middle East [9], and Brazil [10]. Particularly in Brazil, the pre-salt fields located in the Santos sedimentary basin stand out as some of the biggest recent oil discoveries. The term Pre-Salt describes the deposits formed when the African and South American landmasses were separated, resulting in the formation of the Atlantic Ocean. Within this stratigraphic layer, the Santos Basin contains substantial deposits of petroleum. These fields contain significant in-place volumes, favorable permeability and porosity characteristics, and distinctive diagenesis features. Currently, Pre-salt accounts for approximately 77 % of Brazil's total oil production [11].

Carbonate formations exhibit considerable heterogeneity and anisotropy. It is a direct result of their chemical composition, as well as the interaction of depositional and diagenetic processes. These processes evolved spontaneously over time. The gradual alteration has resulted in substantial permoporous

differences, even over a small area. The comprehensive scheme presented by Choquehe and Littleton (1970) [12] classifies carbonate porosity according to the interrelationship between porosity and structure. Primary porosity originates at deposition. Secondary porosity occurs after initial sedimentary layering, as result of diagenetic transformations. The carbonate rocks have a natural propensity for diagenesis, caused by their chemical activity. Predominantly constituted of calcite ($CaCO_3$) and dolomite ($CaMg(CO_3)_2$), these minerals undergo dissolution and, subsequently, are removed under the influence of water, resulting in structural modifications within the carbonate matrix. The diagenetic process produces a wide range of structural modifications, spanning scales ranging from millimeter-size voids, to the formation of extensive cavern systems that reach tens of meters. This phenomenon is also called karstification [13].

Numerical simulations of flow through naturally fractured and karstified reservoirs are extremely complex due to the simultaneous interaction of different scales, ranging from micropores ($\approx 10^{-6}$ m) to macropores (structures with dimensions stretching from millimeters to several meters). These voids have a considerable effect on the permeability of the porous media. Furthermore, these macropores may have connections via fracture networks. This is a phenomenon that can lead to considerable shifts in permeability, ranging over orders of magnitude [14]. The cumulative consequence of these intricate interactions, occurring in multiphase fluid flow, results in a noticeable decrease in volumetric oil sweep efficiency. This is particularly true when contrasted against comparatively homogenous rocks, such as sandstone.

In recent decades, a variety of methodologies have emerged to describe fluid dynamics within geological formations. The mathematical and physical approaches incorporated into these studies reflect their complex nature, with intricate interactions occurring across multiple dimensions. Yao and Huang, (2017) [15] describes two strategies for dealing with this problem: the Single Domain Approach (SDA) and the Two Domains Approach (TDA). The former, SDA, envelops flow dynamics within a singular domain, formulated through a single equation. In contrast, TDA separates the porous matrix and the free-flowing region into distinct domains. This approach requires the careful establishment of appropriate interfacial conditions, thereby coupling the differential equations underlying flow dynamics within each designated domain. Generally, the Darcy equation is used to describe the fluid flow within the porous matrix, while the flow within the free-flow regions is described by Navier-Stokes or the Stokes equation, depending upon the context.

Brinkman (1947) [16] proposed a single domain approach to avoid the

complexity of interfacial conditions between the porous matrix and the free-flowing regions. Typically, the Brinkman model characterizes fine-scale flows, with a subsequent scaling process that integrates it into larger, coarser-scale models [17]. This model is also applicable in plug-scale flow descriptions [18].

Dual-continuum models are an alternative approach to represent natural fractures and karstified reservoirs. Barenblatt et al. (1960) [19] presented a dual continuum model that describe the flow through both the porous matrix and the fracture network. The porous matrix is composed by interconnected blocks. Fractures are characterized by their dimensions exceeding the characteristic pore scale. Consequently, fractures display a higher permeability, yet their volumetric capacity is small compared to the porous matrix. To complete the representation, the porous matrix and the fractures couple through a fluid transfer function that describe the fluid exchange between two different domains.

1.2 Objectives

In this study, it is proposed a methodology for representing two-phase flow in kartified porous media. Brinkman's model is used to investigate the fluid flow in heterogeneous porous media containing vugs in the fine scale. The flow predictions obtained by the Brinkman model are used to generate equivalent properties for single-continuum and dual-continuum Darcy models in a coarse scale.

The two versions of a single-continuum ($1\phi 1k$) Darcy model are described used in this analysis. Firstly, a heterogeneous Darcy model is used to compare Brinkman and the Darcy models on a fine scale. In this approach, the vugular region is described as a porous medium with high porosity and permeability. The goal is to study the effects of viscous pressure drop in the flow through vug and fractures. In addition, it seeks to compare the Brinkman and Darcy models on the same scale. The second approach, a homogeneous Darcy model, represents domain homogenization. To represent the fine-scale solution, equivalent absolute permeability and equivalent relative permeability curves are established on the coarse scale which is modeled through the Darcy model. Using this methodology, equivalent properties can be established through numerical optimizations for use on a coarse scale.

It is also explored the use of dual-continuum models to homogenize the domain. Dual-continuum models distinguish porous matrix and fracture attributes, providing detailed description of the flow through the porous matrix and vug-fracture system. The $2\phi 2k$ model is used in these cases, where both the

porous matrix grid and the fracture grid are treated as homogeneous domains. The results are especially prominent for highly anisotropic porous media, with flow occurring preferentially through vugs. Consequently, it is necessary to establish equivalent absolute permeability and equivalent relative permeability curves for the fracture grid to achieve these results.

For both the single-continuum and dual-continuum homogeneous models, equivalent petrophysical properties are obtained through numerical optimization. The Brinkman method produces a fine-scale solution. In the coarse scale, the Darcy model is used, and the fine-scale results are represented through equivalent petrophysical properties. In the literature, this procedure is commonly referred to as upscaling by history matching. The purpose of this study is to fill a gap in the literature by describing how multiphase flow occurs in a karstified porous media. As a result, it utilizes a methodology that is more suited to understanding the physics of flow between a porous matrix and a free-flow region, a characteristic of fluid flow in a high heterogeneous medium. A second objective of this study is to generate equivalent petrophysical properties of kasrtified media that can be applied on a reservoir scale. The reservoir models are often tens of kilometers long, making it impossible to describe karst geometries at this scale. It is possible to represent karstified regions in a reservoir by utilizing equivalent petrophysical properties.

1.3 Thesis Organization

This thesis is organized into five chapters, including this introductory chapter.

Chapter 2 presents the literature review of heterogeneous porous media flow modeling. This chapter introduces the main methodologies employed in this study. It offers a comprehensive overview of the current state of the art regarding models that depict the transition between free-flow regions and flow within porous mediums. An overview of the key advancements in the dual-continuum model is provided.

Chapter 3 outlines the formulation and the methodology employed for implementing the numerical solution using finite element method for Brinkman and Darcy models. It elucidates the fundamental equations, alongside the numerical discretization, and the computational implementation of the solution. Furthermore, it presents the analytical solutions employed for numerical validation. The equations for a black-oil simulator, similar to the one utilized in the IMEX simulator, are presented in a generalized manner.

In chapter 4, the analysis and discussion of the results obtained using the

methods presented in chapter 3 are presented. This analysis includes numerical validations of the models used. Additionally, mesh testing and the methods used to generate these meshes are discussed. Results are presented for two different sets of vug configurations. The first set of synthetic vugs consists of simple geometric shapes. A second set consist of vug configurations of carbonate plug, obtained by micro tomography. In these cases, a comparison is made between Brinkman's model and both homogeneous and heterogeneous single-continuum Darcy models.

In Chapter 5, the third set of cases derived from Lajedo Arapuá is analyzed with dual-continuum models. This investigation examines models with intricate vug geometries and illustrates how the homogeneous $2\phi 2k$ model can be used to homogenize them. Cases with pronounced fluid channeling through the vugular media can be homogenized using this technique.

Finally, chapter 6 presents the conclusions of this work, as well as suggestions for future work.

2
Literature Review

This chapter provides a review of the existing literature, serving as a basis for this study. It begins with a concise description of carbonate rocks and vug formation processes. Furthermore, it provides insight into the most appropriate methodologies for modeling fluid dynamics within this geological context. There is a detailed description of the SDA and TDA methods. The SDA review focuses on the Brinkman equation for modeling such porous media. The TDA review focuses on exploring the interface conditions between porous region and free region flows. A comprehensive overview of the major dual continuum methods is also provided, with particular emphasis on the double porosity ($2\phi 1k$) and double porosity and double permeability ($2\phi 2k$) methods. Both academic research and industrial practices use these methods extensively.

2.1
Carbonate Rocks

Carbonate rocks, also called carbonates, are sedimentary rocks composed of minerals such as calcium carbonate ($CaCO_3$) or dolomite ($CaMg(CO_3)_2$). These rocks are formed by the accumulation and hardening of sediments found in freshwater and marine environments. They often contain preserved marine organisms, such as coral, mollusks, and foraminifera. Carbonate rocks have a wide variety of textures, which can provide a lot of information about their formation and history. They can display crystalline textures composed of fine-grained calcite crystals, or sparse textures with larger, sparkling crystals. Others, such as those with oolitic textures, consist of small spherical grains called ooids. A carbonate rock may be classified as mudstone, wackestone, packstone, grainstone, or boundstone depending on the grain size and sorting within the rock. Fine-grained mudstones can be distinguished from coarser-sized grainstones [20]. Figure 2.1 illustrates the classification of carbonates rocks based on their structural characteristics.

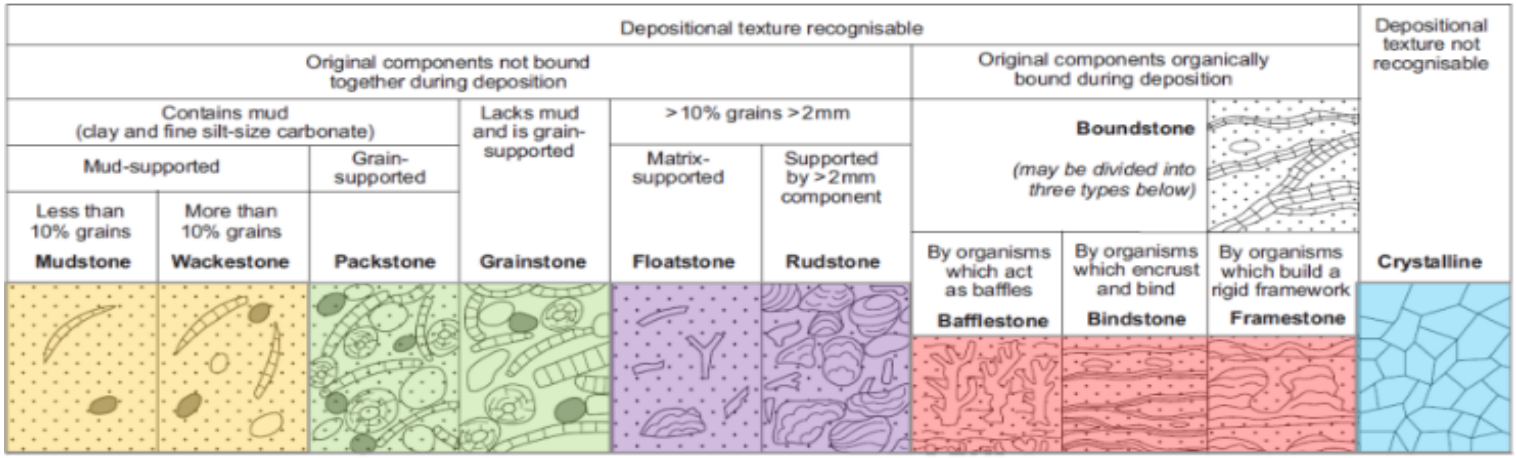

Figure 2.1: Classification for carbonate sedimentary rocks [20].

Carbonate rocks can be formed under a variety of environmental conditions. In shallow marine environments, such as reefs, lagoons, and platforms, organisms such as corals and mollusks contribute to carbonate deposition. In deep oceanic conditions, carbonate muds can accumulate, forming deposits similar to chalk. In freshwater settings, such as lakes and ponds, carbonates accumulate, resulting in rocks such as travertine and tufa. Carbonate rocks can dissolve over time due to acidic groundwater. This process creates karst landscapes characterized by sinkholes, caves, and underground drainage systems.

Choquehe and Littleton (1970) [12] classified carbonate rocks based on several factors, including pores and texture, as shown in figure 2.2. These classifications typically include primary and secondary porosity. Primary porosity is formed during sediment deposition, often linked to the arrangement of skeletal fragments or grains. It is important to note that interparticle porosity is found between individual grains within the rock, while intraparticle porosity is found inside specific particles, such as fossil pores or single grains within the rock. Moldic porosity results from the dissolution of more soluble minerals, leaving voids or cavities in the rock. Fenestral porosity arises from skeletal material dissolution, leading to irregular voids. Secondary porosity develops later due to various processes like dissolution, fracturing, or alteration. It is called vuggy porosity, which consists of large and irregular pores that resemble holes or voids formed by dissolution.

Fractures and karst are the main features that constitute to the rock heterogeneity for fluid flow. A kasrt is a term used to describe rock areas characterized by the formation or enlargement of void spaces, either unfilled or occupied by breccias or sediment [13] . In these processes, minerals undergo dissolution and are removed by the fluid that permeates the rock, often water in this context. Figure 2.3 shows different scales of karts in nature.

Two karstification patterns were identified by Meyers (1988) [21]. The first pattern, also called the classic pattern, is characterized by the enlargement of bedding planes and joints. This occurs in crystallized carbonates with minimal intergranular porosity and negligible permeability. This type of rock typically yields expansive caves and a clear pattern of preferred pathways through which fluids move. The second pattern, when dissolution occurs primarily within intergranular pores, resulting in minor cavities, irregular veins, or fissures without discernible structural or stratigraphic alignment. This kind of karst are dispersed and diffused. Moreover, the classic karst tends to penetrate carbonate rocks to depths of tens to hundreds of meters or even thousands of meters. Karst with a dispersed dissolution pattern typically

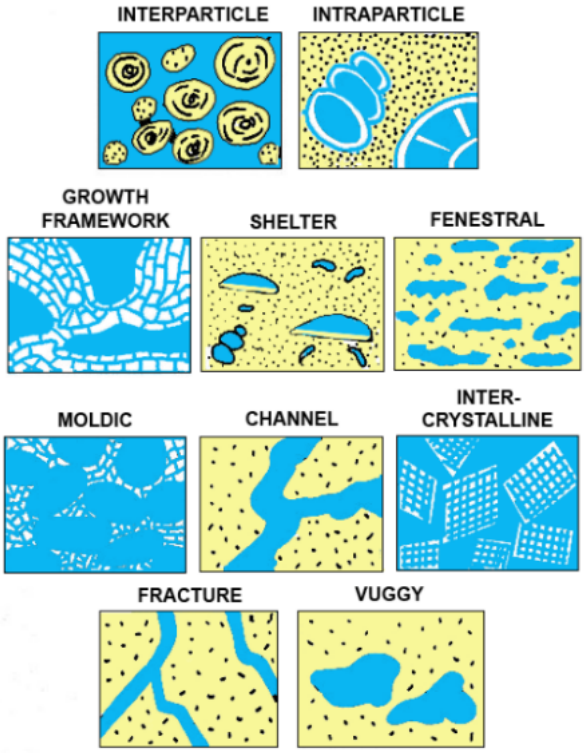

Figure 2.2: Classification of carbonate sedimentary rocks based on porosity [12].

reaches only a few meters or, at most, tens of meters below the surface. The most intense phase of karstification occurs in the first few meters of the dissolution process. A schematic representation of the formation of these two types of karst features are illustrated in figure 2.4.

Karst can also be classified according to how it was formed. It can be classified in two basic ways: hypogenic karst and epigenic karst. These processes are illustrated in figure 2.5. Hypogenic karst is caused by acidic groundwater that slowly dissolves the subsurface carbonate rocks. Consequently, caves and grottos are formed underground as a result of this process. On the other hand, epigenic karst develops at the rock surface. Generally, rock erosion and dissolution occur in the vadose zone (soil and rock layers that are unsaturated) and the epiphreatic zone (rock layers that are saturated). Several surface features are associated with epigenic karst formations, including sinkholes and lapiaz.

Fractures are structural discontinuities within geological formations caused by mechanical stresses. Figure 2.6 shows a typical example of fracture in rocks. A notable contrast in morphology exists between fractures and karsts, where karsts exhibit substantially greater volume compared to fractures. Fractures are caused by a combination of macroscopic forces, including tectonic plate movements, which provide the necessary stress for the rock to

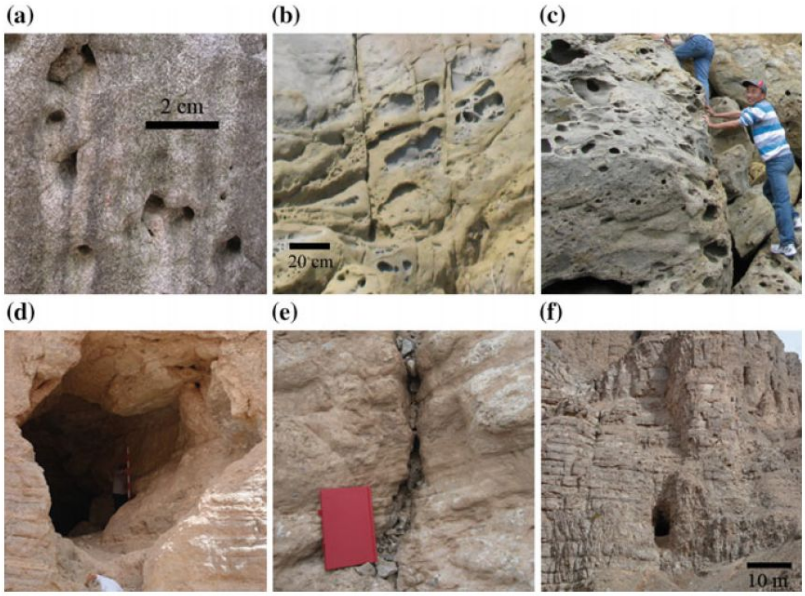

Figure 2.3: An example of various vug and karst features in nature [15].

be sheared or opened, and microscopic factors including the elastic properties of matrix grains and the structural arrangements within porous media, which include pore morphology and microcracks. The microscopic characteristics of a rock determine how fractures propagate. Fractures typically display a wide variety of linkages and networks [23].

2.2 Mathematical Models for Flow Through Heterogeneous Porous Media

Yao and Huang (2017) [15] presented a comprehensive discussion on modeling fluid flow through a porous medium embedded with fractures and vugs. Two distinct methodologies emerge for coupling the free-flow domain with the porous matrix: the Single Domain Approach (SDA) and the Two Domains Approach (TDA). In SDA, a single differential equation describes flow dynamics. It is not necessary to have an interfacial condition between the porous matrix and the free-flow domain. Conversely, the TDA establishes a boundary, treating the porous matrix and the free-flow as discrete entities, which requires the introduction of interfacial conditions to establish a connection between the differential equations delineating the flow in each respective domain. In essence, the Darcy equation applies to porous matrix dynamics, while the Navier-Stokes or Stokes equation describes free-flow region dynamics. The literature provides a wide variety of interfacial conditions that attempt to capture the dynamic relationship between the porous matrix and the free-flowing region. Beavers and Joseph (1967) [25] (BJ) present the classic interface condition, expressed

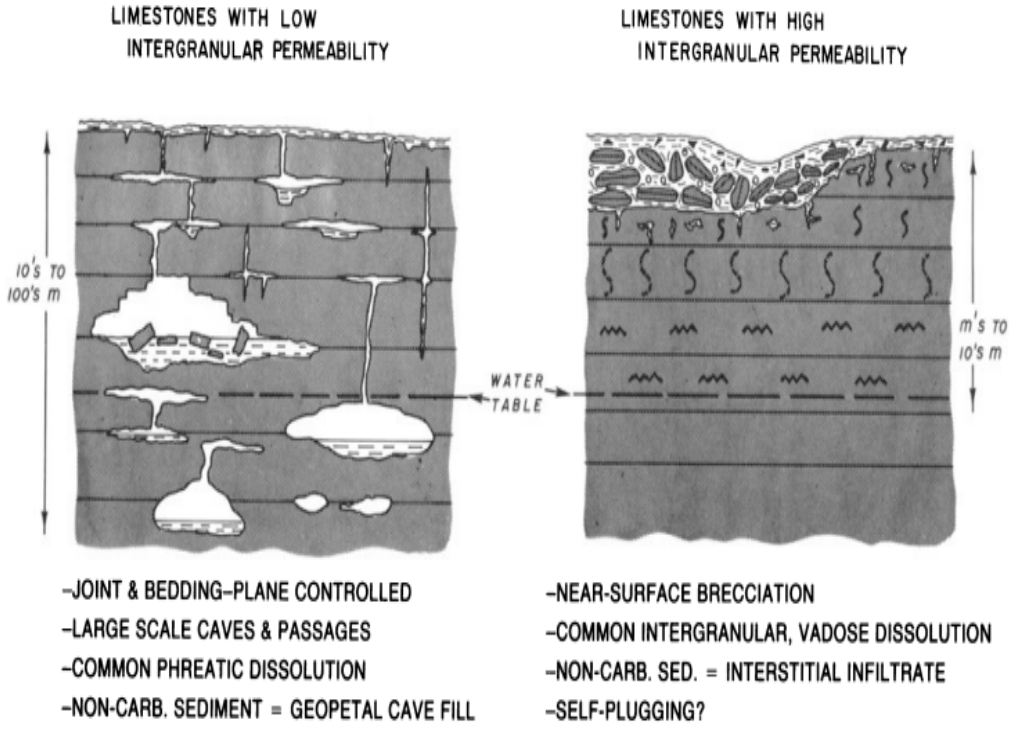

Figure 2.4: Schematic model of conduit-type kasrt (left) and diffuse karst (right) [21].

Figure 2.5: Schematic representation of epigenic kasrt (a) and hypogenic karst (b). Adapted from [22].

as :

$$\frac{\mathrm{d}u_t}{\mathrm{d}\eta} = \frac{\alpha_{BJ}}{\sqrt{K}}\left(u_t - u_D\right), \tag{2-1}$$

where u_t is the tangential velocity in the free-flow region, η in the direction normal to the interface, u_D is the Darcy velocity in the porous matrix, K is the absolute permeability, and α_{BJ} is a dimensionless parameter called the slip coefficient.

It is essential to determine α_{BJ} because it has a direct impact on

Figure 2.6: Example of fracture system.[24].

the accuracy of the representation of this interface condition. Nevertheless, estimating this coefficient accurately is significantly challenging. Specifically, α_{BJ} shows a strong relationship with the porous matrix configuration at the interface. Several references emphasize this point [26, 27, 28]. According to Zang and Prosperetti (2009) [29], pressure gradients, shear stresses, and Reynolds numbers influence α_{BJ}. Liu and Prosperetti (2011) [30] developed a boundary condition that refines the BJ condition, taking into account the pressure gradient and the viscous shear stress. Saffman (1971) [31] provided theoretical support for the validity of the BJ condition, though its applicability is restricted to planar interfaces. Several modifications have been made to the BJ equation in order to make it more versatile, so that it can be applied to a wide range of geometric configurations. The proposal was supported and elaborated in [32, 27, 33], exhibiting both physical and mathematical rigor. Jones (1973) [34] applied homogenization theory to create an equivalent interface condition aligned with the same principles.

Eggenweiler and Rybak (2020) [1] conducted numerical analyses of free flow regions interacting with anisotropic porous media where the fluid velocity at the interface has non-parallel trajectories. Numerical simulations did not agree with the BJ interfacial coupling condition. By integrating porous and free-flow regions with Stokes equations, they demonstrated the limitations of the commonly used Beavers–Joseph and Beavers–Joseph–Saffman interface conditions. The comparisons between coupled Stokes-Darcy simulations and pore-scale models revealed that these interface conditions often fail when flow

directions are not parallel to the porous medium interface, particularly when full permeability tensors are used. Furthermore, they noted that discrepancies between macro and microscale simulations were closely tied to the porous medium's geometry. All cases were applied to filtration processes, where velocities within porous media are higher than in free-flowing media.

Brinkman (1947) [16] introduced a single domain approach, which is successfully employed to describe fluid dynamics through a porous matrix coupled with free-flow domains. This method eliminates any interfacial conditions at the porous matrix interfaces with the free-flow region. Gray and O'Neill (1976) [35] and Whitaker (1999) [36] deduced Brinkman equation through the average volume method. Since then, several studies have been presented using the Brinkman equation to model karst and naturally fractured reservoirs. Neale and Nader (1974) [37] demonstrated congruence between the BJ interfacial condition and the Brinkman equation. Additionally, Taylor (1971) [27] deduced the BJ condition from the Brinkman equation. Krotkiewski et al. (2011) [18] calculated the effective permeability of a carbonate rock containing vuggs within a spatial volume measuring $13\times13\times21$ cm^3. Okabe and Blunt [38] conducted an analysis of permeability within the context of vugs and small-scale pores, successfully capturing the relationship between estimated permeability and macroporosity. Multi-scale investigation was conducted using microtomography and multi-point statistics on a carbonate rock sample. The permability was computed using the Lattice Boltzmann method. There was good agreement between the computed average permeability and the measured permeability. Golfier et al. [39] investigated the macroscopic behavior utilizing the Darcy-Brinkman model. They worked on numerical solutions for fractured and cavity porous media. An explicitly analytical solution for effective permeability was derived and compared to the numerical solution. Dali (2019) [40] employed the Brinkman formulation to solve 2-D flow in porous media in carbonates with macropores. The geometry of the pore structure was determined by microtomographic images of a carbonate rock sample. It was confirmed the compatibility between Brinkman equation and BJ condition, specifically to single-phase flows within karstified porous media. In particular, this validation extends to scenarios in which the velocity within the free-flow domain is much greater than that within the porous domain. A discrepancy in velocity induces quasi-parallel flow directions within the free flow region and the porous matrix, which leads to minimal numerical error. Cruz (2022) [41] extended the previous study to a three-dimensional setting with similar results. Dali (2019) [40] demonstrated that in studies of carbonate rock flows, the velocities within the vugular regions are greater than those in the porous

regions. Moreover, the velocities in the vugular regions are closely parallel to principal vug orientation. It is therefore expected that, when applying BJ interfacial conditions in reservoir studies, the velocity field should have fewer distortions than those reported by [1], because the flow trajectory is parallel to the porous media interface.

Establishing the α_{BJ} parameter to simulate flow in carbonate rocks remains challenging. This parameter is not affected only by the surface interaction between the porous medium and the free-flow region, but also by various flow parameters [29]. Due to the internal flow dynamics in the porous medium, it is difficult to conduct laboratory measurements within this carbonate rock samples. Furthermore, to the best of our knowledge, there appears to be a gap in the literature concerning studies that integrate interfacial conditions with multiphase flows, specifically in two-phase systems. Furthermore, oversimplifications using arbitrary values of α_{BJ} may lead to significant errors. As a result, the SDA methodology appears to be a promising approach for the purposes outlined in this study. It simplifies the implementation process and reduces uncertainties associated with the selection of α_{BJ} parameter. Moreover, the existing literature indicates that the Brinkman model exhibits strong correlations with a variety of interfacial conditions [37]. A comprehensive exploration of the Brinkman viscosity term (μ^*) is also presented in section 3.1.5.

There is relatively limited reference available for applying Brinkman's model to multiphase flows in comparison with its single-phase models. Coclite et al. (2014) [42], Bürger et al. (2016) [43] and Dine and Saad (2018) [44] solved the Brinkman equation in an immiscible two-phase flow in a non-homogeneous porous medium. Coclite et al. (2014) [42] utilized a weak form combined with the finite difference method to demonstrate model convergence. Meanwhile, Bürger et al. (2016) [43] used the Discontinuous Finite Volume Element (DFVE) method and the Runge–Kutta Discontinuous Galerkin (RKDG) method, to solve the Brinkman equation effectively through the satisfaction of discrete maximum principles and the attainment of numerically robust outcomes. Dine and Saad (2018) [44] performed convergence analysis of a combined non-conforming finite volume method with finite element methods discretized in a triangular mesh. The authors established a numerical solution within the weak form and demonstrated convergence. However, solution uniqueness proof remains inconclusive due to intrinsic nonlinearities. They noted that the Brinkman equation adds diffusivity to the system compared to the Darcy solution. Hallak et al. (2019) [45] investigated a five-spot drainage geometry, where a central karstified region interacts with the surrounding porous matrix. This dynamic interplay was characterized by substantial contrasts in

porosity and permeability between the two regions. In situations characterized by high to moderate Darcy numbers, the Brinkman models result in divergent fluid displacement fronts when compared with non-homogeneous Darcy formulations with different porosity and permeability in each region.

In a study developed by Belhaj et al., (2005) [46], non-Darcy flow is examined in terms of viscous, inertial, and convective effects in fluid flow through porous media. A modified Brinkman formulation was used to accommodate two-phase flow in multiphase conditions commonly encountered in fractured petroleum reservoirs. In contrast to conventional models such as Darcy's equation, the researchers attempt to provide a more accurate representation of fluid flow in reservoirs characterized by high velocities or fractures. For scenarios involving high velocities, the modified Brinkman formulation is suitable, whereas Darcy can be used for scenarios involving low velocities.

Armiti-Juber and Rohde (2019) [47] conducted a series of two-phase studies employing an asymptotically flat domain, wherein the Brinkman model demonstrated superior physical and numerical outcomes compared to the conventional Darcy model. The Brinkman model accurately describes two-phase flow in flat domains, particularly in high porosity media. In such environments, it incorporates effective viscosity and second-order terms. In particular Brinkman vertical equilibrium agrees excellently with the full two-phase flow model, while being computationally more efficient. It is demonstrated that the Brinkman vertical equilibrium model accurately describes saturation overshoots and exhibits a spreading speed smaller than the Darcy model. Armiti-Juber and Rohde (2019) [48] analyze weak solutions for a nonlocal pseudo-parabolic model describing nearly uni-directional two-phase flow in Brinkman regimes. The model describes homogenized flow of two immiscible phases in a rectangular porous media domain, featuring equations for two distinct two-phase flow scenarios. The study concentrates on asymptotically flat domains and includes a nonlocal evolution equation representing nearly unidirectional two-phase flow. Armiti-Juber (2022) [49] examines two-phase flow in thin porous media domains of Brinkman type. A weak solution to a coupled two-phase flow model converges to a weak limit as the domain width-length ratio approaches zero. With a single nonlocal evolution equation of saturation, the reduced model captures the original coupled model effectively. As the geometrical parameter diminishes, this convergence simplifies complex two-phase flow phenomena in porous media.

Elkady et al. (2022) [50] study on non-Darcian immiscible two-phase flow through porous materials investigates flow behavior and heat transfer charac-

teristics in porous media using the Darcy-Forchheimer-Brinkman model. The study aims to understand how porosity, inertia, friction, and saturation affect the flow dynamics and thermal aspects of immiscible two-phase flow through porous materials. Both numerical simulations and experimental validations are conducted to analyze the hydrodynamic and thermal aspects of the flow, with a focus on the channeling effect, velocity distribution, and the impact of neglecting certain parameters like the Brinkman coefficient and flow inertia. Regarding the Brinkman model influence, they concluded that the Brinkman model in the study of non-Darcian immiscible two-phase flow through porous materials is that neglecting the Brinkman coefficient enhances the channeling effect and increases flow velocity near the solid boundary, resulting in faster flow at the wall.

Two-phase flow using the Brinkman equation models fluid flow and heat transfer, as well as two-phase fluid flow with suspended particles. Bhatti et al. (2018) [51] investigated the impact of mass and bio-heat transfer on the peristaltic propulsion of two-phase flows through a Darcy-Brinkman-Forchheimer porous medium. They aim to understand how the Brinkman equation influences heat and mass transfer effects in the presence of magnetic fields, compliant walls, and chemical reactions. They concluded that the Brinkman number, which represents the ratio of viscous dissipation to molecular conduction, plays a significant role in temperature distribution. Due to viscous dissipation, a high Brinkman number reduces conduction, which increases temperature. The study conducted by Khan et al. (2022) [52] examined the generalized dusty Brinkman type of fluid that flows between parallel plates under magnetic-hydrodynamic (MHD) free convection. A generalized Brinkman type dusty fluid was studied to examine the combined effect of a magnetic field and heat transfer. It has been argued that the fractional model of dusty fluids of the Brinkman type is more realistic than the classical model. The effect of time on Brinkman-type fluid and dust particle velocity was highlighted, which demonstrated that both velocities increased with the passage of time, indicating the dependence on time of unsteady fluids.

Simulation of oil reservoirs involves partitioning vast domains spanning tens of kilometers into discrete units with smaller dimensions, typically measured in meters. Unfortunately, refining meshes to capture vug geometry accurately is both costly and impractical. Homogenization theory can be useful in this scenario in order to accurately represent fluid flows in large domains. In this method, two distinct scales are used in the analysis. The fine scale is simulated using models that are capable of capturing detailed characteristics of the flow. For flow in vugular porous media, the Darcy model is usually ap-

plied to simulate the porous matrix, while the Navier-Stokes or Stokes models are used to simulate the vugular regions. In the coarse scale, only the Darcy model is used. The transfer of scale is generally accomplished through equivalent properties, such as absolute permeability and relative permeability curves.

Argabost et al. (2004) [53] presented a homogenization approach for single-phase, incompressible, viscous fluid considering a variety of vug configurations, including layered vugs, meandering vug channels, constricted vug channels, and disconnected vugs. Their findings indicate that connectivity between the vugs is crucial to predicting macroscopic properties. In their subsequent work, Argabost and Lehr (2006) [54], based on the homogenization of single-phase flow, derived an analytical solution for simple geometries. Based on this model, the vug can be represented through Poiseuille flow and alternates from vug to matrix behaves as if the vugs have infinite permeability. Argabost et al. (2009) [55] applied the Darcy-Stokes coupled equations with the Beavers-Joseph-Saffman interfacial condition to create a macro-model for vuggy porous media. The authors simulated field-scale aquifer flow using different synthetic vuggy media configurations to demonstrate the importance of elements such as channel shape, aperture, and disconnectivity. Huang et al. (2010) [56] proposed a mathematical flow model for a discrete fracture-vug network (DFVN). Utilizing homogenization theory, they derived the equivalent Darcy flow equation and obtained the theoretical formula for the effective permeability tensor of fractured vuggy media. The examples illustrate that permeability of the medium is significantly affected fracture or vug sizes, though it remains independent of the distribution of the fractures or vugs.

Popov et al. (2009) [14] applied the Brinkman equation on fine-scale dynamics within a synthetic porous medium interlaced with vuggs and a complex pattern of fractures resulting in connectivity between the vuggs. This interaction resulted in a substantial increase in effective permeability. Meanwhile, Qin et al. [57] and Gulbransen et al. (2010) [58] effectively derived the absolute permeability from a local solution at a fine scale using Brinkman equation. Subsequently, upscaled permeability is applied to solve the Darcy equation at a coarse scale. Similarly, He et al. (2015) [59] proposed a Brinkman model to simulate transient single-phase fluid flow in 2-D synthetic representations of naturally fractured and karstified carbonate reservoirs. In naturally fractured carbonate karst reservoirs, cavities and natural fractures profoundly alter fluid transport patterns. Conversely, cavities alone do not produce comparable effects. Campos (2022) [60] developed a single-phase transient simulator based on the Brinkman equation. Compared to the dual-continuum models, Brinkman results showed a strong correlation.

Huang et al. (2013) [61] conducted a comprehensive investigation of two-phase flow. They applied the methodology developed on Huang et al. (2010) [56] to compute the absolute permeability of the coarsened grid. In the context of two-phase flow, they introduced an innovative approach to calculating relative permeability curves. On the fine grid, a distinction was made between the relative permeability in the vuggy domain and the porous matrix. Consequently, analytical techniques were employed to derive a novel pseudo-relative permeability curve for the coarse grid. This pseudo-relative permeability curve effectively captures the influence of the relative permeability curves of both the porous media and the free-flow region. Yan et al. (2016) [62] investigated two-phase flow in fractured-vuggy reservoirs. They employed homogenization theory for small fractures and vugs, and modeled long fractures using the Embedded Discrete Fracture Model (EDFM). The homogenization theory is used to determine the equivalent absolute permeability. An analytical method is used to determine the relative permeability for the coarse scale. This approach simplifies the numerical simulation of flow in fractured-vuggy reservoirs by avoiding unstructured meshing and numerical calculations for the entire reservoir.

2.2.1 Dual-Continuum Models

Dual-continuum models are one of the approaches used to model flow in natural fractured and karstified reservoirs. Barenblatt et al. (1960) [19] proposed the dual-continuum framework that provides a comprehensive method for analyzing the flow through porous matrix and fractures independently. Basically, it consists of two equations that allow for independent modeling of two distinct media. The main characteristic of this model lies in that the porous matrix consists of interconnected blocks, whereas the fractures are wider than the characteristic pore size. Thus, the fractures have higher permeability when compared to the porous matrix. Moreover, the porous matrix and fractures are coupled by a fluid transfer function to ensure effective fluid transfer between them. Eq. (2-2) is also known as the dual-continuum model ($2\phi 2k$):

$$\begin{cases} \nabla \cdot (K^m \nabla p^m) - \alpha \left(p^m - p^f\right) = c_t^m \mu \phi^m \dfrac{\partial \rho^m}{\partial x}, \\ \\ \nabla \cdot \left(K^f \nabla p^f\right) + \alpha \left(p^m - p^f\right) = c_t^f \mu \phi^f \dfrac{\partial \rho^f}{\partial x}, \end{cases} \tag{2-2}$$

where the superscripts m and f indicate the matrix and fracture domains and α is a dimensionless parameter that measures the characteristic of fissured rocks. The parameter α is generally represented as:

$$\alpha = K^m \sigma^2 \tag{2-3}$$

The authors assumed that the fluid transfer intensity between the porous matrix and the fractures depends on the permeability of the matrix K^m, coupled with the width of fissure aperture (σ), that is, the fracture surface per unit of rock volume, which is also known as the shape factor.

The shape factor reflects the geometric relation between the matrix and the fracture. Due to its inherent nuances and associated uncertainties, the parameter σ has received considerable attention. Many studies have been conducted in order to provide a more accurate representation of σ. The model proposed by Warren and Root (1963) [63] simplifies this approach by assuming that the primary porosity system, or the porous matrix, is composed of identical rectangular parallelepiped blocks with constant properties. The secondary porosity system, referred as the fracture system, is characterized by an orthogonal network with axes parallel to the edges of the matrix blocks and spaced uniformly with constant width. According to this model, fluid can flow between the matrix and the fracture, but not between different blocks of the matrix. Consequently, fluid flow only occurs through the fractures, while the matrix functions as a source/sink. It is commonly called dual porosity model or just $2\phi 1k$ model. Figure 2.7 represents the idealization of a fracture reservoir.

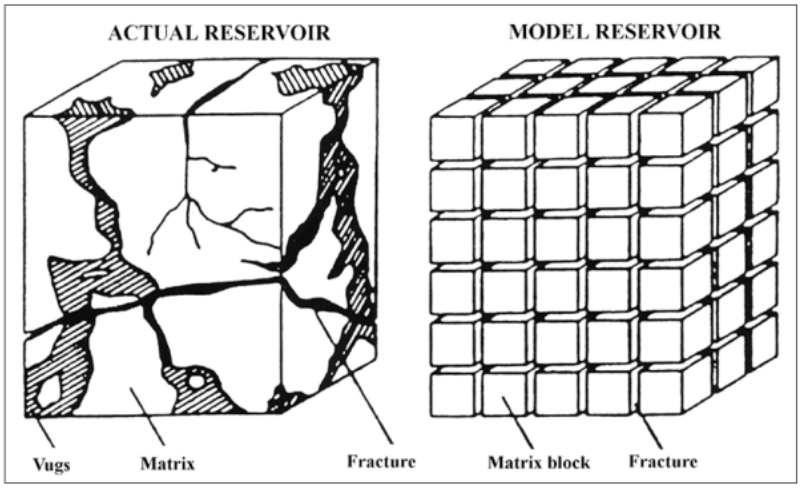

Figure 2.7: Schematic representation of a fractured porous medium proposed by Warren and Root (1963) [63].

In contrast to Warren and Root (1963) [63], which simplified the matrix representation into cubic blocks surrounded by fractures, Kazemi et al. (1976) [64] presented it as a rectangular block of varying dimensions. Thomas et al. (1983) [65] contributed significantly by introducing a matrix-fracture

formulation that was remarkably stable. In this formulation, fracture flow is integrated seamlessly with matrix fracture flow, implicitly taking into account variables such as pressure, water saturation, gas saturation, and oil saturation. Gilman and Kazemi (1983) [66] modified the Kazemi et al. (1976) [64] model by adding diagonal permeabilities in the grid cells. Gilman (1986) [67] refined a $2\phi 1k$ block model for representing heat transfer, gravity segregation, and other transient phenomena. Quandalle and Sabathier (1989) [68] improved method for the fluid transfer term between matrix and fracture in a dual-porosity system. The method achieves higher accuracy and calculates flows related to capillary, gravity, and viscous forces within the system.

To enhance the capabilities of the $2\phi 1k$ model, an improved model called the $2\phi 2k$ model was introduced by Gilman and Kazemi (1988) [69] and Dean and Lo (1988) [70]. In the $2\phi 2k$ model, fluid flows between matrix to matrix and matrix to fracture block, allowing a more comprehensive representation of flow behavior. Other authors have refined the physical representation of the $2\phi 2k$ models. Sonier et al. (1988) [71] proposed a gravity-driven fluid exchange mechanism between the matrix and fracture. Coats (1989) [72] improved the Warren and Root (1963) [63] model representing capillary pressure, gravity, and viscous forces within the matrix-fracture transfer function in the context of a compositional fluid model. Meanwhile, Ueda et al. (1989) [74] introduced a gravitational model to predict the fluid phase vertical equilibrium. This model delineates a transition zone within the matrix block to more effectively capture the nuanced manifestation of the transient saturation profile. This is determined by the dynamic relationship of viscous, capillary, and gravity forces. This marked enhancement precipitated a modification of the shape factor, aligning it more effectively with empirical observations. Fung (1991) [74] enhanced the dual-porosity/dual-permeability models by describing matrix/fracture drainage patterns block-to-block for gas and oil flow, using a pseudo-capillarity potential. Uleberg and Kleppe (1996) [75] based on an extensive analysis of physical mechanisms and influential parameters impacting fluid flow in fractured reservoirs, argues that a comprehensive model for such reservoirs must integrate all primary flow mechanisms and processes. It encompasses a variety of factors including gravity, capillary forces, gravity drainage, diffusion, capillary continuity, and reinfiltration. In mixed-wet systems, simulations demonstrated the importance of capillary continuity between matrix blocks. Meanwhile, Lu and Blunt (2007) [76] proposed an improved transfer function that accounts for displacement due to imbibition when capillary pressure is positive, in combination with gravity drainage, for $2\phi 2k$ systems.

2.3 Upscaling Methodology

Single-phase static upscaling techniques are common in reservoir studies. Numerous studies have been conducted in this area, and the most important ones are described below. The most common method used to upscaling porosity from fine-scale models is the volumetric weighted arithmetic mean, which ensures preservation of pore volume [77]. In terms of permeability upscaling, there are three main methods employed: averaging, which involves horizontal arithmetic and vertical harmonic averages; Cardwell-Parsons directional averaging [79]; and flow-based upscaling with closed boundary conditions [78, 80]. In addition, Wen and Gomez-Hernández (1996) [81], Renard and Marsily (1997) [82], Farmer (2002) [83], and Durlofsky (2003) [77] provide detailed literature reviews on upscaling methods. These authors agree that flow-based techniques are most effective for upscaling absolute permeability.

An effective upscaled model of fluid injection in heterogeneous reservoirs typically requires more effort. Two-phase upscaling is recommended for processes involving water or immiscible gases injection. When fine-scale simulation data are available, pseudo-relative permeability curves are commonly used to enhance the accuracy of coarse-scale simulation models. Various methodologies have been proposed to enhance the representation of small-scale results in coarse-scale simulation models. Barker and Fayers (1994) [84] developed the method of transport coefficients (also known as α-factors), which is a method that uses modifiers introduced into flow terms to calculate the composition of fluids flowing from a large grid block as compared to the average composition of fluids within that block. Additionally, pseudo relative permeability curves are used. The method was tested for various fluid systems with improved accuracy in the results, particularly in terms of component production rates. Barker and Thibeau (1997) [85] conducted a comprehensive review of existing relative permeability upscaling approaches. They highlighted significant limitations associated with pseudo-relative permeability curves during the upscaling of fine-grid geological models to coarse-scale simulation models. They concluded that pseudo-relative permeability curves are viable only in scenarios where capillary or gravity equilibrium can be assumed at the coarse-scale grid block. Chen et al. (2003) [86] proposed a coupled local–global upscaling method, where local boundary conditions for computing upscaled properties are derived from global coarse-scale flows. They demonstrated notable enhancements over conventional local methods but did not explore specific global flow patterns or well effects, potentially impacting upscaling accuracy. Chen and Durlofsky (2006) introduced an adaptive local–global (ALG) upscaling method to tailor coarse-scale

parameters for various global flow conditions. They implemented a threshold to update upscaled properties only in high-flow regions, potentially enhancing upscaling efficiency. Results on highly heterogeneous systems showed enhancements over local and coupled local-global upscaling techniques. Zhang et al. (2008) [88] proposed the Well Drive Upscaling (WDU) method, utilizing global well drive and actual boundary conditions to address inappropriate boundary conditions in single-phase upscaling. While presenting promising results, the approach requires a fine-scale pressure solution for application. Moreover, this method is suitable for effectively upscale the transmissibility since relative permeability is still a challenge to be represented block-to-block.

Regarding the application of dual-continuum techniques to upscaling, Evazi and Jessen (2014) [89] proposed an approach to upscaling heterogeneous reservoir models by splitting porosity. Based on flow capacity, this method classifies reservoirs into primary and secondary porosities. The authors rigorously evaluate this approach against traditional single-porosity models, demonstrating its superior ability to capture preferential flow paths and enhance displacement efficiency. There is evidence that the dual-porosity model is capable of improving displacement efficiency representation in coarse-scale modeling, as well as predicting breakthrough times and post-breakthrough responses with increased accuracy. However, the overall workflow can be costly since fine-scale models require streamline simulations to be obtained. As another disadvantage, the strategy can be dependent on the original well locations and flow rates due to the use of fine-scale results to divide the porous media. Rios et al. (2020) [90] introduced an innovative $2\phi 2k$ upscaling approach. This method enhances coarse-scale predictions accuracy compared to conventional techniques, particularly in reservoirs with significant heterogeneity. By addressing the optimistic tendencies inherent in traditional upscaling methods, the proposed strategy offers dependable outcomes even at large upscaling ratios. It consistently refines traditional upscaling outcomes across diverse flow-direction scenarios. By using the flow and storage capacity as well as the Lorenz coefficient, fine-scale porous media are segmented into primary and secondary systems. The respective properties for each coarse-scale are computed, and the flow is simulated within the revised upscaled model using the $2\phi 2k$ model. According to the results, the method is effective in reducing biases in sweep efficiency and oil recovery factor estimations, as well as refining coarse-scale uncertainty profiles.

2.4 Summary

Studies involving homogenization in domains where flow occurs simultaneously between the porous medium and the free flow region are relatively common for single-phase flow. Generally, homogenization or volume averaging techniques are used for this purpose. In this context, many studies use the Brinkman equation on a fine scale and the Darcy model on a coarse scale for single-phase studies. In comparison, few studies have been published using the Brinkman equation to model two-phase flow. The homogenization of two-phase flows has also been applied in relatively few studies.

This study aims to fill the gap in the literature regarding two-phase flow modeling in kasritic systems. Brinkman two-phase flows model is applied on a fine scale. Based on Brinkman results, upscale is applied to derive coarser results. Based on a more realistic physical description of fine-scale results, this study proposes a methodology for establishing equivalent petrophysical properties on the coarse scale. Most of the upscaling methods mentioned above focus on determining petrophysical properties on a reservoir scale. It is not feasible to directly upscale highly detailed models, in which vug geometries can be discretized, to reservoir scales, in which simulation cells span hundreds of meters. This study aims to derive equivalent properties for describing karst systems. In this sense, this method may be considered an intermediate upscaling procedure in reservoir modeling, which connects the scale between a rock sample of several centimeters and that of the field.

3
Flow Models and Solution Methods

This chapter details the methodologies employed in this study. It covers the fundamental equations of the Brinkman and Darcy models for single and two-phase flow, including the weak form of these equations for finite element discretization. Furthermore, it details the analytic solutions from the literature for some simple problems used for solution method implementation validation. The chapter also outlines methodologies for comparing the Brinkman model with the single-continuum and dual-continuum Darcy models. It provides insights into the approaches used for achieving equivalency in porous media through the single-continuum model and the dual-continuum model. Additionally, a brief overview of the black-oil model is included, as the double-continuum models are solved using CMG's commercial software. Furthermore, the mesh tests for the cases studied in chapters four and five are presented.

It is first necessary to establish assumptions to simplify the physical and mathematical models proposed in order for the problem to be posed correctly. In all subsequent studies, the following hypotheses are be used.

1. Low Reynolds Flow;
2. Immiscible Fluids;
3. Capillary Pressure is neglected;
4. Gravitational effects neglected;
5. 2-D Domain;
6. Incompressible Fluid and porous matrix;
7. Isothermal flow and no chemical reactions;
8. Constant properties ;
9. The pore space is fully saturated with aqueous and oleic phases.

In order to provide a better understanding of these hypotheses, it is worth highlighting a few of them. In a porous matrix as well as in free-flowing media, capillary pressure is negated. As only horizontal flow is considered, gravitational effects are ignored.

3.1 Flow Models

3.1.1 Mass and Linear Momentum Conservation for Single Phase Model

Mass conservation is described by the following differential equation:

$$\frac{\partial \rho}{\partial t} + \nabla \cdot (\rho \mathbf{u}) = q \ , \tag{3-1}$$

where ρ is the density, $\mathbf{u}$ is the velocity vector, and q is a source / sink term.

Linear momentum conservation is governed by the Cauchy equation:

$$\rho \frac{D\mathbf{u}}{Dt} = \rho \mathbf{g} + \nabla \cdot \mathcal{T} \ , \tag{3-2}$$

where $\mathbf{g}$ is the gravity force and $\mathcal{T}$ is the Cauchy stress tensor. In this study, it is only considered Newtonian fluid. Thus, eq. (3-2) is simplified with the assumptions of isotropic fluid and linear relation between the strain rate and the viscous stress, i.e:

$$\mathcal{T} = -p\mathbf{I} + \mu \left(\nabla \mathbf{u} + \nabla \mathbf{u}^T \right) \ , \tag{3-3}$$

where p is the pressure and μ is the dynamic viscosity.

The Navier-Stokes formulation is attained by expanding equation (3-2) and subsequently implementing (3-3):

$$\rho \left(\frac{\partial \mathbf{u}}{\partial t} \right) + \mathbf{u} \cdot \nabla \mathbf{u} = \rho \mathbf{g} - \nabla p + \mu \nabla^2 \mathbf{u}. \tag{3-4}$$

For this analysis, it is assumed that the flow occurs at low Reynolds numbers ($Re \ll 1$), i.e., momentum advection terms are much smaller than viscous terms ($\mathbf{u} \cdot \nabla \mathbf{u} \ll \nabla^2 \mathbf{u}$). Gravity is also neglected since it is considering horizontal two dimensional domain. With all the above hypothesis, the Navier-Stokes equation is simplified to Stokes equation:

$$\nabla p = \mu \nabla^2 \mathbf{u}. \tag{3-5}$$

Since oil reservoir flows typically exhibit low velocities, the Skotes equation is suitable for simulating free-flow regions. Although high Reynolds numbers are present near wells at distances up to several tens of meters, in the majority of reservoirs, the low Reynolds number hypothesis can be confidently applied.

3.1.2 Darcy Equation for Single Phase Flow

Darcy's law is a fundamental equation for modeling flow through porous media [91]. Its popularity can be attributed to its ability to accommodate intricate structures accurately, since microscopic pore space flow is simplified to an average representation of fluid motion. Darcy's law establishes a linear relationship between flow magnitude and the potential gradient acting on fluid, i.e:

$$\mathbf{u}_D = \frac{K}{\mu}\left(-\nabla p + \rho \mathbf{g} \nabla z\right) \tag{3-6}$$

where $\mathbf{u}_D$ is the Darcy velocity, z is depth and K is the permeability. It is assumed that the porous media is isotropic, so the permeability tensor can be expressed by a single scalar variable.

3.1.3 Darcy Equation for Two-Phase Flow

This section presents the equations and underlying assumptions of Darcy two-phase flow model. The fluids are considered immiscible in this model, and there is no mass exchange between the phases or with the solid phase. It is noteworthy that water is identified as the wetting phase, denoted by w, whereas oil is identified as the non-wetting phase, denoted by o.

Furthermore, it is essential to establish equations that describe how relative permeability and the capillary pressure vary with fluid saturation. In this study, the porous media exclusively has water and oil, therefore:

$$S_w + S_o = 1, \tag{3-7}$$

where S_w and S_o are the respective volume fractions for water and oil, respectively.

In porous media, capillary forces are induced when two or more immiscible fluids come into contact. These fluids interact with one another and with

the solid phase resulting in a contact angle with the porous medium walls. The phenomena is inherently governed by cohesive forces at the molecular level within the respective phases, as well as by adhesive forces between them.

The capillary pressure, denoted as p_c, is conventionally characterized by:

$$p_c(S_w) = p_o - p_w, \tag{3-8}$$

where p_o is the pressure within the non-wetting phase and p_w is the pressure within the wetting phase [3]. Capillary pressure can be described using a variety of empirical and mathematical models. In the present study, capillary pressure is neglected, i.e. $p_c = 0$.

For two-phase flow, Darcy equation (eq. 3-6) is generalized as

$$\mathbf{u}_n = \frac{Kk_{rn}}{\mu_n}\left(-\nabla p_n + \rho_n \mathbf{g}\nabla z\right) \quad n = w, o\ , \tag{3-9}$$

where k_{rn} is the relative permeability of each phase, which is a function of the phases saturation.

Mass conservation equation for each phase (3-1) in flow through porous media is expressed as:

$$\frac{\partial(\phi\rho_n S_n)}{\partial t} + \nabla\cdot(\rho_n \mathbf{u}_n) = q_n \quad n = w, o\ , \tag{3-10}$$

where ϕ is the porosity.

The total Darcy velocity $\mathbf{u}$ is the summation of each phase Darcy velocity:

$$\mathbf{u} = \mathbf{u}_o + \mathbf{u}_w. \tag{3-11}$$

It is also necessary to define the phase mobility (λ_n), total mobility (λ_T), and fractional flow (f_n), respectively:

$$\lambda_n = \frac{k_{rn}}{\mu_n}, \tag{3-12}$$

$$\lambda_T = \lambda_w + \lambda_o, \tag{3-13}$$

$$f_n = \frac{\mathbf{u}_n}{\mathbf{u}}. \tag{3-14}$$

When capillary pressure is neglected, the fractional flow of each phase is equal to the ratio between the phase and total mobilities,

$$f_n = \frac{\lambda_n}{\lambda_T}. \tag{3-15}$$

Using the definition (3-7), it is only necessary to calculate the saturation in one phase because the other one is easily obtained. It is chosen the wetting phase, water (w). In this study, the capillary pressure and the gravitational force are neglected. For simplification, it is assumed that water and oil have identical density, ensuring uniform local fluid density. In addition, fluids and porous matrix are treated as incompressible. Consequently, ρ_o, ρ_w, and ϕ are constant. Thus, the mass conservation for the wetting phase becomes:

$$\phi \frac{\partial S_w}{\partial t} + \nabla \cdot (f_w \mathbf{u}) = q_n, \tag{3-16}$$

where q_n is a source/sink term.

Accordingly, the following set of equations are used to describe the Darcy two-phase flow:

$$\nabla \cdot (\mathbf{u}) = q, \tag{3-17}$$

$$\nabla p = -K^{-1} \lambda_T^{-1} \mathbf{u}, \tag{3-18}$$

$$\phi \frac{\partial S_w}{\partial t} + \nabla \cdot (f_w \mathbf{u}) = q_w. \tag{3-19}$$

3.1.3.1 Relative Permeability

The effective permeability of a fluid defines how easily a fluid can flow through the porous medium in the presence of other fluids. The relative permeability is defined as the ratio of the effective permeability to the absolute

permeability of the medium and depends on the fluid saturation, $k_{rn} = f(S_n)$. Considering the complexity of the subsequent analysis, two models of relative permeability were used. The first model is the Corey and Brooks [92] correlation. This model represents the interaction between velocities in wetting and non-wetting phases in porous media, and is widely used in the literature. It is typically obtained through experiments in which rock samples are tested under specific conditions for a specific scenario (pressure, temperature, oil, water, and gas compositions). The relative permeability curves are written as a power-law function of the saturation:

$$k_{rw} = k_{rw}^0 (S_m)^{n_w}, \tag{3-20}$$

$$k_{ro} = k_{ro}^0 (1 - S_m)^{n_o}, \tag{3-21}$$

$$S_m = \frac{S_w - S_{wi}}{1 - S_{wi} - S_{or}}, \tag{3-22}$$

where S_{wi} is the initial water saturation, S_{or} is the irreducible oil saturation, k_{rw}^0 is the water relative permeabilty at the irreducible oil saturation, k_{ro}^0 is the oil relative permeability at the initial water saturation, n_w is the water exponent and n_o is the oil exponent.

A second model is the LET correlation [93]. The relative permeability curves are written as a function of saturation in terms of three parameters. The LET model allows oil mobility to be adjusted at low water saturations while maintaining special core analysis (SCAL) data at high water saturations. At a field scale, this method has been successfully applied to the simulation of oil production from a field in the Norwegian Sea. When compared to the Corey and Brooks model, the LET model has the advantage of a greater degree of freedom. The functional forms of the LET model are:

$$k_{rw} = k_{rw}^0 \frac{(S_m)^{L^w}}{(S_m)^{L^w} + E^w (1 - S_m)^{T^w}}, \tag{3-23}$$

$$k_{ro} = k_{ro}^0 \frac{(S_m)^{L^o}}{(1 - S_m)^{L^o} + E^o (S_m)^{T^o}}, \tag{3-24}$$

where only S_{wi}, S_{or}, k^0_{rw} and k^0_{ro} have a physical meaning. L^n, E^n, and T^n are empirical parameters used to better fit the data.

3.1.4 Buckley–Leverett

The Buckley-Leverett model is used in this study to validate the implementation of the Darcy and Brinkman numerical models. Buckley-Leverett theory [94] refers to the displacement of immiscible two-phase flow within a porous medium. The BL model is built upon assumptions of linear (1-D) flow in an isotropic and homogeneous porous medium, with both fluids considered incompressible. The water injection occurs at a constant rate, i.e., the velocity along the inlet boundary is constant.

Displacement efficiency can be defined as:

$$E_D = \frac{Amout\ of\ oil\ displaced}{Initial\ Amount\ of\ oil\ in\ the\ porous\ medium}. \tag{3-25}$$

Based on the eq. (3-10) and eq. (3-15), mass conservation of the water phase can be written as:

$$\phi \frac{\partial S_w}{\partial t} + \mathbf{u} \frac{\partial f_w}{\partial x} = 0. \tag{3-26}$$

To calculate the displacement efficiency, it is necessary to establish the saturation as a function of position and time, $S_w(x,t)$. The boundary conditions and the initial condition for this problem are:

$$S_w(x,0) = S_{wi}, \quad x \geq 0 \tag{3-27}$$

$$S_w(0,t) = S_{winj}, \quad t \geq 0 \tag{3-28}$$

where S_{winj} is the injection saturation.

The following variables are used to make equation (3-26) dimensionless:

$$x_D = \frac{x}{L}, \tag{3-29}$$

$$t_D = \int_a^t \frac{\mathbf{u}}{\phi L} dt. \tag{3-30}$$

Eq. (3-30) is also referred to as the dimensionless porous volume injected. Thus it is possible to expand equation (3-26) using (3-29) and (3-30) as follows:

$$\frac{\partial S_w}{\partial t_D} + \frac{\partial f_w}{\partial S_w}\frac{\partial S_w}{\partial x_D} = 0. \tag{3-31}$$

Writing eq. (3-31) as total differential equation,

$$dS_w = \frac{\partial S_w}{\partial x_D}dx_D + \frac{\partial S_w}{\partial t_D}dt_D, \tag{3-32}$$

with this it is defined the specific velocity for a given water saturation v_{S_w} in terms of its position and injected pore volumes:

$$\frac{dx_D}{dt_D} = -\frac{\partial S_w/\partial t_D}{\partial S_w/\partial x_D} \equiv v_{S_w}. \tag{3-33}$$

Substituting eq. (3-32) into eq. (3-33) gives:

$$v_{S_w} = \frac{\mathrm{d}f_w}{\mathrm{d}S_w}, \tag{3-34}$$

with this, it is possible to estimate the position of the water advection front along the porous medium as a function of the injected volume for a given $S_w = s$:

$$x_D\big|_{S_w=s} = \left.\frac{\mathrm{d}f_w}{\mathrm{d}S_w}\right|_{S_w=s} t_D. \tag{3-35}$$

Eq. (3-35) can be employed to compute the saturation at a specific position relative to the injection point, considering a predetermined volume of injected fluid as exemplified in figure 3.1.

3.1.5
Single-phase Brinkman Model

Brinkman equation [16] presents a mathematical formulation designed to address the concomitant fluid flow occurring within both a free-flow region and a porous matrix. Notably, the author has successfully incorporated the Stokes diffusion term into Darcy's law. The single-phase Brinkman equation is represent as follows:

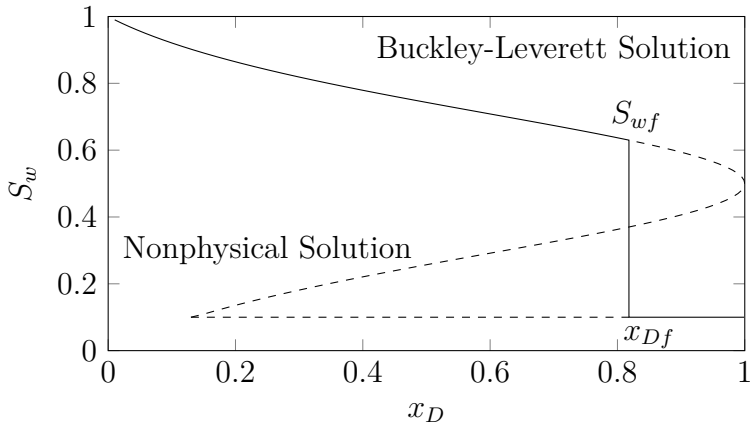

Figure 3.1: Saturation profile obtained in a homogeneous, 1-D porous medium for an arbitrary t_D. S_{wf} is the water front saturation in the x_{Df} position. This profile is obtained through equation (3-35).

$$\nabla p = \mu^* \nabla^2 \mathbf{u} - \frac{\mu}{K}\mathbf{u}, \tag{3-36}$$

where μ^* is denominated the effective Brinkman's viscosity.

Since the porous media is considered isotropic, the tensor is simplified to a scalar in this study. Consequently, the porous matrix attains a real-valued permeability, symbolized by K, while in the vugular domain, K is conceptually infinite.

The determination of the effective Brinkman's viscosity (μ^*) has attracted considerable attention. Several studies suggest different values might be used instead of fluid viscosity. Martys et al., (1994) [95] highlighted an important observation: the effective viscosity parameter is intimately related to the porosity of the porous medium. The porosity of the porous matrix examined ranged from 50% to 80%. It is noteworthy that these values significantly exceed the average porosity levels found in carbonate rock reservoirs, which typically range from 10 to 20 percent. Lundgren (1972) [96] conducted an experiment on a bed of randomly dispersed spheres. During their investigation, they found a significant correlation between medium porosity and effective Brinkman viscosity, specially for elevated porosity values. Neale and Nader (1974) [37] performed an analysis to establish a correlation between the Beavers-Joseph equation and Brinkman viscosities. This correlation was well represented by the model $\alpha_{BJ} = \sqrt{\mu^*/\mu}$. Koplik et al., (1983) [97] indicated that in comparison with pore-fluid viscosity, the effective Brinkman viscosity is inferior. Brinkman formulation captures these effects with remarkable accuracy. This results were reached for high porosity medium. Aurianlt (2009) [98] indicated that the parameter μ^* assumes parity with μ when dealing with

high porosity. Moreover, the Brinkman equation cannot be applied to porous media such as rock samples. Accordingly, Whitaker (1999) [36] presented a concept of porosity correction, which is equivalent to the intrinsic velocity and apparent flow velocity. Gilver and Altobelli (1994) [100] employed nuclear magnetic resonance techniques to explore water flow through structured foams with very high porosity. For a Reynolds number of 17, their experiments reveal that the ratio of Brinkman viscosity to dynamic viscosity oscillates between 5.1 and 10.9. In their study, porosity ($\phi = 0.975$) and advective effects are elevated. Hence, the flow behaviour in carbonate reservoirs is inconsistent with high porosity and high Reynolds number (except near wells). Generally, formulations addressing Brinkman's viscosity term are tailored for high porosity contexts [95, 96, 97, 98, 100], which diverges from the scenario this study aims to investigate. Moreover, various studies present different perspectives on this matter. For instance, [98] suggests the Brinkman viscosity term is equivalent to the fludi viscosity for high porosity, while [95, 97] suggested correction on Brinkman viscosity term for high porosity media. This issue remains an ongoing debate and is not the focus of the present study.

The use of viscosity values that are different from those of the fluid in the free-flow region has several implications. Often, this approach relies on correlations derived from specific porous medium configurations and flow regimes, which do not align with the conditions usually associated with carbonate rock flows. Furthermore, a substantial amount of literature assumes that Brinkman's viscosity corresponds to the fluid viscosity in the free-flow region. According to the literature [14, 17, 58, 57, 101, 53, 55, 54, 59, 102, 18, 38, 39, 40, 41, 60, 45], the most common value for μ^* is the same as the fluid viscosity in the free flow region $\mu^* = \mu$ and $\mu^* = 0$ at the porous matrix region. In addition, the permeability at the free flow region is set as $K \to \infty$, making the Darcy term tending to zero as sketched in figure 3.2.

3.1.6 Two-Phase Brinkman Model

Equation (3-36) is modified to represent the two phase flow. For simplification, it is considered that water and oil have the same density. The velocity in the vug region follows the same assumption as the Darcy total velocity, which is $\mathbf{u} = \mathbf{u}_o + \mathbf{u}_w$. Moreover, a simplified approach is chosen to examine the viscosity of the mixture. This involved computing a saturation-weighted average of individual phases' viscosity. Within the scope of this study, μ^* is set as zero on the matrix domains and it is modeled on the two-phase flow as proportional of each phase saturation locally in the free-flow region:

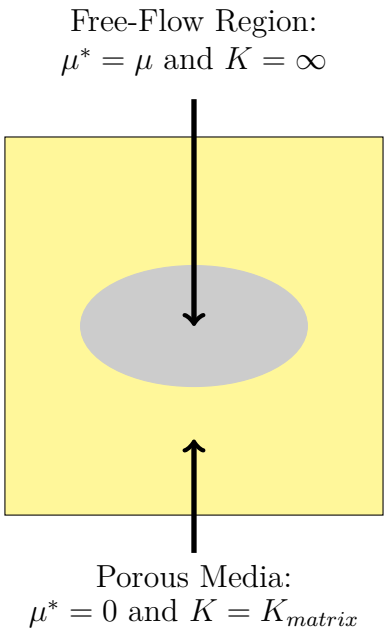

Figure 3.2: Diagram illustrating of the Brinkman model. The yellow region represent the porous matrix and the gray region represents the free-flow region.

$$\mu^* = \mu_o (1 - S_w) + \mu_w S_w. \tag{3-37}$$

Through the imposition of these constraints upon μ^* and K the Darcy term becomes negligible within the vulgular region, while the Stokes term is not considered within the porous matrix.Accordingly, the following set of equations are selected to represent the Brinkman two-phase flow:

$$\nabla p = \mu^* \nabla^2 \mathbf{u} - \frac{\mathbf{u}}{K \lambda_T}, \tag{3-38}$$

$$\nabla \cdot \mathbf{u} = q, \tag{3-39}$$

$$\phi \frac{\partial S_w}{\partial t} + \nabla \cdot (f^* \mathbf{u}) = q_w, \tag{3-40}$$

where f^* must be define differently for the free-flow region and the porous matrix. In the porous matrix region $f^* = f_w$. In the free-flow domain, the velocity of each phase is considered to be a linear function of the phase saturation. Therefore, the free-flow region has $f^* = S_w$ for the water phase.

This approach was employed based on the experimental observations of Romm (1966) [99]. Analogously, it is similar to considering a relative permeability curve in $\times$.

As similar to the Darcy two-phase model, Corey and Brooks relative permeability correlation [92] is used to characterize the two-phase flow in the porous matrix, where the irreducible water saturation and residual oil saturation are both assumed to be zero and Brooks exponents are $n_w = 2$ and $n_o = 2$, respectively. Furthermore, the endpoints of relative permeability, k_{ro} at $S_w = 0$ and k_{rw} at $S_w = 1$, both have values of one.

Modeling flow within the free-flow depends on several simplified assumptions. However, as far as the author knowledge, there is no clear approach to how phase velocity and phase viscosity should be treated appropriately for flow in free-flow region interacting with the porous medium. Currently, this issue remains unresolved.

3.2 Flow Domain, Initial and Boundary Conditions

In this study, different vug configurations are used to evaluate the behavior of a two-phase flow in highly heterogeneous rectangular porous media. In all the cases, the domain is initially saturated by non-wetting phase, oil (o), being displaced by the injection of a wetting phase, water (w). Figure 3.3 represents a sketch of the flow domain. $\Omega \subset \mathbb{R}^2$ is a rectangle representing a porous medium containing vugs. The porous matrix domain Ω_M and the vug domain Ω_V are defined as such: $\Omega = \Omega_M \cup \Omega_V$ and $\Omega_M \cap \Omega_V = \varnothing$.

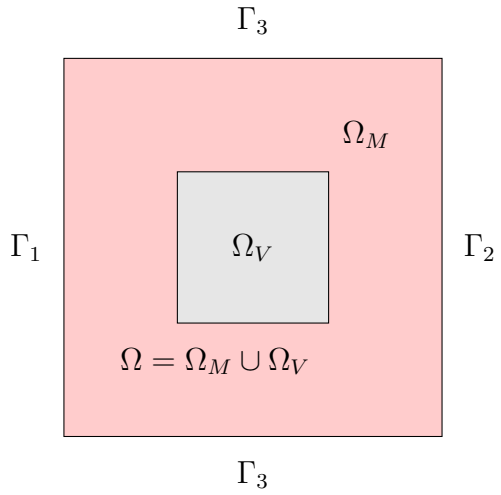

Figure 3.3: Schematic representation of the computational domains and their boundaries conditions.

Water is injected through the left inlet boundary at a constant velocity,

i.e $\mathbf{u} = \mathbf{u}_{in}$ and $S_w = 1$ along Γ_1 in figure 3.3. The pressure in the outlet boundary is constant, $p = p_{out}$ along Γ_2. The top and botton boundaries are considered impermeable, $\mathbf{u} \cdot \mathbf{n} = 0$ on Γ_3, i.e:

$$S_w = 0 \; at \quad t = 0, \tag{3-41}$$

$$S_w = 1 \; on \quad \Gamma_1 \tag{3-42}$$

$$\mathbf{u} = \mathbf{u}_{in} \; on \quad \Gamma_1 \tag{3-43}$$

$$\mathbf{u} \cdot \mathbf{n} = 0 \; on \quad \Gamma_3, \tag{3-44}$$

$$p = p_{out} \; on \quad \Gamma_2. \tag{3-45}$$

3.3 Numerical Implementation

The finite element method (FEM) is used for solving the partial differential equations (PDE) associated with the different models described in the previous session. The continuous problem is converted into a discrete system of equations to approximate the solution. An effective implementation of the method requires an accurate representation of the geometry by finite elements. The quality of the mesh is essential to the success of the solution. Sections (3.5.1) and (3.5.2) discuss mesh generation in detail. The weak form is obtained by multiplying the original PDE by a weight function and integrating into the problem domain. This procedure converts a differential equation into an algebric system of equation. The coefficients of the approximate solution's expansion in terms of the basis functions constitute the unknowns of the discrete problem. The functions are restricted to specific local regions within the domain, resulting in a sparse linear system.

It is possible to solve the Brinkman and Darcy equations numerically by selecting the appropriate set of basis functions according to the particularities of each set of equations. The type of elements and the order of the basis functions play an important role in the accuracy and efficiency of a finite element analysis. The Mixed Finite Element Method (MFEM) is chosen for the solution of the pressure and velocity fields for Brinkman and Darcy equations. The MFEM is an extension of the classical FEM. In particular, it is well suited to the solution of problems involving coupled or interrelated physical phenomena. A major advantage of MEFM over FEM in the context of this study is that MEFM is locally conservative, which is essential for numerical stability for solving the equations that are proposed.

A first attempt was made to model Brinkman's two-phase problem

using Taylor-Hood elements for the velocity and pressure fields, and the Discontinuous Galerkin method for the saturation field, based on Dali [40], Cruz [41], and Campos [60] single-phase investigation. However, it was not possible to obtain a numerical solution for the saturation field. Although Taylor-Hood basis functions can solve the single-phase Brinkman problem without significant issues, this modeling approach lacks local conservation at the element level. Consequently, these non-conservative effects introduce numerical errors into the saturation field, leading to inherently non-physical outcomes such as water saturation exceeding one.

In MFEM, the velocity and pressure fields are expanded in terms of different sets of basis functions. Far Darcy's equations, it is used Raviart-Thomas (RT) and Discontinuous Galerkin (DG) for velocity and pressure fields, respectively. In Brinkman formulation, the velocity field is expanded using Brezzi-Douglas-Marini (BDM) functions, whereas the pressure field is expanded using Discontinuous Galerkin method. The saturation field is discretized by the DG method in both formulations. Raviart-Thomas basis functions are commonly used to solve vector fields problems. The basis functions associated with RT_0 are piecewise constant vector functions defined on the edges or faces of the elements. The basis functions point outward from the centroids of the faces or edges and are chosen to ensure compatibility and accuracy when estimating constant vector fields. These basis functions are commonly used to model the Darcy equation [103]. RT_0 has three degrees of freedom and BDM_1 is used to expand the velocity field in the Brinkman formulation and the pressure field is modeled using the Discontinous Galerking method of zero order (DG_0). RT_0 and BMD_1 basis functions are described in more detail below.

RT and BDM are frequently used as approximation spaces $H_{div}(\Omega)$, which definition is

$$H_{div}(\Omega) = \left\{ \boldsymbol{u} = (u_1, u_2)\, \epsilon \left(L^2(\Omega) \right)^2 \mid \nabla \cdot \boldsymbol{u} \;\; \epsilon\, L^2(\Omega) \right\}. \tag{3-46}$$

The Ω computational domain is described using triangles in this study. Assume that $\mathcal{T}_h$ represent a regular triangulation of Ω, where $\mathcal{T}_h$ corresponds to the mesh elements of T , $\mathcal{E}_h$ represents the interior edges of $\mathcal{T}_h$, and $\mathcal{P}_k(T)$ describes the space of bivariate polynomials of degree $\leq k$ on T.

A description of the basis functions for RT_k is provided first, where

$$RT_k(T) = (\mathcal{P}_k(T))^2 + \mathbf{x}\mathcal{P}_k(T), \tag{3-47}$$

and the RT_k approximation space is defined by

$$\begin{aligned} RT_k(\Omega) &= \{\mathbf{u}_h \mid \mathbf{u}_h \in RT_k(T)\ \forall T\ \in \mathcal{T}_h, \\ &\quad \mathbf{u}_h \cdot \mathbf{n}_{ij} \text{ is continuous across } e_{ij},\ \forall e_{ij} \in \mathcal{E}_h\} \end{aligned} \tag{3-48}$$

where e_{ij} is the edge of $\mathcal{E}_h$ and $\mathbf{n}_{ij}$ is a unit vector to e_{ij}.

The next step is to describe the basis functions for BDM. The $BDM_k(\Omega)$ approximating space is defined as follows:

$$\begin{aligned} BDM_k(\Omega) &= \{\mathbf{u}_h \mid \mathbf{u}_h \in BDM_k(T)\ \forall T\ \in \mathcal{T}_h, \\ &\quad \mathbf{u}_h \cdot \mathbf{n}_{ij} \text{ is continuous across } e_{ij},\ \forall e_{ij} \in \mathcal{E}_h\} \end{aligned} \tag{3-49}$$

where basis functions for BDM_k

$$BDM_k((T) = (\mathcal{P}_k(T))^2, \tag{3-50}$$

Most commonly in RT_k and BDM_k spaces continuity for $\mathbf{u}_h \cdot \mathbf{n}_{ij}$ across $e_{ij} \in \mathcal{E}_h$ can be illustrated graphically by showing degrees of freedom for $\mathbf{u}_h \cdot \mathbf{n}$ on the edges of $T \in \mathcal{T}_h$. Figure 3.4 illustrates the degree of freedom for RT_0 and BDM_1. Finite Element computations impose restrictions on the test space by selecting the appropriate basis functions. As part of these restrictions, the derivatives of the approximation must be continuous. Additionally, the basis functions exhibit a Lagrangian property in that their value is at their nodal point, and their value vanishes at all other nodes. In order to compute the basis functions, the integrals over $T \in \mathcal{T}_h$are transformed into integrals over $\hat{T}$, where $\hat{T}$ represents the reference triangle on which the basis functions are defined. The vertices of the triangle $\hat{T}$ are: (0,0), (1,0), and (0,1). Edge numbers for $\hat{T}$ are: edge 1 pertains to the edge opposite vertex (0, 0), edge 2 pertains to the edge opposite vertex (1, 0), and edge 3 pertains to the edge opposite vertex (0, 1). An edge's normal basis functions are called φ^i, where φ^i is a vector. To clarify, $\mathbf{n}_k$, where $k = 1, 2, 3$, describes the outer unit normal to each edge of $\hat{T}$. Accordingly, $\varphi^i \cdot \mathbf{n}_k = 0$, along the edge k for $i \neq k$. As a result, $RT_0(\hat{T})$ the basis functions are:

$$\hat{\mathbf{e}}_1(\xi, \eta) = \sqrt{2} \begin{bmatrix} \xi \\ \eta \end{bmatrix} \tag{3-51}$$

$$\hat{\mathbf{e}}_1(\xi,\eta) = \begin{bmatrix} \xi - 1 \\ \eta \end{bmatrix} \tag{3-52}$$

$$\hat{\mathbf{e}}_1(\xi,\eta) = \begin{bmatrix} \xi \\ \eta - 1 \end{bmatrix} \tag{3-53}$$

$$\varphi^1 = \hat{\mathbf{e}}_1(\xi,\eta), \quad \varphi^2 = \hat{\mathbf{e}}_2(\xi,\eta), \quad \varphi^3 = \hat{\mathbf{e}}_3(\xi,\eta). \tag{3-54}$$

The basis functions of $BDM_1(\hat{T})$ are:

$$\hat{\mathbf{e}}_1(s_1,s_2) = \frac{\sqrt{2}}{s_2 - s_1} \begin{bmatrix} s_2\xi \\ (s_2-1)\eta \end{bmatrix} \tag{3-55}$$

$$\hat{\mathbf{e}}_1(s_1,s_2) = \frac{1}{s_2 - s_1} \begin{bmatrix} s_2\xi + \eta - s_2 \\ \eta(s_2-1) \end{bmatrix} \tag{3-56}$$

$$\hat{\mathbf{e}}_1(s_1,s_2) = \frac{1}{s_2 - s_1} \begin{bmatrix} \xi(s_2-1) \\ \xi + s_2\eta - s_2 \end{bmatrix} \tag{3-57}$$

According to the proposed model, $g_1 = 1/2 - \sqrt{3}/6$ and $g_2 = 1/2 + \sqrt{3}/6$ correspond to two Gaussian quadrature points on the interval [0,1], where $BDM_1(\hat{T})$ basis functions are:

$$\varphi_1^1 = \hat{\mathbf{e}}_1(g_1,g_2), \quad \varphi_2^1 = \hat{\mathbf{e}}_1(g_2,g_1), \tag{3-58}$$

$$\varphi_1^2 = \hat{\mathbf{e}}_2(g_2,g_1), \quad \varphi_2^2 = \hat{\mathbf{e}}_2(g_1,g_2), \tag{3-59}$$

$$\varphi_1^3 = \hat{\mathbf{e}}_3(g_1,g_2), \quad \varphi_2^3 = \hat{\mathbf{e}}_3(g_2,g_1), \tag{3-60}$$

Discontinuous Galerkin (DG) method is used to solve partial differential

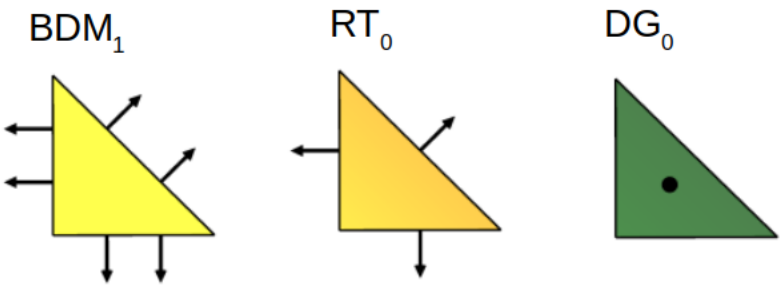

Figure 3.4: An illustration of all degrees of freedom (Dof) of the Brezzi-Douglas-Marini of first order basis functions (BDM_1), Raviart-Thomas zero order basis functions (RT_0) and the Discontinous Galerking method of zero order basis functions (DG_0). Adapted from [106]

equations (PDEs) with discontinuities between adjacent elements. The DG method offers significant advantages, including conservation at the elemental level, adaptability to intricate geometries using high-order approximations, reduced numerical dispersion, when appropriate slope limiters are used, and spurious oscillations are prevented. This method is based on the ability to select basis functions based on any field variable, its derivatives, or both that are discontinuous across element boundaries while maintaining the global domain continuity. Discontinuous Galerkin methods utilize the same space functions as continuous Galerkin methods, but with a relaxed continuity between elements. DG methods involve the application of both test and basis functions marked by discontinuities at region interfaces. This approach provides enhanced flexibility, allowing for accurate encapsulation of discontinuities in the solution. The method is particularly effective in scenarios involving heterogeneous materials, interfaces delineating distinct regions, or non-continuous behaviors. A DG method is suitable when dealing with hyperbolic equations, such as the saturation eq. (3-40). Figure 3.5 sketches the representation of a DG_2 model, where it can be seen that the degree of freedom of two adjacent elements are not common in the element boundaries.

Discontinuous Galerkin methods are designed to accommodate functions that exhibit discontinuous behavior across certain interfaces within the domain. It is assumed that the same triangulation as RT and BDM of the Ω domain. To fully characterize the Discontinuous Galerkin (DG) method, it is necessary to provide additional definitions. In the case of element T, h_E is the diameter of the circle circumscribed in T. F is a mesh face or edge, where there are two different mesh elements T_1 and T_2 such that $F = \partial T_1 \cap \partial T_2$. If it is a boundary element $F = \partial T_1 \cap \Gamma$. It is also important to define the interface jumps and averages. Let g be any smooth scalar function,

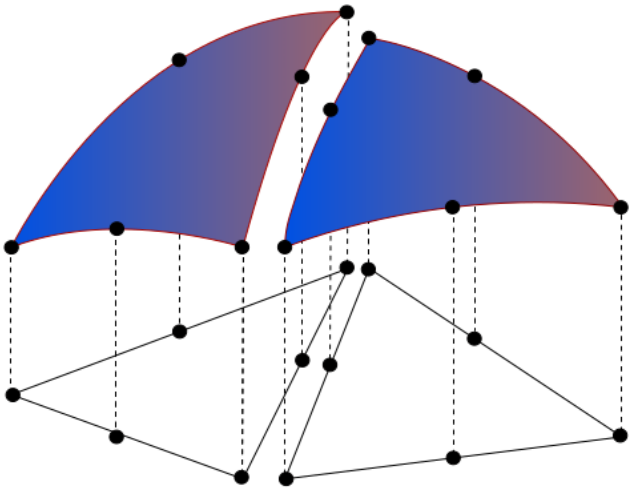

Figure 3.5: Schematic degrees of freedom (Dof) of a second order discontinuous Galerkin finite element. All Dof are internal to the element [106].

$$\{g\} = \frac{1}{2}\left(g|_{T_1} + g|_{T_2}\right), \tag{3-61}$$

$$[g] = g|_{T_1} - g|_{T_2}, \tag{3-62}$$

where $[\cdot]$ and $\{\cdot\}$ are defined as the jump and average operators thought the edge F, respectively. The DG_k approximation space is defined by

$$DG_k(\Omega) = \left\{\mathbf{u}_h \mid \mathbf{u}_h \in L^2(\Omega) \mid \forall T \ \in \mathcal{T}_h, \mathbf{u}_h \mid_T \in DG_k(T)\right\}, \tag{3-63}$$

The basis functions of $DG_0(\hat{T})$ are defined as follows. In accordance with the definition of the vertices of the elementary triangle $\hat{T}$,

$$\omega_1(\xi, \eta) = 1, \tag{3-64}$$

where ω_1 is a scalar function.

Implicit Pressure Explicit Saturation (IMPES) algorithm is used to time integrate the system of nonlinear equations governing two-phase flow in both Brinkman and Darcy models [101, 104]. This method is simple to implement, has extensive use in literature, the computational cost is relatively low when compared to alternative approaches such as the simultaneous solution [107],

and it has recognized accuracy.

The numerical solution is implemented using the FEniCS platform, which is an open-source library designed to automate the computation of partial differential equations (PDEs) through finite element methods. These libraries are efficiently implemented in C++ and can be managed with C++ or Python language [105]. The DOLFIN library is part of FEniCS and compile linear systems composed of tensors of different ranks on meshes extending up to three spatial dimensions. It is flexible enough to accommodate a wide range of variational formulations and basis functions.

3.3.1 Weak Form of the Two-Phase Darcy Model

In this section, the weak formulation of the Darcy equation is presented. Equations (3-17), (3-18), and (3-19) are discretized through the mixed finite element method for velocity and pressure. The velocity field and the pressure filed are described by RT_0 and DG_0. Discountiouns Galerkin method of order zero was adopted to describe the saturation field. Additionally, the upwind method, equation (3-78), is used to ensure numerical stability of the water phase saturation equation (3-77). It is assumed that the porosity in the vugular region is set to $\phi_V = 1$ and that the permeability in the vugular region is set to an arbitrary high value. Brinkman's model and Darcy's model are consistent with respect to the relative velocities for each phase within the vug domain. This consistency was achieved by incorporating the study conducted by Romm (1966) [99], wherein the relative permeability curve was adopted as the $\times$ shape in the Darcy model, i.e. n_o and n_w are set as one. This approach has been utilized by Hussien (2012) [108], Yan et al., (2016) [62], and Machado et al., (2020) [110] in their investigations of two-phase flow within vugs. In the vugs the S_{wi} and S_{or} are also considered zero.

As a first step, the weak form of Darcy velocity eq. (3-18) is presented. The eq. (3-18) is multiplied by the weight function $\mathbf{v}$

$$\int_\Omega \frac{\mathbf{u}_h^n}{K\lambda\left(S_{wh}^n\right)} \cdot \mathbf{v} dx + \int_\Omega \nabla p_h^n \cdot \mathbf{v} dx = 0, \tag{3-65}$$

where the superscript n is any time step. Integrating by parts the second term of the eq. (3-65)

$$\int_\Omega \nabla p_h^n \cdot \mathbf{v} \partial\Omega = \int_\Omega \nabla \cdot \left(\mathbf{v} \cdot p_h^n\right) \partial\Omega - \int_\Omega p_h^n \cdot \left(\nabla \cdot \mathbf{v}\right) \partial\Omega \tag{3-66}$$

Applying the Gauss-Green theorem to the first term on the right-hand side,

$$\int_{\Omega} \nabla \cdot (\mathbf{v} \cdot p_h^n)\, \partial\Omega = \int_{\Gamma} \mathbf{n} \cdot (p_h^n \cdot \mathbf{v})\, \partial s, \tag{3-67}$$

where ∂s represents the integration over the boundary. As a result, the equation weak form is

$$\int_{\Omega} \left(\frac{\mathbf{u}_h^n}{K\lambda_T\left(S_{wh}^n\right)} \right) \cdot \mathbf{v}\, \mathrm{d}x - \int_{\Omega} p_h^n \nabla \cdot \mathbf{v}\ \, \mathrm{d}x + \int_{\Gamma} \mathbf{n} \cdot (\mathbf{v}\ p_h^n)\ \, \mathrm{d}s = 0. \tag{3-68}$$

The weak form of mass conservation is given by:

$$\int_{\Omega} (\nabla \cdot \mathbf{u}_h^n)\, q\ \partial\Omega = 0 \tag{3-69}$$

where q is the weight function.

It is necessary to obtain the weak form of the equation for water phase conservation. Using eq. (3-19), a temporal discretization is performed using the finite difference method with explicit discretization of time

$$\phi \frac{S_{wh}^{n+1} - S_{wh}^n}{\Delta t} = \nabla \cdot \left(f_w\left(S_w^n\right) \mathbf{u}_h^n \right). \tag{3-70}$$

Multiplying eq. (3-70) by the weight function r and integrating on Ω,

$$\int_{\Omega} \phi S_{wh}^{n+1} r \partial\Omega - \int_{\Omega} \phi S_{wh}^n r \partial\Omega = \Delta t \int_{\Omega} \nabla \cdot \left(f_w\left(S_{wh}^n\right) \mathbf{u}_h^n \right) r \partial\Omega. \tag{3-71}$$

Integrating by parts the last term of the eq. (3-71),

$$\int_{\Omega} \nabla \cdot \left(f_w\left(S_{wh}^n\right) \mathbf{u}_h^n \right) r \partial\Omega = \int_{\Omega} \nabla \left(f_w\left(S_{wh}^n\right) \mathbf{u}_{\mathbf{h}}^{\mathbf{n}} \right) r \partial\Omega - \int_{\Omega} \nabla r f_w\left(S_{wh}^n\right) \mathbf{u}_h^n \partial\Omega, \tag{3-72}$$

and applying the Gauss-Green theorem to the first term on the right-hand side,

$$\int_{\Omega} \nabla \left(f_w\left(S_{wh}^n\right) \mathbf{u}_h^n \right) r \partial\Omega = \int_{\Gamma} \mathbf{n} \cdot \mathbf{u}_h^n f_w\left(S_{wh}^n\right) r \partial s \tag{3-73}$$

this term encapsulates the numerical flows at both the element interface and domain boundary. The water phase conservation equation is modeled using

the *DG* method, which requires this term to be integrated at the boundary domain and between each element. Moreover, it is employed the upwind model to designate the upstream cell for saturation calculation. It is only possible to achieve numerical stabilization by applying upwind. Thus,

$$\begin{aligned}\int_{\Gamma} \mathbf{n}\cdot\mathbf{u}_h^n f_w\left(S_{wh}^n\right) r\partial s &= \sum_{i=1}^{3}\int_{\Gamma_i} \mathbf{n}\cdot\left\{f_w\left(S_{wh}^n\right)_{\Gamma 1}\ \mathbf{u}_h^n\right\}_{up} r\partial s \\ &+ \int_{\partial\mathcal{T}^1} \mathbf{n}\cdot\left\{f_w\left(S_{wh}^n\right)_{\Gamma 1}\ \mathbf{u}_h^n\right\}_{up} r\partial S \\ &+ \int_{\partial\mathcal{T}^2} \mathbf{n}\cdot\left\{f_w\left(S_{wh}^n\right)_{\Gamma 1}\ \mathbf{u}_h^n\right\}_{up} r\partial S, \end{aligned} \tag{3-74}$$

where ∂S is the integration over the element boundary. The last two terms of the above equation can be handled as,

$$\begin{aligned}&\int_{\partial\mathcal{T}^1} \mathbf{n}\cdot\left(f_w\left(S_{wh}^n\right)_{\Gamma 1}\ \mathbf{u}_h^n\right)_{up} r\partial S + \int_{\partial\mathcal{T}^2} \mathbf{n}\cdot\left(f_w\left(S_{wh}^n\right)_{\Gamma 1}\ \mathbf{u}_h^n\right)_{up} r\partial S \\ &= \sum_{E\in\varepsilon_h}\int_E [r]\cdot\left\{\left(f_w\left(S_{wh}^n\right)\mathbf{u}_h^n\right)_{up}\right\}\ \mathrm{d}S\end{aligned} \tag{3-75}$$

Furthermore, the saturation at the inlet boundary is weakly imposed

$$\Delta t\int_{\Gamma_1} r\cdot\left(f_w\left(S_{wh}^n\right)_{\Gamma 1}\ \mathbf{u}_h^n\right)_{up}\mathrm{d}s. \tag{3-76}$$

Therefore, the saturation equation can be expressed as follows:

$$\begin{aligned}&\phi\int_{\Omega}\left(S_{wh}^{n+1}-S_{wh}^n\right) r\mathrm{d}x - \Delta t\int_{\Omega}\nabla r\cdot f_w\left(S_{wh}^n\right)\mathbf{u}_h^n\ \mathrm{d}x \\ &+\Delta t\int_{\Gamma} r\cdot\left(f_w\left(S_{wh}^n\right)\mathbf{u}_h^n\right)_{up}\ \mathrm{d}s + \Delta t\sum_{E\in\varepsilon_h}\int_E [r]\cdot\left\{\left(f_w\left(S_{wh}^n\right)\mathbf{u}_h^n\right)_{up}\right\}\ \mathrm{d}S \\ &+\Delta t\int_{\Gamma_1} r\cdot\left(f_w\left(S_{wh}^n\right)_{\Gamma 1}\ \mathbf{u}_h^n\right)_{up}\mathrm{d}s = 0\end{aligned} \tag{3-77}$$

and the upwind is defined as:

$$\left(f_w\left(S_{wh}^n\right)\mathbf{u}_h^n\right)_{up} = \begin{cases}\left(f_w\left(S_{wh}^n\right)\ \mathbf{u}_h^n\right)_{\tau_{h_1}}, & \text{if } \boldsymbol{u}\cdot\boldsymbol{n}\geq 0,\\ \left(f_w\left(S_{wh}^n\right)\ \mathbf{u}_h^n\right)_{\tau_{h_2}}, & \text{if } \boldsymbol{u}\cdot\boldsymbol{n}\geq 0,\end{cases} \tag{3-78}$$

Therefore, the weak form of the set of differential equations for the Darcy two-phase flow is written as:

$$\int_{\Omega}\left(\frac{\mathbf{u}_h^n}{K\lambda_T\left(S_{wh}^n\right)}\right)\cdot\mathbf{v}\,\mathrm{d}x - \int_{\Omega} p_h^n\nabla\cdot\mathbf{v}\ \mathrm{d}x + \int_{\Gamma}\mathbf{n}\cdot\left(\mathbf{v}\ p_h^n\right)\ \mathrm{d}s = 0. \tag{3-79}$$

$$\int_{\Omega} \left(\nabla \cdot \mathbf{u}_h^n\right) q \mathrm{d}x = 0 \tag{3-80}$$

$$\begin{aligned} &\phi \int_{\Omega} \left(S_{wh}^{n+1} - S_{wh}^{n}\right) r \mathrm{d}x - \Delta t \int_{\Omega} \nabla r \cdot f_w\left(S_{wh}^{n}\right) \mathbf{u}_h^n \, \mathrm{d}x \\ &+ \Delta t \int_{\Gamma} r \cdot \left(f_w\left(S_{wh}^{n}\right) \mathbf{u}_h^n\right)_{up} \, \mathrm{d}s + \Delta t \sum_{E \in \varepsilon_h} \int_{E} [r] \cdot \left\{\left(f_w\left(S_{wh}^{n}\right) \mathbf{u}_h^n\right)_{up}\right\} \, \mathrm{d}S \\ &+ \Delta t \int_{\Gamma_1} r \cdot \left(f_w\left(S_{wh}^{n}\right)_{\Gamma 1} \ \mathbf{u}_h^n\right)_{up} \mathrm{d}s = 0 \end{aligned} \tag{3-81}$$

3.3.2 Weak Form of the Two-Phase Brinkman Model

A mixed finite element method is used to obtain the solution for velocity and pressure. It is used BDM_1 for the velocity field, while DG_0 is used for the pressure field. BDM is an H(div)-conforming basis function space, thus the normal component of velocity is continuous on inter-element boundaries. Thus, it is necessary to adapt the BDM_1 space to ensure continuity of the tangential velocity from one element to another, since the Brinkman equation combines simultaneously the Darcy and Stokes equations. Based on Juho et al. (2011) [111], where the BDM basis functions have been modified to ensure the conservation of the tangential velocity component across elements, it is possible to employ such basis functions for description. The author used the the Symmetric Interior Penalty Galerkin (SIPG) or the Nitsche method [109, 103] method to ensure conservation of the tangential component of velocity. In eq. (3-86), the penalty term is expressed by

$$\sum_{E \in \varepsilon_h} \int_{E} \left(\frac{\gamma}{h_E} [\mathbf{u}_h] \cdot [\mathbf{v}] - \left\{ \frac{\partial \mathbf{u}_h}{\partial n} \right\} \cdot [\mathbf{v}] - \left\{ \frac{\partial \mathbf{v}}{\partial n} \right\} \cdot [\mathbf{u}_h] \right) \mathrm{d}S \tag{3-82}$$

where γ is the positive penalty parameter and dS refers to the element boundary. The selection of γ must be adjusted in accordance with the mesh configuration. In chapter 4 and 5, a detailed discussion of determining the appropriate value for γ is provided.

The saturation field is described using DG_0. Furthermore, the upwind method, eq. (3-78), is used the ensure numerical stability of the water phase saturation eq. (3-16). Accordingly, the discretization of the saturation and mass conservation equations follows the approach employed in the Darcy model eq. (3-80) and eq. (3-77). Therefore, it is presented the weak form of the Brinkman equation. Initially, the first term of the equ. (3-38) is integrated in parts,

$$-\int_{\Omega}\mu^{*}\nabla^{2}\mathbf{u}\ \mathbf{v}\partial\Omega=\int_{\Omega}\mu^{*}\nabla\mathbf{u}\cdot\nabla\mathbf{v}\partial\Omega\ -\int_{\Omega}\mu^{*}\nabla\cdot\left(\mathbf{v}\nabla\mathbf{u}\right)\partial\Omega. \tag{3-83}$$

Applying the divergence theorem to the last term of eq. (3-85),

$$\int_{\Omega}\mu^{*}\nabla\cdot\left(\mathbf{v}\nabla\mathbf{u}\right)\partial\Omega=\int_{\Gamma}\mu^{*}\mathbf{n}\cdot\left(\mathbf{v}\nabla\mathbf{u}\right)\partial s=0. \tag{3-84}$$

Thus, it is obtained the weak form of linear momentum diffusion,

$$-\int_{\Omega}\mu^{*}\nabla^{2}\mathbf{u}\ \mathbf{v}\partial\Omega=\int_{\Omega}\mu^{*}\nabla\mathbf{u}\cdot\nabla\mathbf{v}\partial\Omega \tag{3-85}$$

The remaining terms of the weak form of the Brinkman equation are eq. (3-79). The weak form of Brinkman eq.(3-86), total mass conservation eq. (3-87) and water saturation eq.(3-88) are respectively,

$$\begin{aligned}&\int_{\Omega}\mu^{*}\left(\nabla\mathbf{u}_{h}^{n}\cdot\nabla\mathbf{v}\right)\,\mathrm{d}x+\int_{\Omega}\left(\frac{\mathbf{u}_{h}^{n}}{K\lambda_{T}\left(S_{w}^{n}\right)}\right)\cdot\mathbf{v}\,\mathrm{d}x\\&-\int_{\Omega}p_{h}^{n}\nabla\mathbf{v}\ \,\mathrm{d}x+\int_{\Gamma}n\cdot\left(\mathbf{v}\ p_{h}^{n}\right)\,\mathrm{d}s\\&+\sum_{E\in\varepsilon_{h}}\int_{E}\left(\frac{\gamma}{h_{E}}\left[\mathbf{u}_{h}\right]\cdot\left[\mathbf{v}\right]-\left\{\frac{\partial\mathbf{u}_{h}}{\partial n}\right\}\cdot\left[\mathbf{v}\right]-\left\{\frac{\partial\mathbf{v}}{\partial n}\right\}\cdot\left[\mathbf{u}_{h}\right]\right)\mathrm{d}S=0\end{aligned} \tag{3-86}$$

$$\int_{\Omega}\left(\nabla\cdot\mathbf{u}_{h}^{n}\right)q\mathrm{d}x=0 \tag{3-87}$$

$$\begin{aligned}&\phi\int_{\Omega}\left(S_{wh}^{n+1}-S_{wh}^{n}\right)r\mathrm{d}x-\Delta t\int_{\Omega}\nabla r\cdot f_{w}\left(S_{wh}^{n}\right)\mathbf{u}_{h}^{n}\,\mathrm{d}x\\&+\Delta t\int_{\Gamma}r\cdot\left(f_{w}\left(S_{wh}^{n}\right)\mathbf{u}_{h}^{n}\right)_{up}\,\mathrm{d}s+\Delta t\sum_{E\in\varepsilon_{h}}\int_{E}\left[r\right]\cdot\left\{\left(f_{w}\left(S_{wh}^{n}\right)\mathbf{u}_{h}^{n}\right)_{up}\right\}\,\mathrm{d}S\\&+\Delta t\int_{\Gamma_{1}}r\cdot\left(f_{w}\left(S_{wh}^{n}\right)_{\Gamma1}\ \mathbf{u}_{h}^{n}\right)_{up}\mathrm{d}s=0\end{aligned} \tag{3-88}$$

3.3.3
Weak Form of the Two-Phase Stokes Model

The Stokes equation is a limiting scenario of the Brinkman equation within the free-flow region. Through the process of model validation, discussed in section (3.6.2), the validity of the Stokes case is established through a straightforward configuration involving creep flow between two stationary

parallel plates. The imposition of the Dirichlet boundary condition (3-44) encountered limitations due to the use of the BDM_1 basis function. The Dirichlet condition ensures the normal component of the velocity field for this element. An alternative approach is required to accurately enforce the tangential component of the velocity field on Γ_3. Accordingly, Nitsche's method [109] is adopted to weakly enforce the non-slip boundary condition for the Stokes equation. The weak formulation of the Stokes equation adapted to consider the BDM_1 element, i.e:

$$\begin{aligned}
&\int_\Omega \mu^* \left(\nabla \mathbf{u}_h^n \cdot \nabla \mathbf{v}\right) \mathrm{d}x - \int_\Omega p_h^n \nabla \mathbf{v} \ \mathrm{d}x + \int_\Gamma n \cdot \left(\mathbf{v}\ p_h^n\right) \mathrm{d}s \\
&+ \sum_{E \in \varepsilon_h} \int_E \left(\frac{\alpha}{h_E} \left[\mathbf{u}_h\right] \cdot \left[\mathbf{v}\right] - \left\{ \frac{\partial \mathbf{u}_h}{\partial n} \right\} \cdot \left[\mathbf{v}\right] - \left\{ \frac{\partial \mathbf{v}}{\partial n} \right\} \cdot \left[\mathbf{u}_h\right] \right) \mathrm{d}S \\
&+ \frac{\alpha}{h} \int_{\Gamma_2} (\boldsymbol{v} \otimes \mathbf{n}) : (\boldsymbol{u} \otimes \mathbf{n}) \mathrm{d}s - \int_{\Gamma_2} \nabla \mathbf{u} : (\boldsymbol{v} \otimes \mathbf{n}) \mathrm{d}s \\
&- \int_{\Gamma_2} \nabla \boldsymbol{v} : (\boldsymbol{u} \otimes \mathbf{n}) \mathrm{d}s = 0.
\end{aligned} \tag{3-89}$$

The Stokes equation is solved by the MFEM method. Consequently, it is necessary to simultaneously solve the weak mass conservation eq. 3-87 with eq. (3-89),

3.4 Comparative Studies Between Brinkman and Darcy Model

The objective of this investigation is to simulate flow in intricate geometries at the fine scale with greater detail using both Brinkman and a heterogeneous Darcy model and to derive equivalent properties for the coarse scale. The following outlines the methodologies employed to achieve these objectives.

3.4.1 Heterogeneous Single-Continuum Darcy Model

The objective of comparing the Brinkman model with the heterogeneous $1\phi1k$ Darcy model on the same scale is to evaluate the importance of viscous dissipation in the free-flow region, which is not take into account in the heterogeneous Darcy model. The results show the set petrophysical properties of the vugular region that approximates the Brinkman solution. The first step is to establish the porosity of the vugular region ($\phi^\epsilon_{\Omega_V}$), which is considered as one for all cases. The next step involves establishing the absolute permeability for the vug region. Using the equivalent absolute permeability evaluated from the Brinkman solution $K^{eq}_{1\phi1k}$, it is possible to determine the absolute permeability for the vug region using the heterogeneous $1\phi1k$ Darcy model. The K^ϵ_M is kept constant while K^ϵ_V is modified until the error reaches a minimum value.

The superscript ϵ is used here to define the properties on the fine scale. This concept is detailed in the next section.

3.4.2 Upscaling Methods

This study aims to develop methods for accurately describing two-phase flow in a porous matrix containing vugs and fractures using a homogeneous Darcy model, achieved through history matching approaches. As part of history matching, petrophysical properties are modified to ensure the coarse-scale results represent the fine-scale results correctly. It is important to mention that the approach presented here is not intended to handle a direct transition from a core scale to a reservoir scale. The idea of treating an entire reservoir as homogeneous is not recommended. The method is aimed to determine equivalent petrophysical properties of a cell or a limited region of a reservoir model that contain vug and fractures.

3.4.2.1 Equivalent Properties of the Single-Continuum Model

Firstly, the methodology for the generation of the equivalent petrophysical properties (upscaling) for the simple-continuous model is presented. Accordingly, the fine scale flow is described by eq. (3-38), (3-39), and (3-40) are as follows:

$$\nabla p^{\epsilon} = \mu^{*} \nabla^{2} \mathbf{u}^{\epsilon} - \frac{\mathbf{u}^{\epsilon}}{K^{\epsilon} \lambda_{T}^{\epsilon}}, \tag{3-90}$$

$$\nabla \cdot \mathbf{u}^{\epsilon} = 0, \tag{3-91}$$

$$\phi^{\epsilon} \frac{\partial S_{w}^{\epsilon}}{\partial t} + \nabla \cdot (f_{w}^{\epsilon} \mathbf{u}^{\epsilon}) = 0, \tag{3-92}$$

where the superscript ϵ refers to fine-scale. The flow in the coarse scale (Darcy model) is described by the following equations:

$$\nabla \cdot (\mathbf{u}_{0}) = 0, \tag{3-93}$$

$$\nabla p_0 = \frac{\mathbf{u}_0}{K^{eq}_{1\phi 1k}(\lambda_T)^{eq}_{1\phi 1k}}, \tag{3-94}$$

$$\phi^{eq}_{1\phi 1k}\frac{\partial (S_w)_0}{\partial t} + \nabla \cdot ((f_w)^{eq}_{1\phi 1k}\mathbf{u}_0) = 0, \tag{3-95}$$

where the superscript (eq) represents the equivalent properties on the coarse scale and subscript 0 denotes the solution at the coarse scale. Hence, to accurately represent the fine scale at the coarse scale, it is essential to determine the equivalent values for $\phi^{eq}_{1\phi 1k}$, $K^{eq}_{1\phi 1k}$, $(k_{ro})^{eq}_{1\phi 1k}$, and $(k_{rw})^{eq}_{1\phi 1k}$. Through the application of averaging or integration within well-chosen REV the fine-scale might be well represented in the coarse scale.

The selection of $\phi^{eq}_{1\phi 1k}$ aims to represent the initial total oil and water volumes within Ω. $K^{eq}_{1\phi 1k}$ is derived from the results of Brinkman's single-phase, steady-state flow model. Using the average pressure and velocity field at the fine scale, $K^{eq}_{1\phi 1k}$ is computed to emulate the equivalent of Darcy's single-phase, steady-state flow model at the coarse scale. The selection of S_{wi} and S_{or} aligns with proportional quantities in the domain Ω. It is assumed that the relative permeability endpoint $(k_{ro})^{eq}_{1\phi 1k}$ at $(S_w)_0 = 0$ is equal one. The relative permeability curves are determined numerically. The following parameters are chosen for numerical optimization: $(k_{rw})^{eq}_{1\phi 1k}$ at $(S_w)_0 = 1$, $(n_w)^{eq}_{1\phi 1k}$, and $(n_o)^{eq}_{1\phi 1k}$. It is employed the History Matching (HM) [113] method as optimization procedure, where the equivalent relative permeability curve for the homogeneous $1\phi 1k$ Darcy model is determined. An iterative process is applied to compare water flow rates on Γ_2 and the Δp between Γ_1 and Γ_2 between the homogeneous $1\phi 1k$ Darcy and Brinkman models, aiming to optimize model parameters. More details about HM are given in section (3.4.3). It is necessary to use two objective functions in this context, one to determine the water flow rate in Γ_2, equ. (3-96) and the other to determine the pressure difference between Γ_1 and Γ_2, eq. (3-97). The root mean square error function (RSME), eq. (3-96) and eq. (3-97), are applied as the objective functions to minimize the difference between Brinkman and Darcy models, where Corey's water $((n_w)^{eq}_{1\phi 1k})$ and oil $((n_o)^{eq}_{1\phi 1k})$ exponents and the end-point $(k_{rw})^{eq}_{1\phi 1k}$ at $(S_w)_0 = 1$, are the design variables.

$$RSME_{Q_w} = \sqrt{\frac{1}{n}\sum_{i=1}^{n}\left((Q^B_w)_i - ((Q^{eq}_w)_i)_{1\phi 1k}\right)^2} \tag{3-96}$$

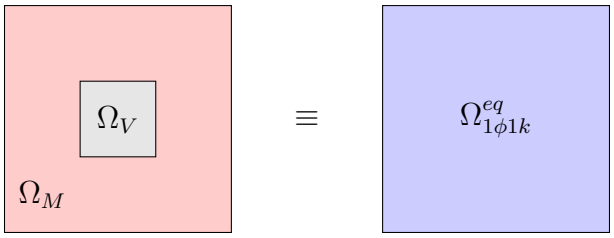

Figure 3.6: Schematic representation of the equivalent porous media ($\Omega^{eq}_{1\phi 1k}$), where the dimensions and the petrophysical properties (porosity, absolute permeability and relative permeability) are equivalent between Ω and $\Omega^{eq}_{1\phi 1k}$

.

$$RSME_{\Delta p} = \sqrt{\frac{1}{n}\sum_{i=1}^{n}\left((\Delta p_i)^B - (\Delta p_i)^{eq}_{1\phi 1k}\right)^2} \tag{3-97}$$

3.4.2.2 Equivalent Properties of the Dual-Continuum Model

The same principle is used as described in section (3.4.2.1), except that in the case here $\mathbf{u}_0$, p_0 and $(S_w)_0$ are the equivalent physical quantities for the homogeneous $2\phi 2k$ Darcy model. Figure 3.7 schematically illustrates how this homogenization is applied in a dual-continuum porous medium. The mathematical model for the coarse scale of the $2\phi 2k$ model is summarized as follows:

$$(\mathbf{u}_w)^m_0 = \frac{-(k_{rw}\mathbf{K})^m}{\mu_w}\nabla p^m_0, \tag{3-98}$$

$$(\mathbf{u}_o)^m_0 = \frac{-(k_{ro}\mathbf{K})^m}{\mu_o}\nabla p^m_0, \tag{3-99}$$

$$(\mathbf{u}_w)^f_0 = \frac{-(k_{rw}\mathbf{K})^f}{\mu_w}\nabla p^f_0, \tag{3-100}$$

$$(\mathbf{u}_o)^f_0 = \frac{-(k_{ro}\mathbf{K})^f}{\mu_o}\nabla p^f_0, \tag{3-101}$$

$$(\phi)^m \frac{\partial (S_w)_0^m}{\partial t} = -\nabla \cdot (f_w \mathbf{u}_0)^m - (q_w)^m , \tag{3-102}$$

$$(\phi)^m \frac{\partial (S_o)_0^m}{\partial t} = -\nabla \cdot (f_o \mathbf{u}_0)^m - (q_o)^m , \tag{3-103}$$

$$(\phi)^f \frac{\partial (S_w)_0^f}{\partial t} = -\nabla \cdot (f_w \mathbf{u}_0)^f - (q_w)^f , \tag{3-104}$$

$$(\phi)^f \frac{\partial (S_o)_0^f}{\partial t} = -\nabla \cdot (f_o \mathbf{u}_0)^f - (q_o)^f , \tag{3-105}$$

$$(q_w)^m = \frac{\alpha (k_{rw})^m}{\mu_w} \left(p^m - p^f\right), \tag{3-106}$$

$$(q_o)^m = \frac{\alpha (k_{ro})^m}{\mu_o} \left(p^m - p^f\right), \tag{3-107}$$

where the superscript m and f represents the matrix and fracture grids, respectively.

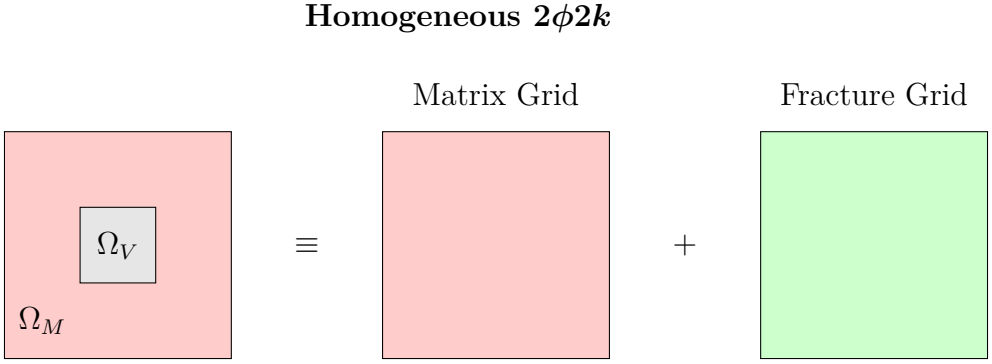

Figure 3.7: This diagram illustrates a homogeneous $2\phi 2k$ models. The light red color represents the matrix petrophysical properties, and the light green color represents the fracture grid petrophysical properties for the homogeneous $2\phi 2k$ Darcy model.

It is assumed that the porous matrix is well-defined. Thus, it is presumed that the porous grid in the $2\phi 2k$ model has the same petrophysical properties as

the porous matrix on the fine scale. Consequently, the equivalent petrophysical properties of the fracture grid on the coarse scale are established to represent properly the fluid flow obtained on the fine scale. The porosity of the fracture domain $(\phi)^f$ is set to a value that conserves the initial volume of fluid on fine-scale volume. The Brinkman single-phase steady-state model is used to calculate the equivalent absolute permeability of the $2\phi2k$ model. As the absolute permeability for the porous matrix grid is kept the same as on the fine scale, the fracture grid absolute permeability $(K)^f$ is established to represent the average results obtained by the Brinkman model on the fine scale. $(S_{wi})^f$ and $(S_{or})^f$ are assumed equal to zero. It is assumed that the relative permeability endpoint at $(k_{ro})^f$ at $(S_w)_0 = 0$ is equal to one. The relative permeability curves are determined using History Matching. The following parameters are chosen for numerical optimization: $(k_{rw})^f$ at $(S_w)_0 = 1$, and the six LET parameters (L_n, E_n, e T_n) for water and oil are varied. An iterative process is applied to compare water flow rates on Γ_2 between $2\phi2k$ and Brinkman models, aiming to optimize model parameters. The root mean square error function (RSME), denoted by eq. (3-96) and eq. (3-97), serves as the objective function to approximate the water flow rate obtained through the Brinkman model (Q_w^B) to that of the water flow rate derived from the homogeneous $2\phi2k$ model $((Q_w^{eq})_{2\phi2k})$. Additionally, it compares the pressure difference between $\Gamma1$ and Γ_2 in the Brinkman model $(\Delta p)^B)$ to that of the homogeneous $2\phi2k$ Darcy model $((\Delta p)_{2\phi2k}^{eq})$.

3.4.3
History Matching Procedure

Obtaining the equivalent homogeneous $1\phi1k$ and $2\phi2k$ Darcy models requires establishment of equivalent relative permeability curves. In this study, it is used the History Matching numerical procedure that minimized the differences between the fine and coarse scales water flow rate on Γ_2 and the pressure difference between Γ_1 and Γ_2. For this purpose, IMEX and CMOST software were used [113].

IMEX is a black oil reservoir simulator. It is part of CMG's reservoir simulation package, which includes both single and dual continuum models. In the $1\phi1k$ homogeneous model, the porous matrix is represented by a single-continuum or grid. The dual-continuum approach, on the other hand, involves two distinct continuums: one for the matrix and one for the fracture network. These models capture complex flow dynamics and interactions between matrix and fracture networks. The term "matrix grid" refers to the porous matrix, while the term "fracture grid" refers to the vugular portion of the domain.

The Black Oil model is widely used in reservoir engineering representation to predict hydrocarbon reservoir behavior. It is named as "black oil" because it primarily deals with oil reservoirs, including both oil and gas phases, while neglecting some of the more complex thermodynamic properties and phase behavior of fluids. Black Oil Model components include fluid phases (oil and gas), fluid properties (PVT properties), phase behavior (phase equilibrium, bubble point pressure, dew point pressure), material balance, and considerations for well-bore and surface facilities. Equations (3-108), (3-109) and (3-110) represent the black oil model for water, oil, and gas conservation:

$$\frac{\partial}{\partial t}\left(\frac{\phi\rho_w}{B_w}S_w\right) = -\nabla\cdot\left(\frac{\phi\rho_w}{B_w}\mathbf{u}_w\right) + q_w, \tag{3-108}$$

$$\frac{\partial}{\partial t}\left(\frac{\phi\rho_o}{B_o}S_o\right) = -\nabla\cdot\left(\frac{\phi\rho_o}{B_o}\mathbf{u}_o\right) + q_o, \tag{3-109}$$

$$\frac{\partial}{\partial t}\left[\phi\left(\frac{\rho_g}{B_g}S_g + \frac{R_s\rho_g}{B_o}S_o\right)\right] = -\nabla\cdot\left(\frac{\rho_g}{B_g}\mathbf{u}_g + \frac{R_s\rho_g}{B_o}\mathbf{u}_o\right) + q_g. \tag{3-110}$$

Consequently, in order to maintain coherence with the Brinkman equation, the black oil model needs to be simplified. It is assumed oil formation volume (B_o) and water formation volume (B_w) are considered constants and equal to one, the fluids and rocks compressibility are set $10^{-10}\ \ 1/kPa$, and the gas, oil and water densities are constant and equal to 1 kg/m^3. Equation (3-110) is beyond the scope of this study because there is no gas flow within the porous medium.

History Matching is a common practice in reservoir engineering. History Matching is defined as the method of examining and making adjustments to model parameters based on past production data. This procedure typically involves numerical methods through which the petrophysical properties of the reservoir model are altered to ensure accurate production data representation.

CMOST History Matching workflow is described as follows. The first step is to provide a reference solution to the IMEX model. In the cases studied here, it is used the Brinkman fine scale solution regarding the water flow rate along Γ_2 and the Δp between Γ_1 and Γ_2. CMOST takes the reference solution as well as the black oil model as a starting point, modifying user-parameterized properties through probability distribution functions. The adjustments are made after evaluating the quality of each simulation run of the IMEX program.

By using an optimization algorithm, the parameter space is explored in an effort to minimize the objective function calculated from the initial simulations of the experimental design. As the number of simulations increases, the results converge closer to that of the reference solution, resulting in a satisfactory solution.

The Designed Exploration and Controlled Evolution (DECE) optimization algorithm is selected. As part of the CMOST DECE optimizer [113], CMG has developed its own proprietary optimization method. As a result, only limited detail is provided regarding the methods and the mathematical description of the methods used. The DECE optimization process consists of two phases: an exploration phase followed by an evolution phase. The purpose of the designed exploration phase is to systematically explore the search space in a random but carefully planned manner in order to gain a comprehensive understanding of the solution space. To generate representative simulation datasets, a combination of experimental design principles and search techniques is applied. During the controlled evolution phase, the simulation results from the designed exploration phase are statistically evaluated. As part of the DECE algorithm, each possible parameter value is meticulously analyzed, assessing whether rejecting certain values would enhance the quality of the solution. As a result of these rejections, the algorithm stores them and excludes them from further exploration. A periodic review of these excluded values is conducted by the DECE algorithm in order to mitigate the risk of getting trapped in local minimum. In the event that the algorithm concludes that some of these exclusions are no longer justified, they are revoked, and the candidate values associated with these exclusions are reintroduced for consideration.

In this study, Latin Hypercube design experiments are employed to establish a sampling space, accessible within the Cmost software package [113]. The Latin Hypercube method is a statistical approach designed to sample multivariate distributions efficiently. It categorizes input variables into k strata, ensuring that each combination within a stratum is sampled precisely once. This technique ensures comprehensive and uniform coverage of parameter spaces, minimizes variance in estimations, and accommodates any number of variables. The number of sample values for each parameter can vary without limit. Users can input these values to be uniformly distributed (uniform distribution) or non-uniformly distributed (non-uniform distribution). Sampling without replacement is employed to amalgamate sample values into design points. For instance, for the first point, one value from each parameter set is randomly selected. Subsequent selections exclude previously chosen points. Latin hypercube sampling enhances the random design by considering input variables as

random variables with known distribution functions. Each input variable's distribution is divided into n strata of equal probability, with one sample taken from each stratum. These sampled input values are then randomly assigned across n cases.

In this study it is used the Gilman and Kazemi (1983) [66] shape factor σ (eq.(2-3)) for the $2\phi 2k$ model. σ is given by the following expression:

$$\sigma = 4\left[\frac{1}{L_x^2} + \frac{1}{L_y^2} + \frac{1}{L_z^2}\right] \tag{3-111}$$

where L_x, L_y, and L_z are the length of matrix edges.

3.5 Mesh Generation

The study involves the generation of both structured and unstructured meshes according to the geometry of the vug. Three families of vug geometry are considered in this context. Firstly, synthetic vugs are simple structures composed of rectangles. The second set of geometries are derived from the Arapuá outcrop, which contains more complex structures. Further, a micro tomography rock sample is used to demonstrate the methodology on a plug scale. A detailed description of the methodology behind mesh generation is provided below.

3.5.1 Structured Mesh Generation

Synthetic vug configurations consisted of simple geometries, with regular and rectangular vugs within the porous matrix. The Donfin library is part of the FEniCS Project and offers a user-friendly mesh generation method called UnitSquareMesh(). This method generates structured square two-dimensional triangular meshes. The length of each dimension of the synthetic flow domain is one meter. The UnitSquareMesh() method requires specific input parameters to determine the number of cells in each direction. As a result, rectangles are subdivided into triangles. Figure 3.8 schematically illustrates how this method generate different mesh configurations. In all the scenarios, it is used the "crossed" option to divide each square element of the domain in order to generate isotropic meshes. The selection of the number of elements considers two criteria. Firstly, the vugs are discretized to capture flow nuances minimally. Second, the solution is mesh independent.

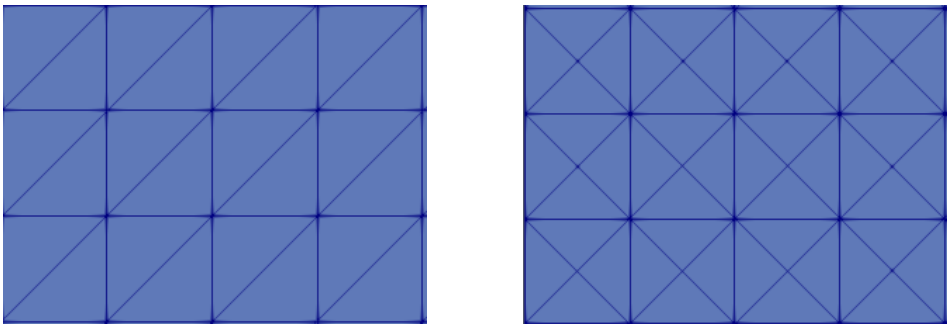

(a) UnitSquareMesh(4,3, "right")

(b) UnitSquareMesh(4,3, "crossed")

Figure 3.8: Example of two meshes configuration generate through the Dolfin library.

3.5.2 Unstructured Mesh Generation

The meshes constructed for Lajedo Arapuá and the vug configuration based on the micro tomography image of the carbonate plug are more sophisticated than the ones used on the synthetic vug configuration, necessitating an alternative methodology. The micro tomography image is used to study two-phase flow through a vuggy porous medium. The geometry represents a cross-section of a carbonate rock core obtained by a micro-tomography scan. The core was extracted from the Morro do Chaves Formation, located in the Sergipe-Alagoas Basin, in Brazil. The micro-tomography image is processed to make it binary, with black pixels representing the vugs and gray pixels representing the porous matrix. More details about the image processing can be found on [40]. For the Lajedo Arapuá vug configurations, it is adopted the approach developed by Dali (2019) [40] and Campos (2022) [60] which is summarized in the following discussion. Based on the 3D geological model, 2D black-and-white images are produced according to individual geological layers where the color black is associated with the vug and the white is associated with the porous matrix. A complete description of the Lajedo Arapuá is provided on section (5.1). Through the script developed by Dali (2019) [40], the binary black-and-white images are interpreted. At the interface between the black and white colors, there is a surface that separates the matrix from the vug. This surface is interpreted as a point cloud and these points delineate the interfaces between the porous matrix and the vugs regions. Subsequently, based on this data set, the finite element mesh is generated using the Gmsh software [112].

3.6 Numerical Validation

This section provides the validation of the implementation of the models presented in this chapter. The accuracy of the numerical results is evaluated by comparing them with existing literature simple cases. The Brinkman single-phase steady state model is numerically verified using a semi-empirical equation developed by Yao and Huang (2017) [15]. Moreover, Brinkman formulation is verified on its limit cases, where there is only porous matrix or the free-flow region. The free-flow region scenario is validated by the flow between two infinite parallel plates at low Reynolds numbers where a pressure gradient is imposed between them. Considering the two-phase flow in porous media the Buckley-Leverett analytical solution is used to evaluate the models. To the best of author's knowledge the are no analytical solution for the Brinkamn equation. In spite of this, the model proposed in this study is compared to the model developed by Hallack, which despite being based on a differential set of differential equations, has a similarities with the model used here, therefore making it possible to conduct a qualitative comparison between them.

3.6.1 Darcy Two-phase

The validation for the Darcy two-phase flow is presented for the weak form of the Darcy model (section 3.3.1) as well as the Brinkman model section (3.3.2) when the Brinkman viscosity set to zero ($\mu^* = 0$), which recovers Darcy formulation. Thus, assuming $\mu^* = 0$ there are two Darcy models and both need validation because each is formulated differently. Brinkman's model employs the BDM_1 basis functions, whereas Darcy's model employs the RT_0 basis functions. As both cases are Darcy models, Buckley-Leverett analytical equation is used to verify them.

The numerical domain used for numerical validation is similar to figure 3.3, where Ω consists of a 1×1 m^2 square characterized by uniform petrophysical properties described in table 3.1. A constant water injection rate is enforced at Γ_1 while maintaining constant pressure at Γ_2. For this analysis, a mesh is generated using the Donfin library. It consists of 500 vertices in the x-direction (the flow direction) and 20 vertices in the y-direction (perpendicular to flow direction). This design emphasizes refinement along the x-direction to accurately capture the abrupt alteration in water saturation as the water front progresses.

Figures 3.9 and 3.10 present the position of the water front as function of

Parameter	Value
ϕ	0.2
K	100 mD
Relative Permeability Model	Corey
n_w	2
n_o	2
S_{wi}	0
S_{or}	0
k_{ro} at $S_w = 0$	1
k_{rw} at $S_w = 1$	1
μ_o	1 cp
μ_w	1 cp
$\mathbf{u}$ on Γ_1	10^{-6} m/s
p on Γ_2	1 atm
S_w on Γ_1	1

Table 3.1: Porous matrix parameters for the numeric validation used in the Brinkman and Darcy models.

t_D both the Buckley-Leverett analytical solution and numerical solutions for the Darcy model and Brinkman model ($\mu^* = 0$), respectively. It is considered three distinct viscosity ratios between water and oil ($\mu_o/\mu_w = 0.5$, 1.0, and 2) across three different injected pore volumes ($t_D = 0.3$, 0.5, and 0.7). In all the scenarios examined, both methods demonstrate substantial agreement between the numerical and analytical results. This alignment suggests that the numerical models effectively capture the underlying physical phenomena.

3.6.2 Stokes Limit Case

Stokes model is a limit case of the Brinkman model. It typically occurs in cases where there is no pores matrix region, only the free-flow region. Mathematically, it occurs when the permeability approaches extreme high values ($K \to \infty$) and the porosity is equal to one. Figure 3.11 is a sketch of the configuration chosen to solve the Stokes equation analytically. The two plates remain stationary while a pressure gradient is applied to induce flow between them. It is assumed that non-slip boundary conditions apply to the plates. The analytical solution is given as:

$$u_p = \frac{h^2}{2\mu}\frac{\partial p}{\partial x}\left(\left(\frac{y}{h}\right)^2 - \frac{1}{4}\right) \tag{3-112}$$

In this example, the conditions are defined as follows: $\partial p/\partial x = -10\ Pa/m$, $h = 1m$, and $\mu = 1\ Pa \cdot m$.

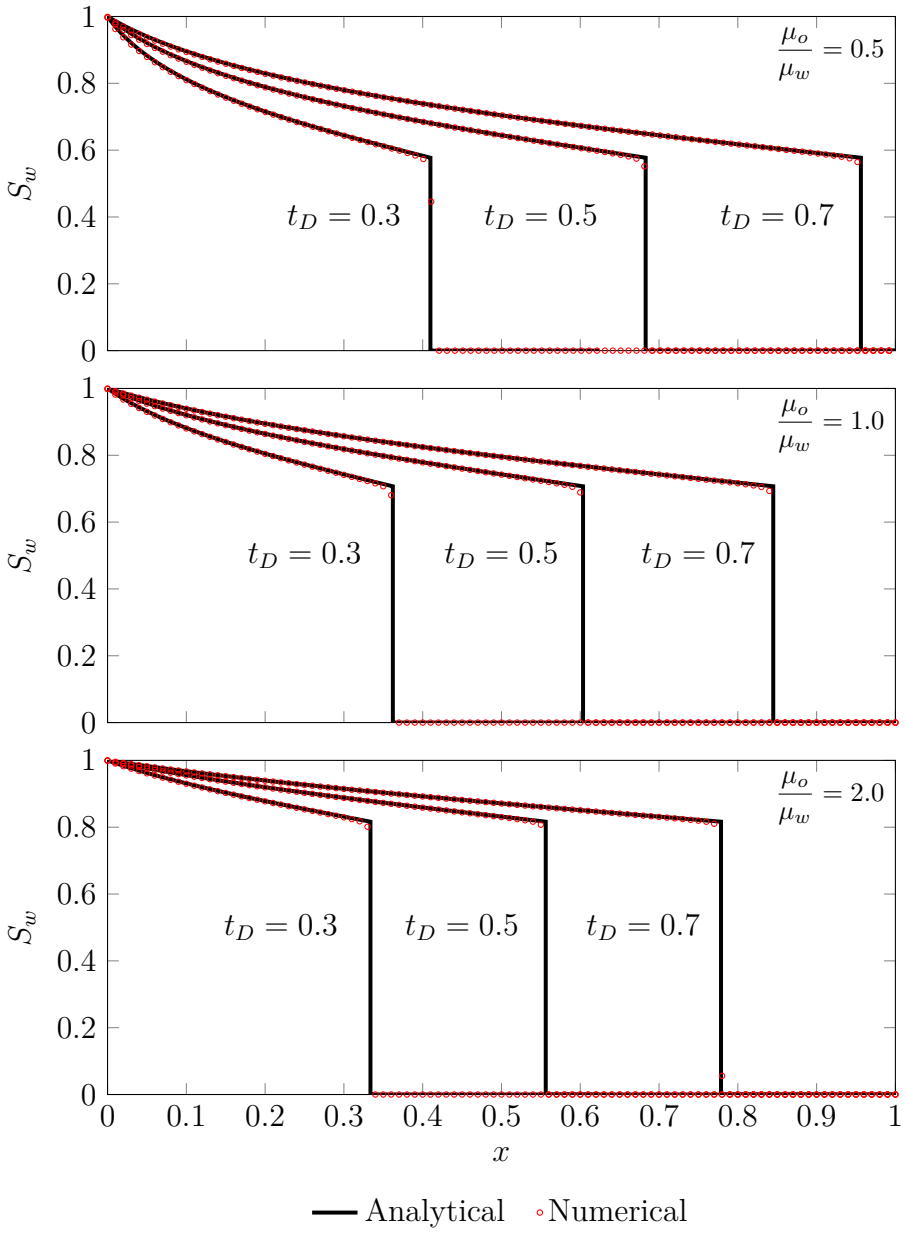

Figure 3.9: Brinkman model two-phase flow numerical solution is compared with the analytical Buckley-Leverett solution for the injection of three distinct porous volumes (t_D = 0.3, 0.5, and 0.7) across three different viscosity ratios ($\frac{\mu_o}{\mu_w}$ = 0.5, 1.0, and 2.0). In this case, the Brinkman model has the $\mu^* = 0$.

Figure 3.12 presents a comparative analysis between the numerical results derived from equation (3-89) and the analytical results from (3-112). Notably, there is strong agreement between numerical and analytical outcomes where the mean square root error is 8.61×10^{-6} m/s.

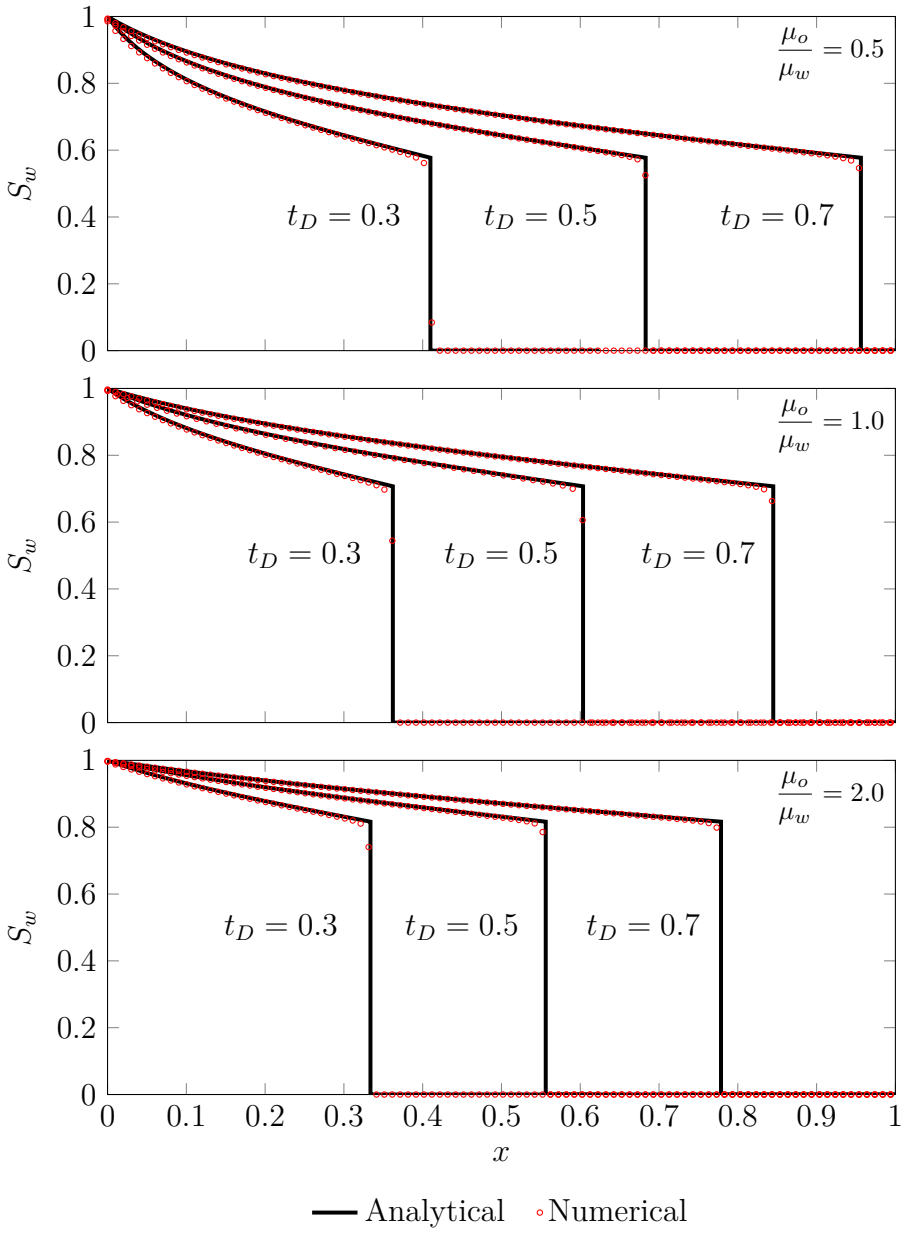

Figure 3.10: Darcy two-phase flow model numerical solution is compared with the analytical Buckley-Leverett solution for the injection of three distinct porous volumes (t_D = 0.3, 0.5, and 0.7) across three different viscosity ratios ($\frac{\mu_o}{\mu_w}$ = 0.5, 1.0, and 2.0).

3.6.3 Brinkman Equation

A study conducted by Yao and Huang (2014) [15] established a semi-empirical correlation for the velocity profile within a channel and a porous matrix. This research employed a similar set up used by Beavers and Joseph (1967) [25] to investigate flow interactions between the porous medium and a free-flow channel. This experiment aimed to evaluate the influence of porous

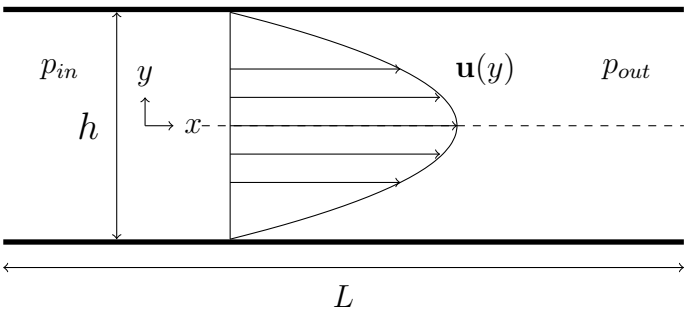

Figure 3.11: Velocity distribution between two stationary parallel plates under an imposed pressure gradient.

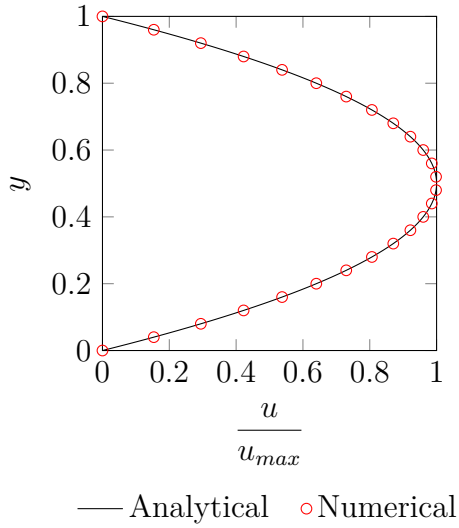

Figure 3.12: The velocity field of creep flow between two parallel plates, modeled by the equation (3-89), is compared against the analytical solution provided by the Stokes equation (3-112).

media on fluid velocity in free-flow regions. Figure 3.13 offers a schematic representation of this experimental configuration, wherein a constant differential pressure is maintained across the observation window. They used Laser Doppler Anemometry (LDA) to measure the velocity profile in the free-flow region. As result, they proposed the equation (3-113) for the velocity profile in this region. Therefore, this correlation is used to validate the velocity field in the single-phase steady state Brinkman model.

In the experiment, the channel is partially filled with a porous media, with ϕ equal to 0.45 and K equal to 5 $\times 10^{-5} m^2$ and the $\partial p/\partial x = -0.33\ Pa/m$. The free-flow region ($h$) has the dimension of 20 mm. Figure 3.14 presents the semi-analytical and the numerical results. It is noted a good correlation resulting in a RSME of 8.8 10^{-5} m/s between the analytic and numerical solutions.

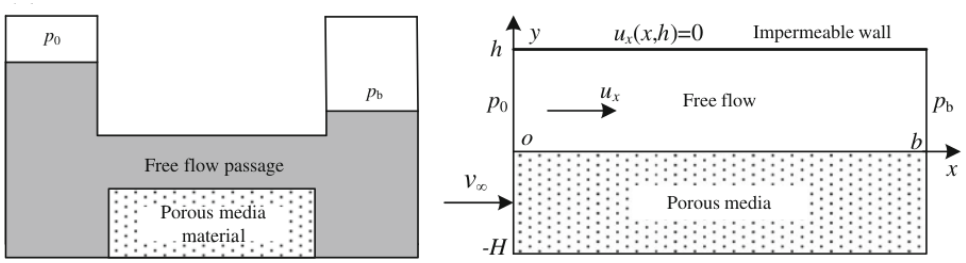

Figure 3.13: Schematic configuration of the experimental apparatus used by [15].

$$\begin{cases} u_s = \left(1 + \dfrac{\alpha}{\sqrt{K}} y\right) u_B + \dfrac{1}{2\mu}\left(y^2 + 2\beta\alpha\sqrt{K}y\right)\dfrac{\mathrm{d}p}{\mathrm{d}x} \\ u_B = -\dfrac{K}{2\mu}\left(\dfrac{\alpha^2 + 2\beta\alpha\sigma}{1+\alpha\sigma}\dfrac{\mathrm{d}p}{\mathrm{d}x}\right) \\ \sigma = \dfrac{H}{\sqrt{K}} \end{cases} \tag{3-113}$$

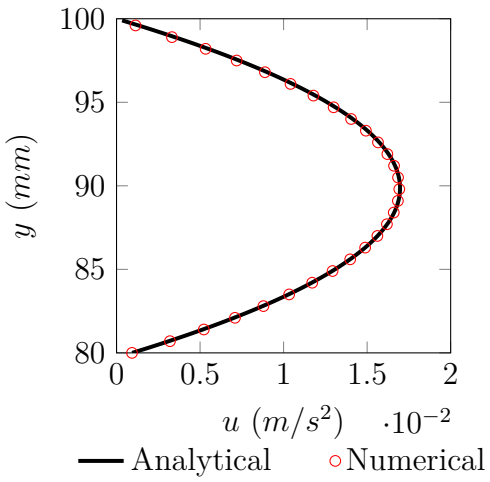

Figure 3.14: The single-phase steady state velocity field obtained by Brinkman numerical solution is compared with the semi-analytical model proposed the Yao and Huang (2017) [15], eq. (3-113).

3.6.4 Brinkman Two-Phase Equation

Despite the authors' best efforts, it was not possible to find an analytical solution to a two-phase flow using the Brinkman equation, even for a simple case. Hence, it was decided to compare the numerical model with a numerical case from the literature. The two models are not exactly the same and this can cause some differences, as shown in figure 3.15. The results of this study

is compared with those presented by Hallak et al. (2019) [45]. In his model, Hallack considered a compressible porous medium with varying compressibility between the vugular and porous regions of the medium, where the vugular compressibility was ten times greater than the matrix compressibility. Furthermore, the author split the Brinkman equation and the conservation equations for the water and oil phases. By adding the conservation of mass, a system of five differential equations was generated. Therefore, Hallack's model differs slightly from the approach proposed in this study, leading to discrepancies.

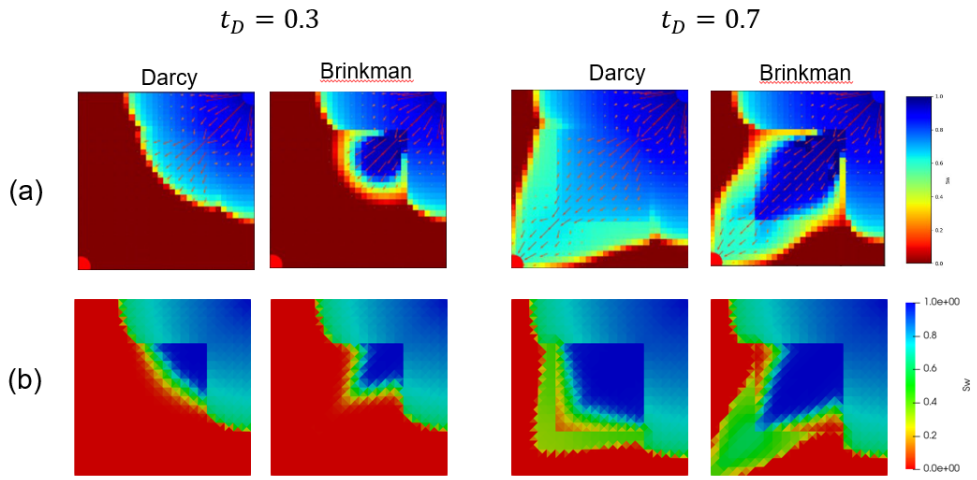

Figure 3.15: The saturation map for two different porous volumes is compared between (a) Hallack's model [45] and (b) this study's model. Brinkman and Darcy models are presented in both studies..

Figure 3.15 illustrates the water front advancement for two distinct t_D values for both models under consideration. As can be seen, the saturation fields for $t_D = 0.3$ differ slightly for the Brinkman and Darcy models between the two studies. The disparities become more pronounced at $t_D = 0.7$, wherein the most significant variations are observed when considering the Darcy model scenarios. As the two investigations use different mathematical modeling approaches, these variations can be attributed to the fact that Hallack's models include compressibility effects, which were not considered in this study. One of the noteworthy aspects of Darcy's model is that there is a more pronounced difference in saturation field in the vugular region. Hallack did not specify which relative permeability curve was used in the vugular region. This study uses a $\times$ curve. A closer examination at $t_D = 0.7$ reveals that disparities exist between the two investigations. For the Brinkman model, these differences are minor and can be attributed to differences in the modeling of compressibility between the two studies. In spite of the differences between the two studies, a qualitative comparison between them is still feasible, as they both demonstrate

a similar trend. In both studies, channeling is evident within the vugs in the Brinkman model, a phenomenon that is not represented by the Darcy model.

4
Comparison Between Prediction of Brinkman and Single-Continuum Models

4.1
Synthetic Domain

Five distinct sintetic vuggy configurations, as illustrated in Figure 4.1, are considered in this study. The flow domain is a $1 \times 1\ m^2$ square porous media containing embedded vugs. These configurations share the same macroporosity but differ in size, shape, and position within the porous matrix. Macroporosity is defined as the ratio of the vug domain's volume to the entire domain's volume, denoted as $\phi^{\epsilon}_{Vug} = V^{\epsilon}_{\Omega_V}/V^{\epsilon}_{\Omega}$. For all of them, ϕ^{ϵ}_{Vug} are equal. The petrophisical and fluid properties are presented in Table 4.1. Initially, the entire domain Ω is saturated with oil ($S_w = 0$). The layout of the boundary conditions is the same as in the figure 3.3. Water is injected at a constant velocity of $\mathbf{u}_{in} = [10^{-6}, 0.0]$ m/s and $S_w = 1$ on Γ_1. Moreover, the outlet pressure on Γ_2 is kept constant along $p_{out} = 1$ atm.

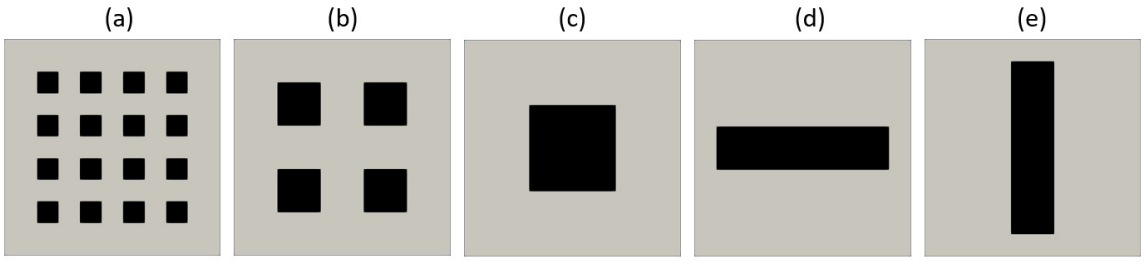

Figure 4.1: The five different domains (vug configuration (a)-(e)) where the geometry and position of Ω_V (black) is varied on the domain and in Ω_M (gray).

4.2
Micro Tomography Image Domain

A more realistic vug configuration, presented in figure 4.2, is used to study two-phase flow through a vuggy porous medium. The geometry represents a cross-section of a carbonate rock core obtained by a micro-tomography scan.

Parameter	Value
ϕ_M^ϵ	0.2
ϕ_{Vug}^ϵ	0.16
K_{ii}^ϵ	100 mD
Relative Permeability Model	Corey
n_w^ϵ	2
n_o^ϵ	2
S_{wi}^ϵ	0
S_{or}^ϵ	0
(k_{ro}^ϵ) at $(S_w)_0$	1
(k_{rw}^ϵ) at $(S_w)_1$	1
μ_o	1 cp
μ_w	1 cp
$\mathbf{u}$ on Γ_1	10^{-6} m/s
p on Γ_2	1 atm
S_w on Γ_1	1

Table 4.1: Porous matrix and fluid parameters for the synthetic cases, (a)-(e) in the Brinkman fine scale model.

The core was extracted from the Morro do Chaves Formation, located in the Sergipe-Alagoas Basin, in Brazil. The micro-tomography image is processed to make it binary, with black pixels representing the vugs and gray pixels representing the porous matrix. As for the petrophysical properties, all are the same as those in Table 4.1, except that $\phi_{Vug}^\epsilon = 0.135$. The image was taken from Dali (2019) [40]. Her study provides a comprehensive description of the process of acquiring an image. Additionally, grayscale images are converted into point clouds using a MATLAB algorithm. Data from this point cloud is used by the Gmsh software to create the unstructured meshes that are used in numerical simulations. Dali's work comprehensively examines the entire process of creating images from microtomography, treating and processing them, creating meshes.

4.3 Mesh Test

The meshes are selected to achieve an optimal representation of flow dynamics while ensuring computational efficiency. This analysis is conducted to identify suitable meshes for two-phase flow solutions. Furthermore, mesh selection considers the consistency of meshes between the cases utilizing models generated on the FEniCS platform and those generated using the IMEX software. The consistency of meshes across the two solvers is performed as follows. In both scenarios, mesh refinement is evaluated to improve the numerical solution based on available computing resources. FEniCS models are limited by

Figure 4.2: Micro tomography image domain, where Ω_V (black) is the vug and Ω_M (gray) is the porous matrix. In this case $\phi^{\epsilon}_{Vug} = 0.135$.

the fact that they are run on a laptop with a simple configuration (Intel Core i5-1035G1 CPU 1.00GHz × 8; Memory 8 GB RAM) , whereas IMEX software has access to the Petrobras Cluster. Therefore, FeniCS mesh selection is performed first. IMEX meshes are comparable in size to FEniCS meshes. Additionally, IMEX mesh refinement is examined to determine whether improved results can be obtained. Despite this, mesh refinement is not beneficial in any of the cases evaluated. The process of coarsening meshes, also known as upgridding, is not considered. This approach is intentionally omitted in this study. Since two-phase flow can be significantly affected by scale transformation when meshes are coarse, this aspect of the study has been excluded.

Initially, the influence of the mesh is examined by comparing the numerical solution of the homogeneous $1\phi 1k$ Darcy model with the analytical solution of the Buckley-Leverett model (equation (3-35)). For this analysis, a porous medium similar to Figure 3.3 is selected, containing only the porous matrix. The petrophysical properties are described on table 4.1. The porous medium is fully saturated with oil. Water is injected at a constant flow rate of $10^{-6}\ m^3/s$ at Γ_1 while a constant pressure of 1 atm is maintained at Γ_2. This configuration produces an isotropic and homogeneous porous medium, which may be compared to the analytical Buckley-Leverett model.

Table (4.2) displays five distinct mesh configurations examined. In these configurations, mesh refinement is performed along the horizontal axis, since vertical flow is negligible. Figure 4.3 illustrates water saturation as a function of horizontal position for $t_D = 0.5$. As the mesh is refined, the numerical solution adheres better to the analytical solution. The region with the abrupt saturation change, where the water front is located, benefits most from mesh refinement. It is observed that for solutions for Mesh III, there is substantial correspondence

between the numerical results and the Buckley-Leverett analytical solution. This test, however, is not sufficient to decide which mesh to use in the cases with vugs. Thus, each synthetic domains has to be tested to verify the meshes' consistency.

Mesh	Nx	Ny	Elements	RMSE
Mesh I	20	20	1,600	3.44×10^{-2}
Mesh II	40	20	3,200	2.17×10^{-2}
Mesh III	100	20	8,000	1.03×10^{-2}
Mesh IV	250	20	20,000	7.29×10^{-3}
Mesh V	500	20	40,000	6.50×10^{-3}

Table 4.2: Mesh parameters used for the mesh test in the synthetic vug configuration (a)-(e). Nx and Ny are the parameters used in the UnitSquareMesh(Nx, Ny, "crossed") method.

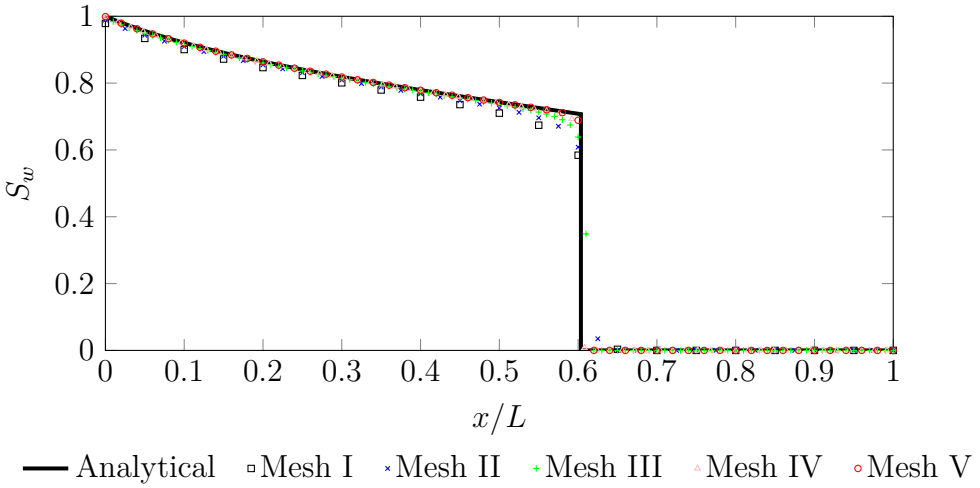

Figure 4.3: The influence of the mesh size on two-phase flow. As the mesh is refined, the discontinuity region at the front is better represented

Supporting the previous analysis, mesh tests are conducted for the five synthetic vug configurations. Table (4.3) displays five distinct mesh configurations tested. The presence of vugs alters fluid dynamics, making the vertical velocity component significant. Therefore, it is decided to keep the same number of elements in x and y directions.

For the micro tomography sample, the mesh test takes other parameters in consideration. The mesh generation parameters include the target mesh size for boundaries (cl_1), the target mesh size for the porous matrix-vug interface (cl_2), and the maximum characteristic length (cl_{max}). Table (4.4) presents the mesh parameters used in this analysis.

		Computational Time (s)				
Mesh	N^o. Elem.	(a)	(b)	(c)	(d)	(e)
Mesh 1	1,600	3.1×10^2	3.2×10^2	3.3×10^2	6.8×10^2 [1]	3.6×10^2
Mesh 2	6,400	2.5×10^3	2.5×10^3	2.6×10^3	6.3×10^3 [1]	2.9×10^3
Mesh 3	25,600	2.1×10^4	2.1×10^4	2.1×10^4	4.9×10^4 [1]	2.0×10^4
Mesh 4	40,000	4.7×10^4	4.8×10^4	4.8×10^4	8.5×10^4 [1]	4.7×10^4
Mesh 5	57,600	8.9×10^4	9.0×10^4	1.2×10^5 [2]	2.1×10^5 [1]	8.1×10^4

Table 4.3: Mesh parameters used for the mesh test in the synthetic vug configuration (a)-(e). It is also presented the computational time for each case. The time step used in these experiments is 200 s. [1]$\Delta t = 100$s. [2]$\Delta t = 150$s

Mesh	cl_1 (m)	cl_2 (m)	cl_{max}(m)	N^o. Elem.	Comput. Time (s)
Mesh 1	8.0×10^{-4}	8.0×10^{-4}	8.0×10^{-4}	3,944	4.3×10^3
Mesh 2	5.0×10^{-4}	5.0×10^{-4}	5.0×10^{-4}	8,944	1.5×10^4
Mesh 3	2.5×10^{-4}	2.5×10^{-4}	2.5×10^{-4}	32.518	1.2×10^5
Mesh 4	2.0×10^{-4}	2.0×10^{-4}	2.0×10^{-4}	50,002	2.7×10^5

Table 4.4: Mesh parameters used for the mesh test in micro tomography configuration. It is also presented the computational time for each case. The time step used in these experiments is 2 s.

Figure 4.4 illustrates the variation of W_{cut} as a function of t_D for all vug configurations. Water cut (W_{cut}) is defined as the ratio between the water flow and total flow rate along the outflow boundary Γ_2. For the cases (a)-(e) the W_{cut} exhibits minimal variance between Mesh 4 and Mesh 5. Essentially, employing more refined meshes than Mesh 4 did not yield an improved solution. Additionally, as depicted in figure 4.3, Mesh III provides a satisfactory resolution when compared with the analytical solution. It is noted that the simulation time increases significantly from Mesh 4 to Mesh 5 which is not desired. Consequently, for the cases examined here, it is considered appropriate to employ Mesh 4 for the synthetic vug scenarios. Mesh 4 has 40,000 elements for the four vug scenarios. This mesh configuration leads to the Brinkman model and the Darcy model have 200,400 and 140,200 degrees of freedom, respectively.

Mesh of 4 is selected for the micro tomography sample since more refined meshes do not improve the water cut evolution. The resulting mesh has 32,518 elements and the Brinkman and Darcy model has 163,022 and 114,029 degrees of freedom, respectively. Figures 4.5, 4.6, 4.7, 4.8, 4.9, and 4.10 illustrate the mesh for the five synthetic vug configurations (a)-(e) and

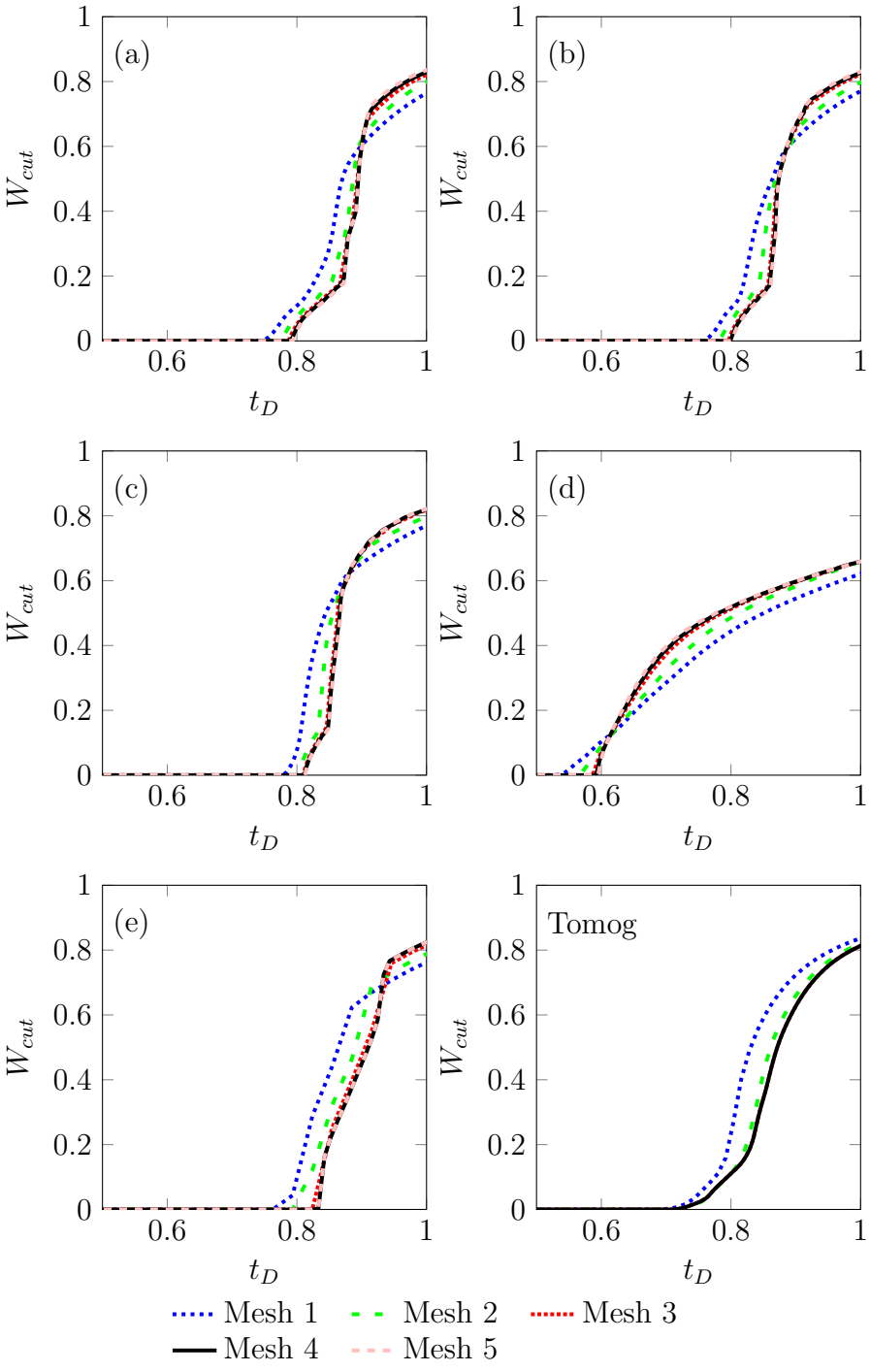

Figure 4.4: Analyses of mesh impact on synthetic vug configuration (a)-(e) and the micro tomography. It is presented the influence of mesh refinement on W_{cut} as a function of t_D.

the micro tomography sample, respectively.

The homogeneous $1\phi 1k$ model has the objective of the establishment of an equivalent porous media through equivalent porosity, equivalent absolute permeability and equivalent relative permeability curves. Specifically, equivalent relative permeability curves are obtained through numerical optimization.

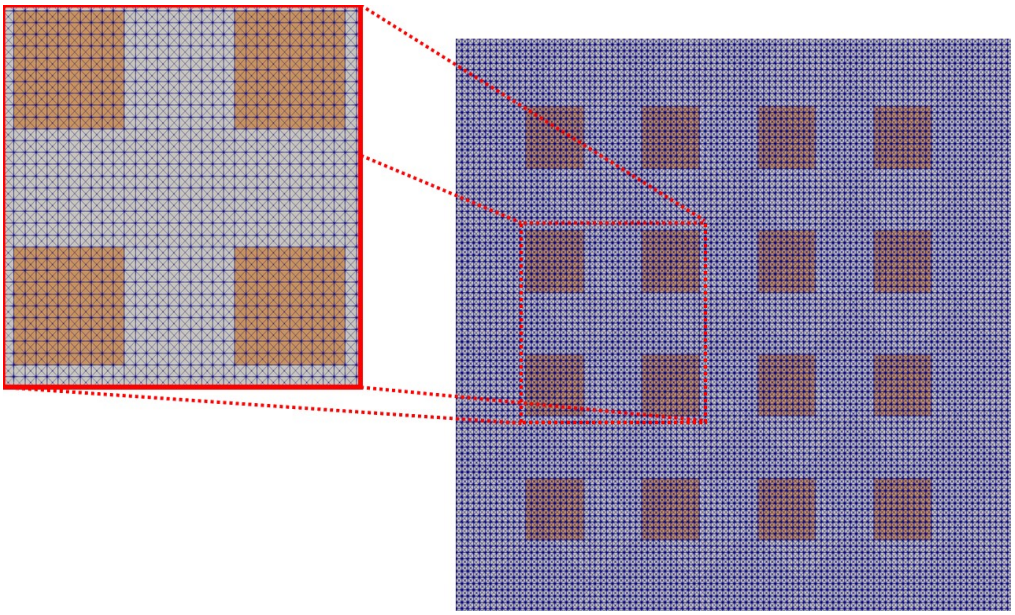

Figure 4.5: Mesh of the synthetic vug configuration (a).

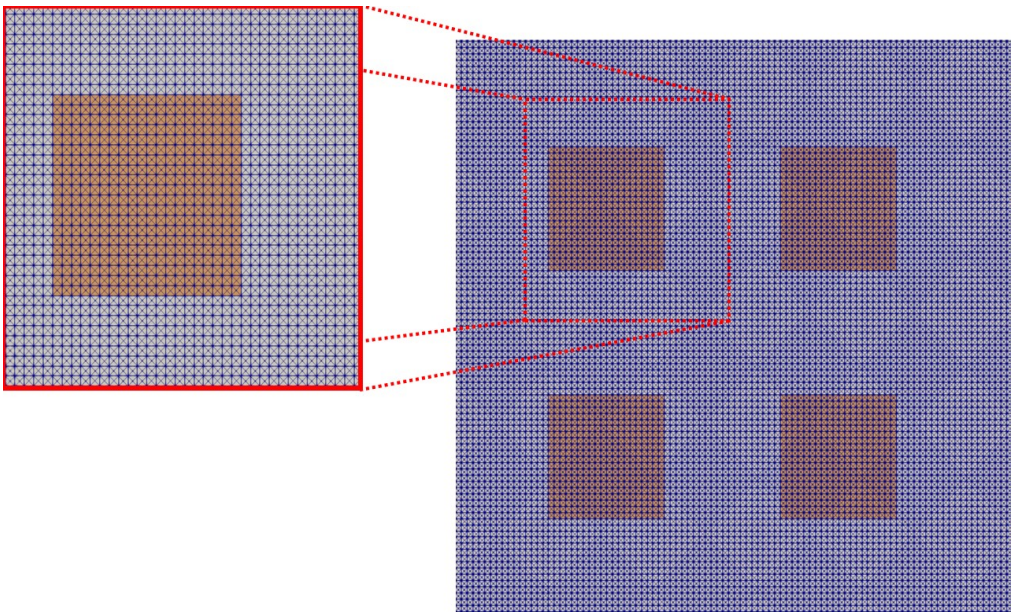

Figure 4.6: Mesh of the synthetic vug configuration (b).

For this task IMEX and CMOST are chosen. It is imperative that the meshes employed in the Brinkman model align with those utilized by IMEX to prevent undesired effects, such as scale-related effects due the the mesh on two-phase flow. To achieve this compatibility, the same number of elements is employed for both meshes. The only difference lies in the shape of these elements, as IMEX utilizes rectangular structured meshes, while the Donfin library generates triangular structured meshes. The IMEX program generates these meshes based on parameters defining the number of cells in each direction as well as

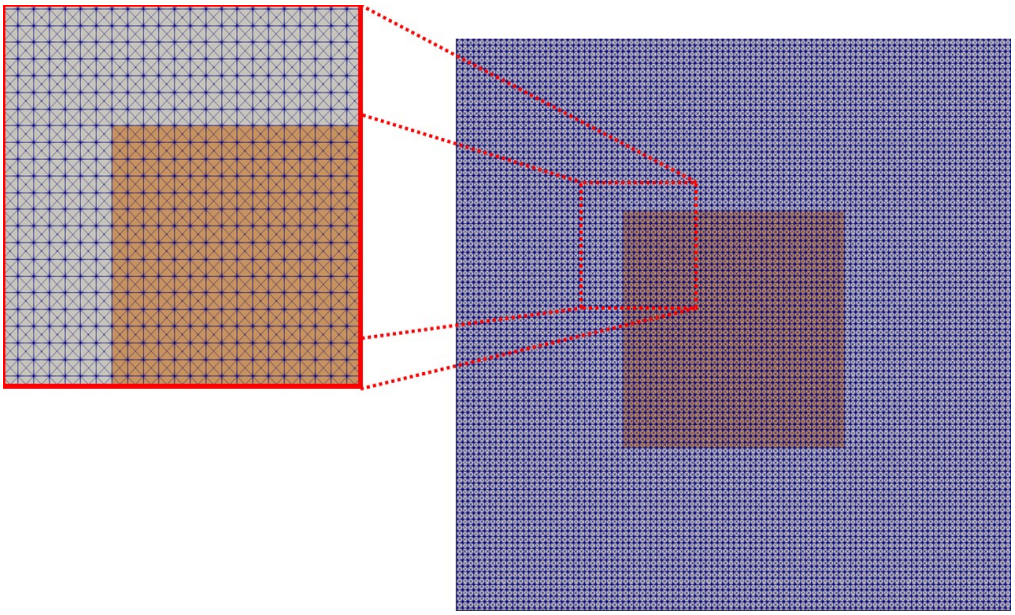

Figure 4.7: Mesh of the synthetic vug configuration (c).

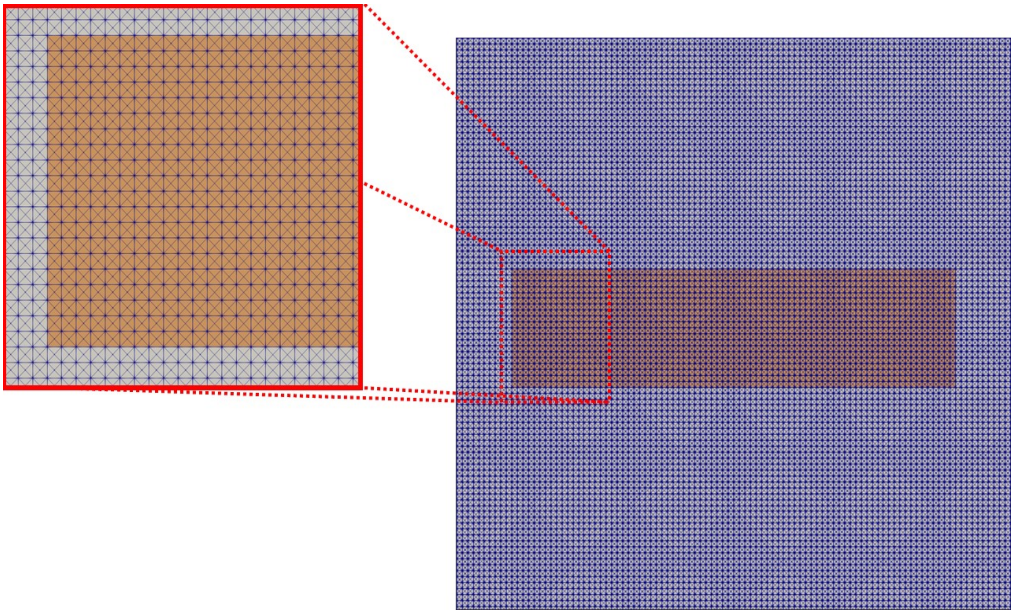

Figure 4.8: Mesh of the synthetic vug configuration (d).

the size of the edges. In the synthetic vugs, the mesh is generated with Nx = 200, Ny = 200, and Nz = 1, with each edge measuring 0.005 m. Figure 4.11 presents the IMEX mesh used to establish the equivalent $1\phi 1k$ domain

IMEX models use different boundary conditions when compared to those employed in the Brinkman and Darcy models developed with the FEM using the Dolfin library. IMEX directly imposes impermeable conditions on all boundaries, with mass exchange occurring through well-surface coupling. In essence, to emulate the inlet condition at Γ_1 and the outlet condition at Γ_2, a

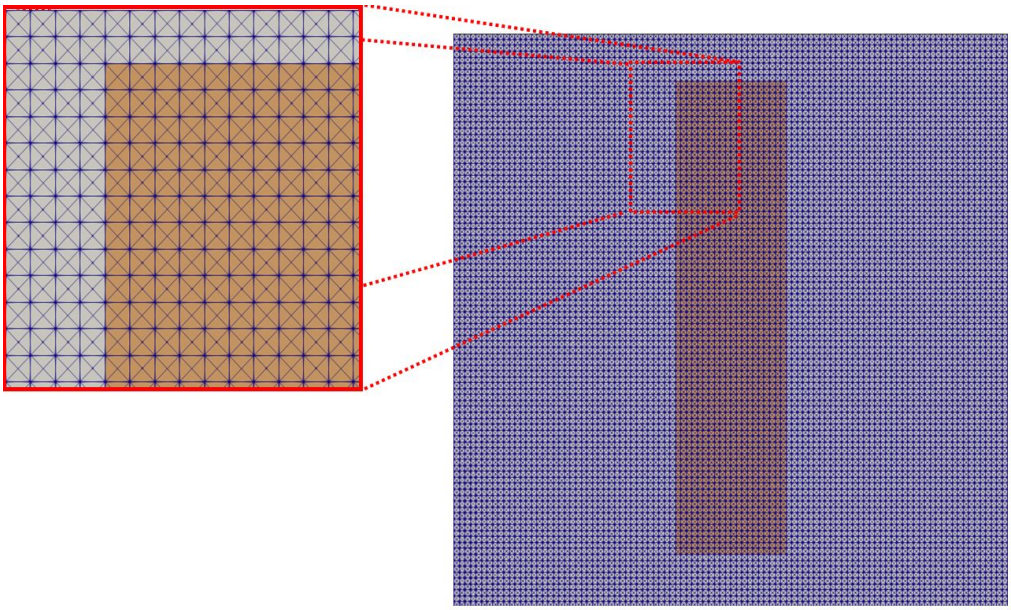

Figure 4.9: Mesh of the synthetic vug configuration (e).

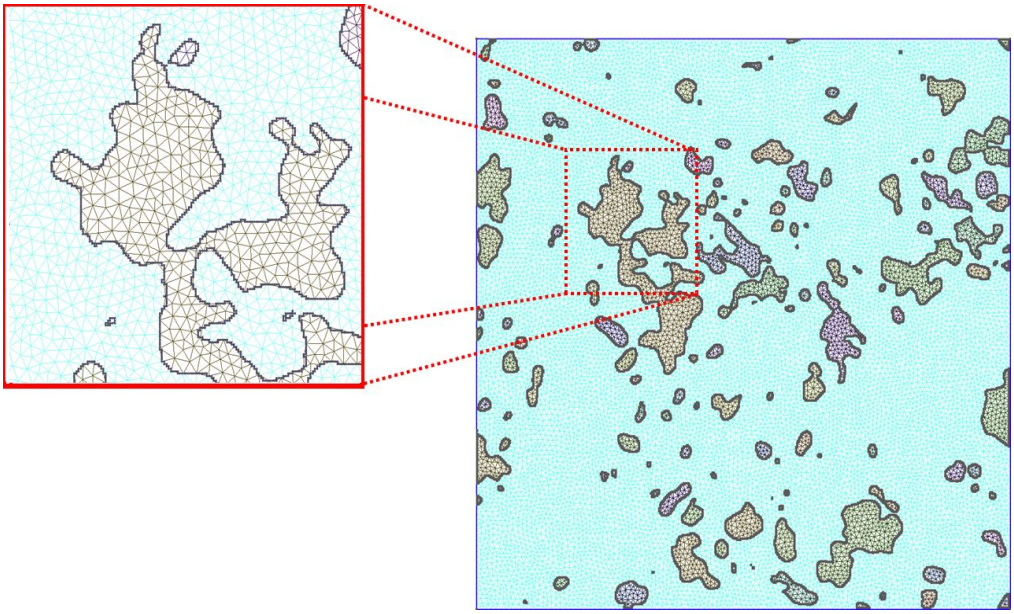

Figure 4.10: Mesh of the micro tomography image.

producer well and an injector well are used, respectively.

These differences result in variations between the results obtained from the finite element models and those generated by IMEX. Primarily, these discrepancies arise because the well is coupled to the center of each cell, leading to inaccuracies. To mitigate these differences, it is employed refined meshes on the wells. It is advisable to refine the mesh within the edge cell that contains the well and move the well to the refined cell at the model boundary. This approach is implemented in this study, as illustrated in Figure 4.11. It can be

seen in figure 4.11 that the first cell is subdivided five times in the direction of the flow (horizontal direction). Another good practice used here is to set a high permeability value in the cells containing the wells. This is done to ensure uniform injection. In this study, these cells have 10 D of absolute permeability.

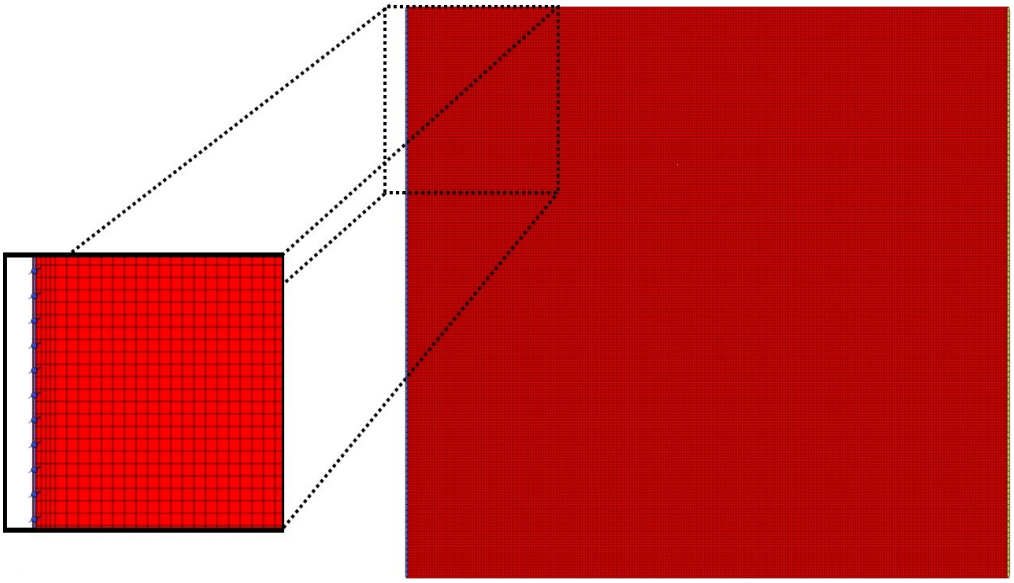

Figure 4.11: Porous matrix or matrix grid mesh configuration. This mesh configuration is used for the synthetic vug configuration, homogeneous $1\phi 1k$ Darcy model.

Based on the mesh configurations described earlier in this section, the parameter γ of the penalty term in equation (3-86) is investigated. In this analysis, γ was tested for the vug configuration (c) and using petrophysical properties of Table 4.1. The initial value Cruz used for evaluation purposes was derived from Cruz's [41] approach, in which boundary conditions were implemented utilizing the penalty model. Additionally, this value was systematically varied to assess its impact on the results. Since $\gamma = 0$, there is no penalty term in the equation, resulting in numerical divergence. As shown in Table 4.5, the results of the sensitive analysis to this parameter indicate that it has a negligible impact on the results. The relative difference in permeability between $\gamma = 1$ and $\gamma = 35$, for example, is 1.54×10^{-9}. Additionally, to evaluate the numerical consistency of γ, it was necessary to compare the outcomes of the Brinkman model with those of Darcy's model. In the Darcy model, the vug permeability was assumed to be 200 times higher than the matrix permeability. Both Brinkman and Darcy models yielded equivalent permeability values which were closely aligned with those presented in Table 4.5, with a relative difference less than 1 %. Therefore, throughout this chapter $\gamma = 35$ is assumed.

γ	$K^{eq}_{1\phi 1k}$ [mD]
1	142.035
10	142.035
35	142.035
100	142.035

Table 4.5: The influence of γ on the absolute permeability of the vug configuration (c).

4.4 Synthetic Domain Results

The following section presents the results for single-phase and two-phase flow in the synthetic domain configurations. Section (3.2) details the boundary conditions, sections (3.4.1) and (3.4.2) provide a detailed presentation of homogeneous and heterogeneous Darcy scenarios, and section (4.1) outlines the configuration employed for generating these scenarios

4.4.1 Single-Phase Flow

Figures 4.12 and 4.13 present the steady-state, single-phase flow velocity magnitude field predicted by the Brinkman model for the different vug configurations. The velocity ratio between the vug interior and the adjacent porous matrix exceeded 10, reaching values as high as 10^3 within selected zones close to the vug-matrix interface for the configurations (a)-(d) and the one obtained from the microtomography image. There are discernible areas of lower velocity within the boundaries of the porous matrix and vugs, delineated by blue shading. In case (e), it is evident that there is only a slight distortion in the velocity field near the lower and upper edge of the vug. For the other portions of the domain, the velocity in the vug is close to the velocity within the porous matrix. In these regions at the edge of the vug, there are also regions of low velocity.

The velocity magnitude along line AA, located at the center of the vugs, provides an interesting observation: the maximum velocity magnitudes within the vugs in cases (a), (b), and (c) exhibit remarkable similarity, despite differences in vug size configurations. Conversely, in case (d), the velocity magnitude is higher. A single channel with very low flow resistance is responsible for this phenomenon. In this study, this phenomenon is called channeling. Fluid migrates from the porous matrix to the vug due to its lower flow resistance, resulting in a low-velocity zone near the boundary between the vug and the porous matrix. In comparison to case (e), where the vug is

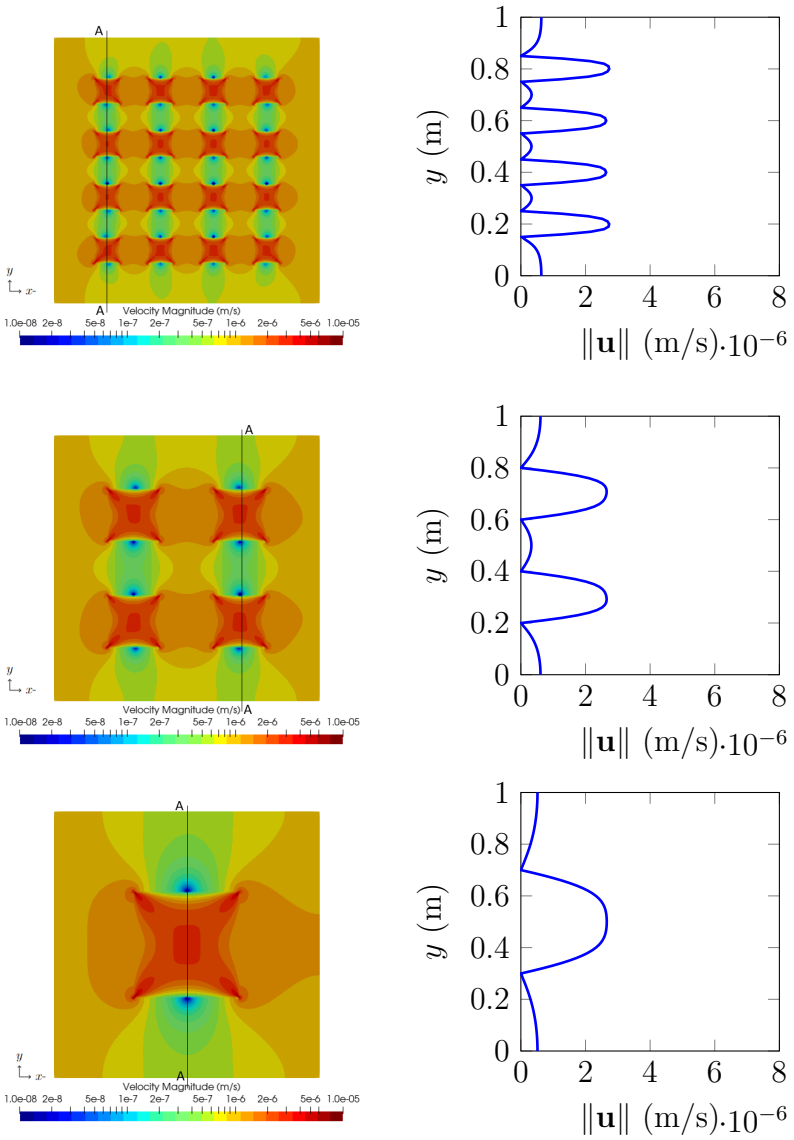

Figure 4.12: Velocity magnitude (m/s) field on the steady-state regime for the vug configuration (a), (b), and (c). For each case, it is presented the velocity profile in the cut AA.

aligned perpendicular to the flow, case (e) exhibits the smallest ratio between vug and porous matrix velocity. In the microtomography image domain, which is more representative of reality, the velocity magnitude within the vugs is comparable to values obtained in synthetic domains. The dispersed distribution of vugs eliminates any discernible preferential flow path. Within the porous matrix, certain regions consistently exhibit low velocities, and these areas are surrounded by vugs. The highest speeds are recorded in the region of the vug in this case. Based on the velocity data, the Reynolds number can be estimated in order to determine whether the simplifying assumptions are valid. Based on water properties at standard temperature, the Reynolds number varies from 5.0 $\times 10^{-3}$ for the microtomography image to 0.8 for the synthetic vug sample

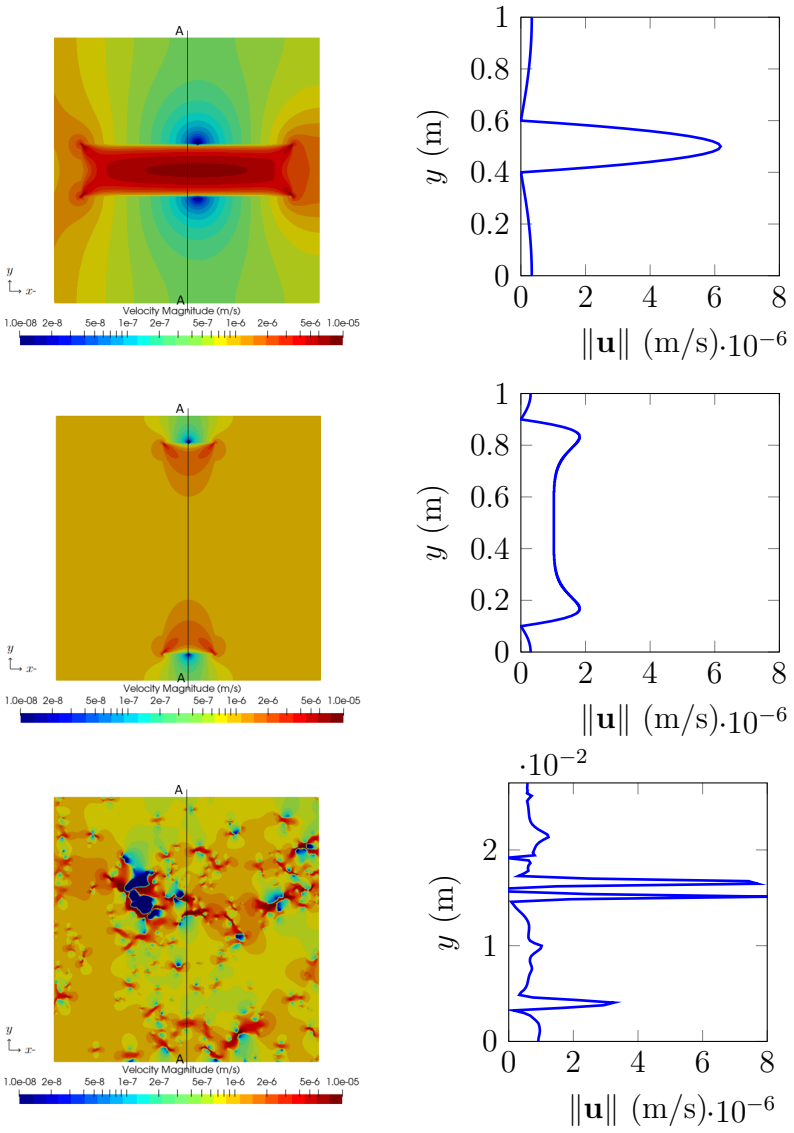

Figure 4.13: Velocity magnitude (m/s) field on the steady-state regime for the vug configuration (d), (e), and the micro tomography sample. For each case, it is presented the velocity profile in the cut AA.

(d). Despite of the fact that Re for sample (d) is a little higher, it is still possible to consider that the hypotheses are valid.

Figures 4.14 and 4.15 present the pressure distribution across section BB along then center of the vugs. Clearly, the pressure gradient within the vug areas is significantly smaller than in the porous matrix for all vug configurations. In these regions, the resistance to flow is much lower than in the surrounding porous matrix. Cases (a)-(c) exhibit nearly identical pressure difference between Γ_1 and Γ_2, while case (d) displays a considerably smaller pressure difference. This variation can be attributed to the distribution of macroporosity throughout the domain, which substantially reduces flow resistance in the horizontal direction. Due to the dimensions of the domain,

the microtomography pressure gradient is smaller than that of the other cases. It is observed, however, that the pressure profile over the domain is similar to the pressure profiles observed in cases (a)-(e) in which the vugular region exhibits a significantly smaller gradient of pressure compared to the porous matrix.

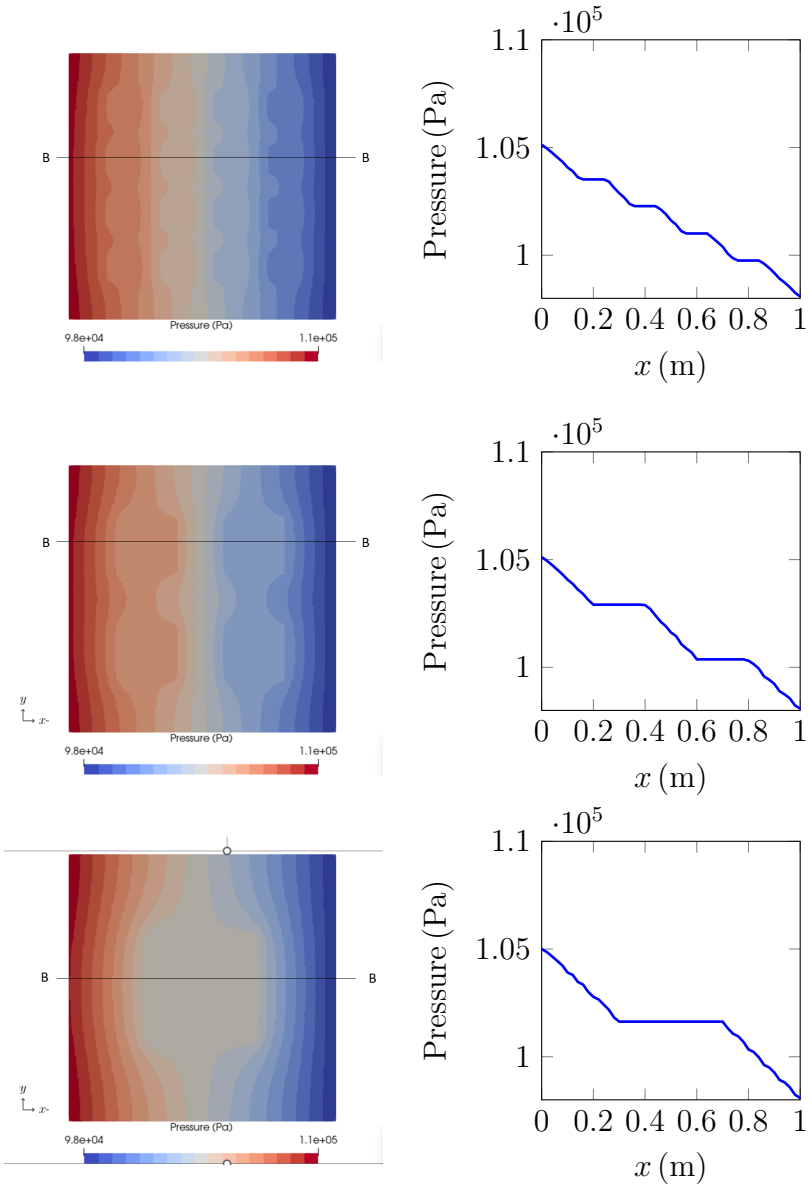

Figure 4.14: Pressure (Pa) field on the steady-state regime for the vug configuration (a), (b), and (c). For each case, it is presented the pressure profile in the cut BB.

The absolute permeability for the homogeneous $1\phi 1k$ model (i.e. on the coarse scale) is determined from the results obtained by the Brinkman model for single-phase flow in the steady state. The results are presented in Table (4.6)

A heterogeneous Darcy model has been used in the literature to analyze

Vug Configuration	$K^{eq}_{1\phi 1k}$ [mD]	K^{ϵ}_{M} [mD]	K^{ϵ}_{Vug} [mD]
(a)	1.41	1	5.3×10^{2}
(a)	14.11	10	5.3×10^{3}
(a)	141.17	100	5.3×10^{4}
(a)	1411.71	1000	5.3×10^{5}
(b)	1.41	1	5.9×10^{2}
(b)	14.19	10	5.9×10^{3}
(b)	141.92	100	5.9×10^{4}
(b)	1419.23	1000	5.9×10^{5}
(c)	1.42	1	1.5×10^{2}
(c)	14.20	10	1.5×10^{3}
(c)	142.05	100	1.5×10^{4}
(c)	1420.51	1000	1.5×10^{5}
(d)	2.38	1	7.6×10^{1}
(d)	23.89	10	7.6×10^{2}
(d)	238.94	100	7.6×10^{3}
(d)	2389.46	1000	7.6×10^{4}
(e)	1.42	1	1.5×10^{3}
(e)	14.20	10	1.5×10^{4}
(e)	142.05	100	1.5×10^{5}
(e)	1420.51	1000	1.5×10^{6}
Tomog	1.54	1	1.1×10^{4}
Tomog	15.40	10	1.1×10^{5}
Tomog	154.02	100	1.1×10^{6}
Tomog	1540.15	1000	1.1×10^{7}

Table 4.6: The permeability obtained through the Brinkman model ($K^{eq}_{1\phi 1k}$) and the estimated absolute permeability (K^{ϵ}_{Vug}) for the vug region in the heterogeneous Darcy model for vug configurations (a)-(e) and the micro tomography sample.

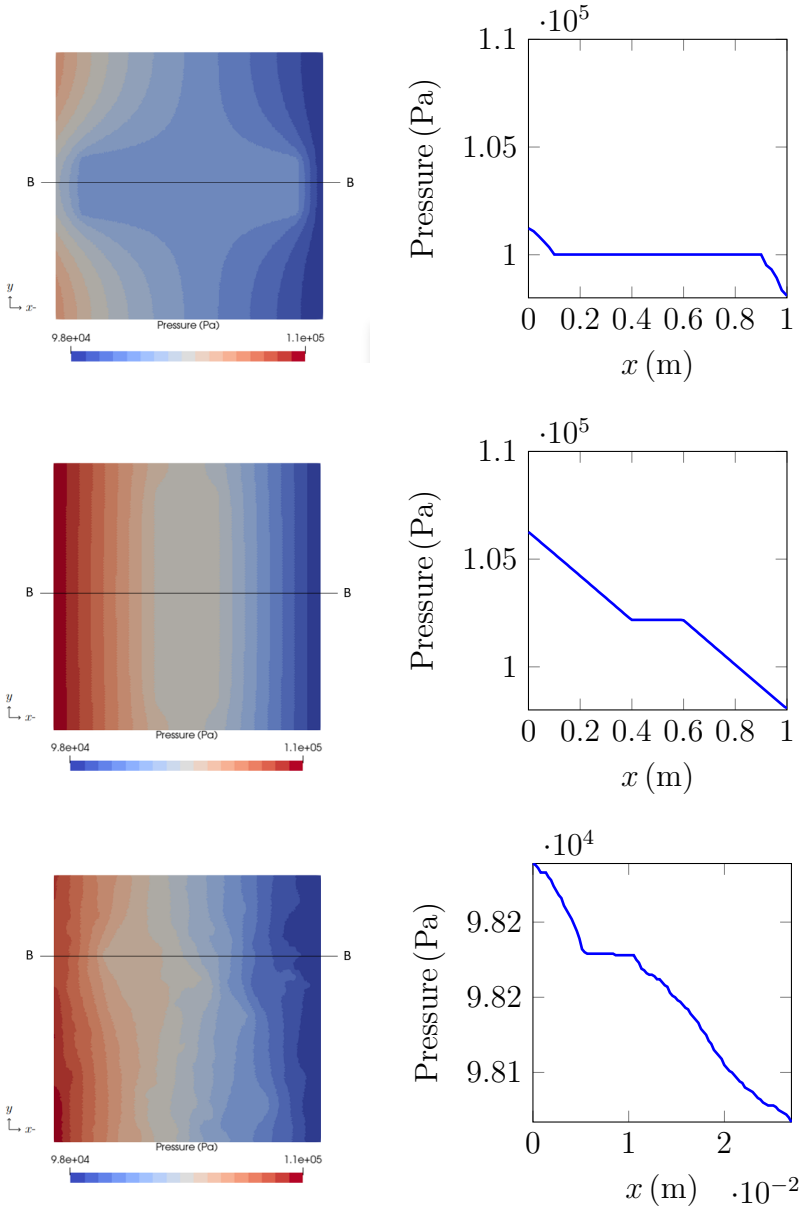

Figure 4.15: Pressure (Pa) field on the steady-state regime for the vug configuration (d), (e), and the micro tomography sample. For each case, it is presented the pressure profile in the cut BB.

flow through vuggy porous media. To model low flow resistance, the permeability of the vuggy region is set to an arbitrarily high value. However, the impact of this value on flow prediction is unclear. The flow field, calculated by employing the heterogeneous Darcy model with different values of the vug region permeability K^{ϵ}_{Vug}, is employed to determine the equivalent absolute permeability of the heterogeneous Darcy solution, denoted as K^{eq}_{hetD}. The relative disparity in the equivalent permeability between the system computed using the Brinkman model and the heterogeneous Darcy solutions is graphically presented in Fig.4.16 for the different vug configurations under consideration.

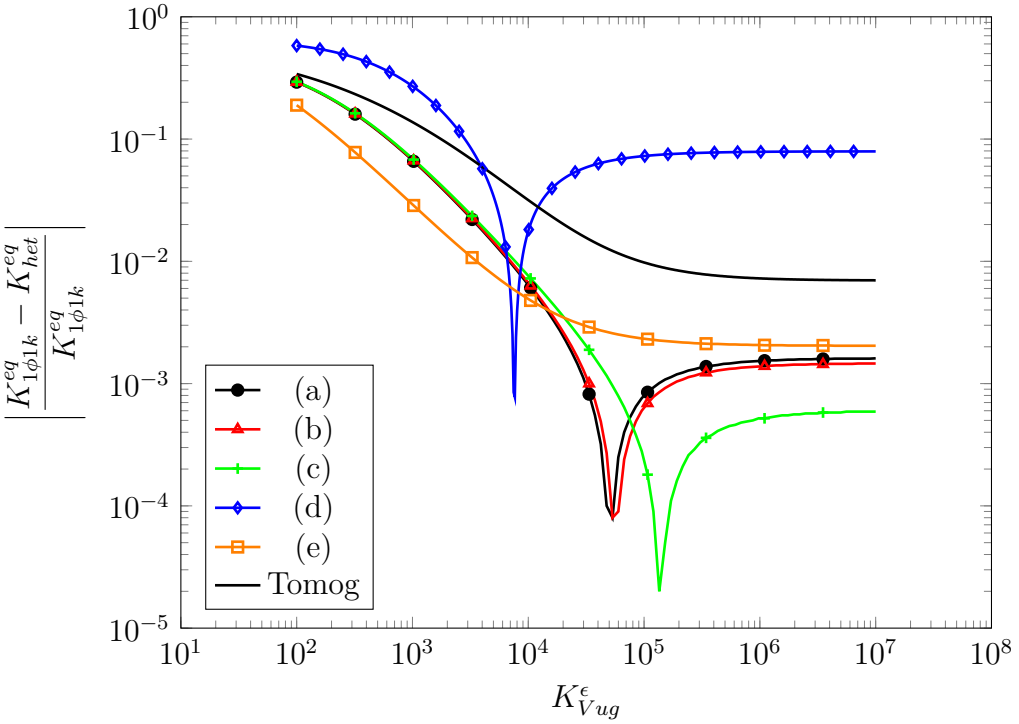

Figure 4.16: The relative error between the single-phase steady state flow obtained by the Brinkman model and the flow obtained by the heterogeneous $1\phi 1k$ Darcy model based on the vug permeability (K^{ϵ}_{V}) of the vug configurations (a)-(e) and the micro tomography.

According to Fig.4.16, for vug configuration (d), characterized by a channel aligned with the flow, the difference is nearly 10 % when $K^{\epsilon}_{Vug} \to \infty$. In contrast, for vug configurations (a)-(e), the relative difference is significantly lower, below 0.2 %. Interestingly, for synthetic configurations (a)-(d), there is a specific value of the imposed vuggy permeability K^{ϵ}_{Vug} that minimizes the relative difference between the computed equivalent absolute permeabilities. The results derived from the micro tomography image domain differ slightly from those derived from synthetic vug configurations. The relative difference between the equivalent permeability calculated with Brinkman and heterogeneous Darcy models decreases as the imposed permeability of the vug region increases. The minimum difference, approaching 1 %, is asymptotically achieved for $K^{\epsilon}_{Vug} > 10^6$. A comparable trend is observed in the vug configuration (e); however the error is lower. Table (4.6) presents the K^{ϵ}_{Vug} that minimizes the differences between the computed absolute permeability, followed by the equivalent permeability of the porous medium. The configurations of vugs (a), (b), and (c), yield equivalent permeability values that are similar. Conversely, the vug configuration (d) produces substantially higher equivalent permeability. On the other hand, vug configuration (e) has the lower $K^{eq}_{1\phi 1k}$. The results

demonstrate the impact that vug distribution within the porous matrix has on equivalent permeability.

Figure 4.17 shows the impact of matrix permeability (K_M^ϵ) on the results. This analysis aims to determine the influence of the porous matrix on the optimum vug permeability that minimizes the differences between Brinkman and the heterogeneous Darcy model. This is accomplished by varying the porous matrix permeability on a fine scale and calculating the value of $K_{1\phi 1k}^{eq}$ for each K_M^ϵ, covering the range form 1 mD to 1000 mD.

Independent of the vug configuration, different values of vug permeability minimize the error function for each matrix permeability value. Moreover, the ratio between K_{Vug}^ϵ and K_M^ϵ is the same in all scenarios. Based on the variation in the permeability of the matrix, it is evident that there is a change in the pressure drop inside the vug. This means that the permeability of the free-flowing region is also influenced by the surrounding porous medium. As a result, establishing an absolute permeability for a vug region cannot be evaluated independently in the matrix, making Brinkman modeling crucial for establishing equivalent petrophysical properties for the vug region. Therefore, it is necessary to evaluate the vug permeability for each set of matrix permeability, particularly for vug configurations (d).

As highlighted by the results discussed here and corroborated by previous work [54, 56, 62, 61], vuggy porous media have equivalent petrophysical properties that strongly depend on the geometry and configuration of vugs and fractures, and the Brinkman model is useful for assessing equivalent properties of heterogeneous porous media.

4.4.2 Two-Phase Flow

In this section, the displacement of oil by water injection is analyzed for different configurations of vugs. Figure 4.18 displays the evolution of the water saturation field predicted by the Brinkman model for the six vug configurations at three dimensionless injected water porous volumes (t_D). The first row of the diagram illustrates the solution of water saturation through the porous matrix alone (i.e., with no vugs). This scenario corresponds to the properties of the porous matrix without a vugular system, which has a permeability of 100 mD and porosity of 0.2. The evolution of the water front in case (d), with the long vug aligned with the flow direction, differs significantly from the other cases. Because of the lower flow resistance along the vug, the water front accelerates, resulting in a non-uniform saturation profile and an early water breakthrough ($t_D = 0.579$). The low velocity regions in the porous matrix that

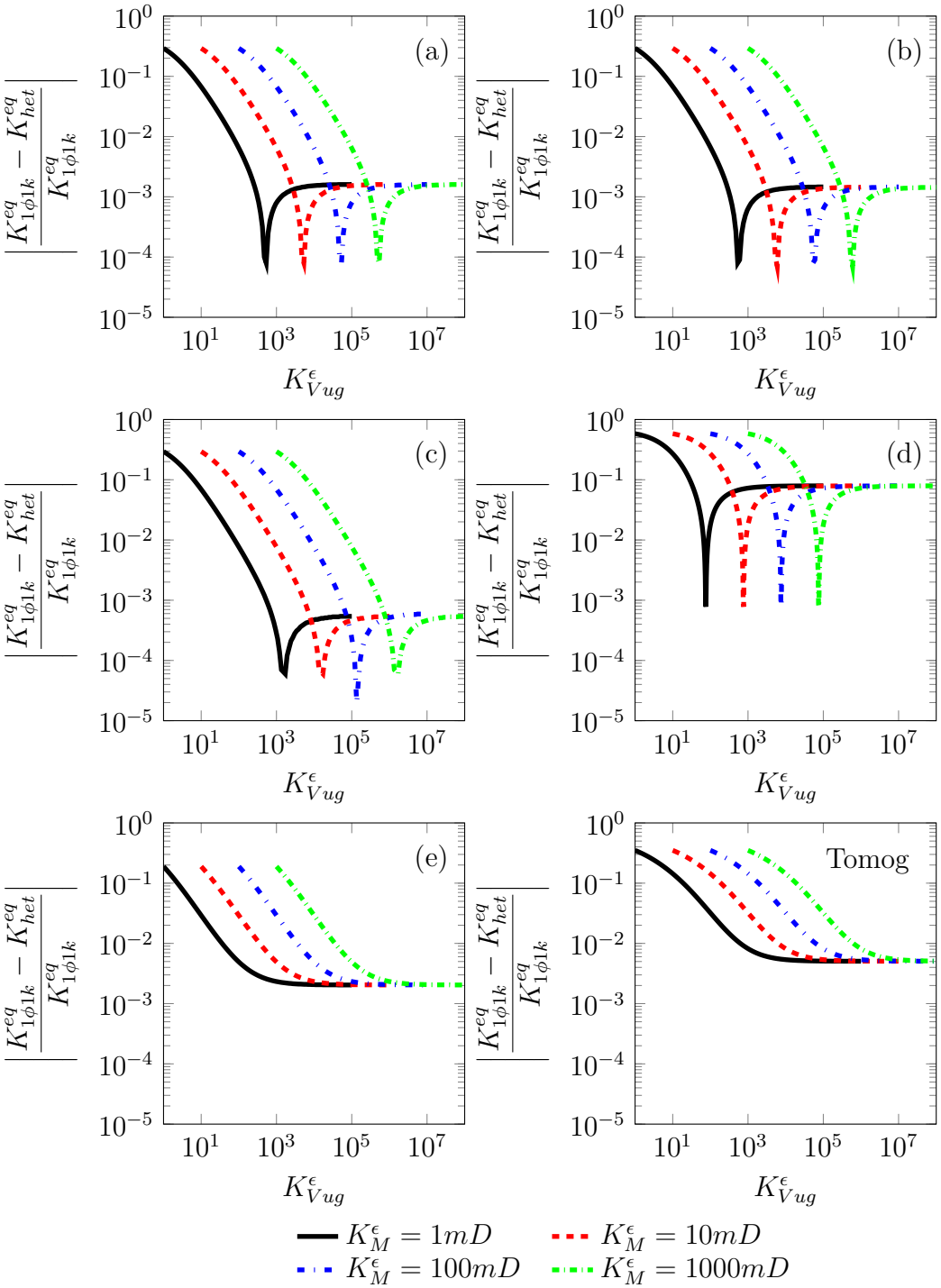

Figure 4.17: The relative error between the Brinkman model and the heterogeneous Darcy model on a single-phase steady state flow is evaluated when the matrix absolute permeability (K^{ϵ}_{M}) is assessed for each of the vug configurations (a)-(d) and the microtomography at 1mD, 10mD, 100mD, and 1000mD. For each K^{ϵ}_{M} and for each vug configuration the vug permeability (K^{ϵ}_{Vug}) is evaluated.

are aligned with the flow direction result in lower water saturation. Despite the higher velocity in the vugs compared to the porous matrix, the water front in configurations (a)-(c) and (e) appears to be slower in the vug domain than in the porous domain. This can be explained by the larger oil volume that must be displaced in the vugs.

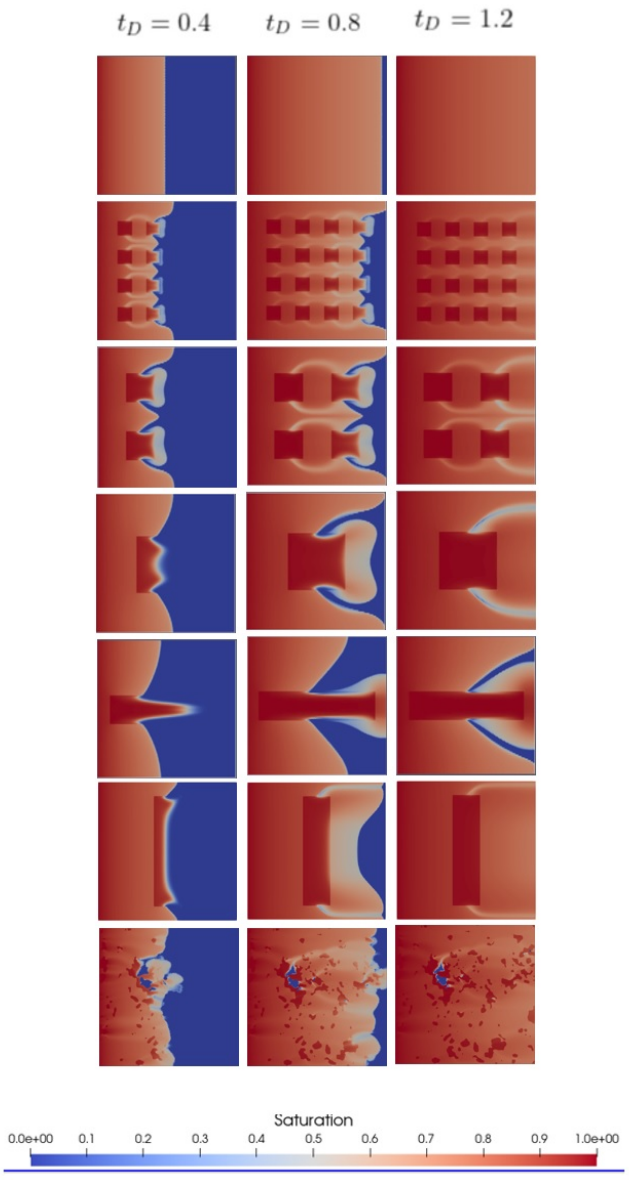

Figure 4.18: Comparison of the saturation field between a porous matrix without vug modeled by Darcy equation, six distinct vugular configurations by Brinkman model. These scenarios are analyzed at three different t_D in order to examine the impact of water injection on the saturation field.

Figure (4.19) illustrates the evolution of W_{cut} in terms of t_D across different vug configurations and the porous matrix devoid of vugs. The water cut evolution in the porous matrix alone, represented by the dashed line in

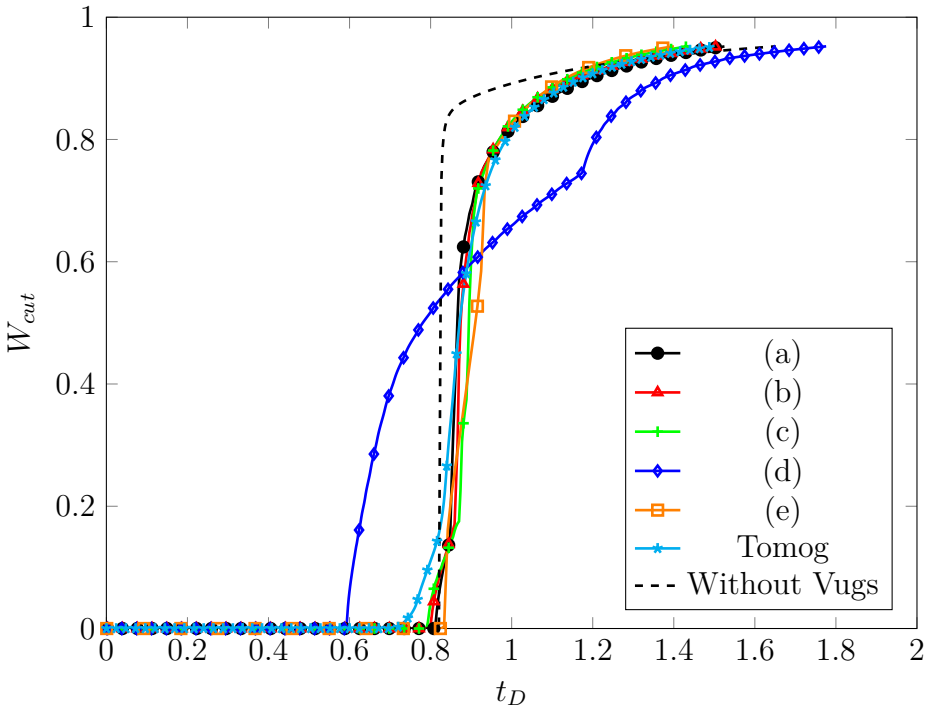

Figure 4.19: Analysis of the W_{cut} as a function of t_D for the samples (a)-(e) and the micro tomography image using the Brinkman model compared with the porous matrix without vugs.

the plot, is abrupt due to a uniform water saturation front, resulting in water breakthrough at $t_D = 0.81$. In the configurations (a)-(c) and (e) the water production curves exhibit similar evolution, but a slower water production increase due to non-uniform water front. The water breakthrough times in these cases are comparable and slightly lower than the porous matrix without vugs: (a) $t_D = 0.797$, (b) $t_D = 0.782$, (c) $t_D = 0.774$. For case (e), with the long vug aligned perpendicularly to the main flow direction, water breakthrough is $t_D = 0.83$, which is slightly higher than the porous matrix value. As anticipated, in case (d) the water breakthrough happens much earlier at $t_D = 0.579$, which is explained by the channeling effect, and the water cut growth is much slower than in the other cases. The vug configuration derived from the micro tomography image, demonstrates a water cut curve evolution similar to cases (a)-(c). The water breakthrough occurs at $t_D = 0.71$. This is attributed to the uneven distribution of voids in the domains, resulting in an irregular water front.

The heterogeneous Darcy model predictions are compared to the Brinkman solution for all cases explored. In the two-phase heterogeneous Darcy model, the value of the vug region permeability K^{ϵ}_{Vug} is chosen as the one that minimizes the difference to the equivalent absolute permeability predicted by

the Brinkman model, which is shown in Tab.(4.6). Figure 4.20 shows the comparison between the water cut predictions of the heterogeneous Darcy and Brinkman models. Both models predicted similar evolution for water production for all vug configurations. Generally, water breakthrough occurs first in the Darcy model. This small delay in water breakthrough in the Brinkman model may be associated with the viscous dissipation in the vug domain, which is not considered in the heterogeneous Darcy formulation.

The evolution of the pressure difference during oil displacement predicted by both the Brinkman model and the heterogeneous Darcy models are presented in Fig.(4.21). The pressure difference is normalized by the pressure difference at $t_D = 0$, which corresponds to the pressure difference of oil single phase flow. Notably, the results obtained with both Brinkman's and Darcy's heterogeneous models are almost equal at $t_D = 0$, since the heterogeneous Darcy model is constructed to yield an absolute permeability very close to that obtained with the Brinkman model (the relative difference is lower than 1 %). However, the evolution of the pressure difference predicted by each model is quite different. In particular, the Brinkman model requires a higher inlet pressure level to maintain an identical flow rate when compared to the heterogeneous Darcy model. In some instances, discrepancies may reach as high as 40 %. The peak of pressure represents the advancement of the water front as it crosses the interface between the matrix and the vug, as well as Γ_2. On the heterogeneous Darcy model, these peaks have a much lower intensity and are almost imperceptible in the plot. The phenomenon may be attributed to the viscous dissipation inside the vugs that is neglected in the heterogeneous Darcy model. The pressure difference results show that using a heterogeneous Darcy model to describe two-phase flow in vuggy porous media may lead to inaccurate results, as it neglects the viscous pressure drop along the vugs.

The fine-scale Brinkman model is used in order to test the impact of porous matrix on two-phase flow at permeability ranging from 1 mD to 1000 mD. Notably, the results for W_{cut} and $\dfrac{\Delta p_{t_D}}{\Delta p_{t_D=0}}$ are the same across the six scenarios, as depicted in figure 4.20 and 4.21 (the case of the porous matrix with 100 mD). There is a variation in inlet pressure between scenarios that is attributed to differences in flow resistance as a result of the variation of equivalent permeability, as can be seen in Table (4.6).

In reservoir scale models, it is usually not feasible to use a mesh that maps the vugular region. A single model cell should describe the complex dynamics of flow through the porous matrix and vugs. For this purpose, a homogenization of the domain is applied. In this study, Brinkman's results are used to determine equivalent relative permeability curves for a homogeneous

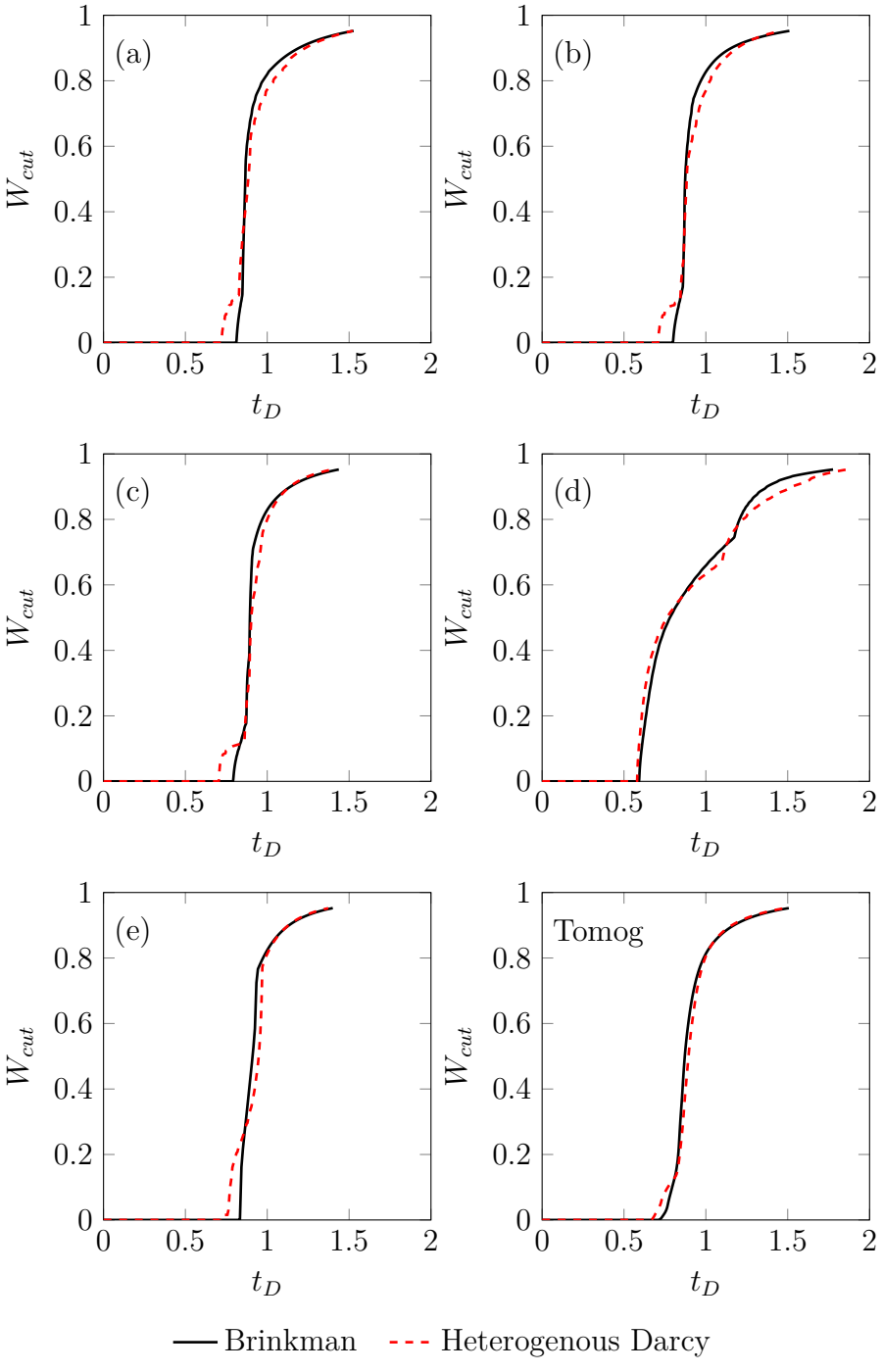

Figure 4.20: The impact of the two-phase flow is examined by evaluating the pressure difference as a function of the injected porous volume for both the Brinkman and Darcy heterogeneous $1\phi 1k$ Darcy models. This analysis is conducted for the vug configurations (a)-(e) and the micro tomography image.

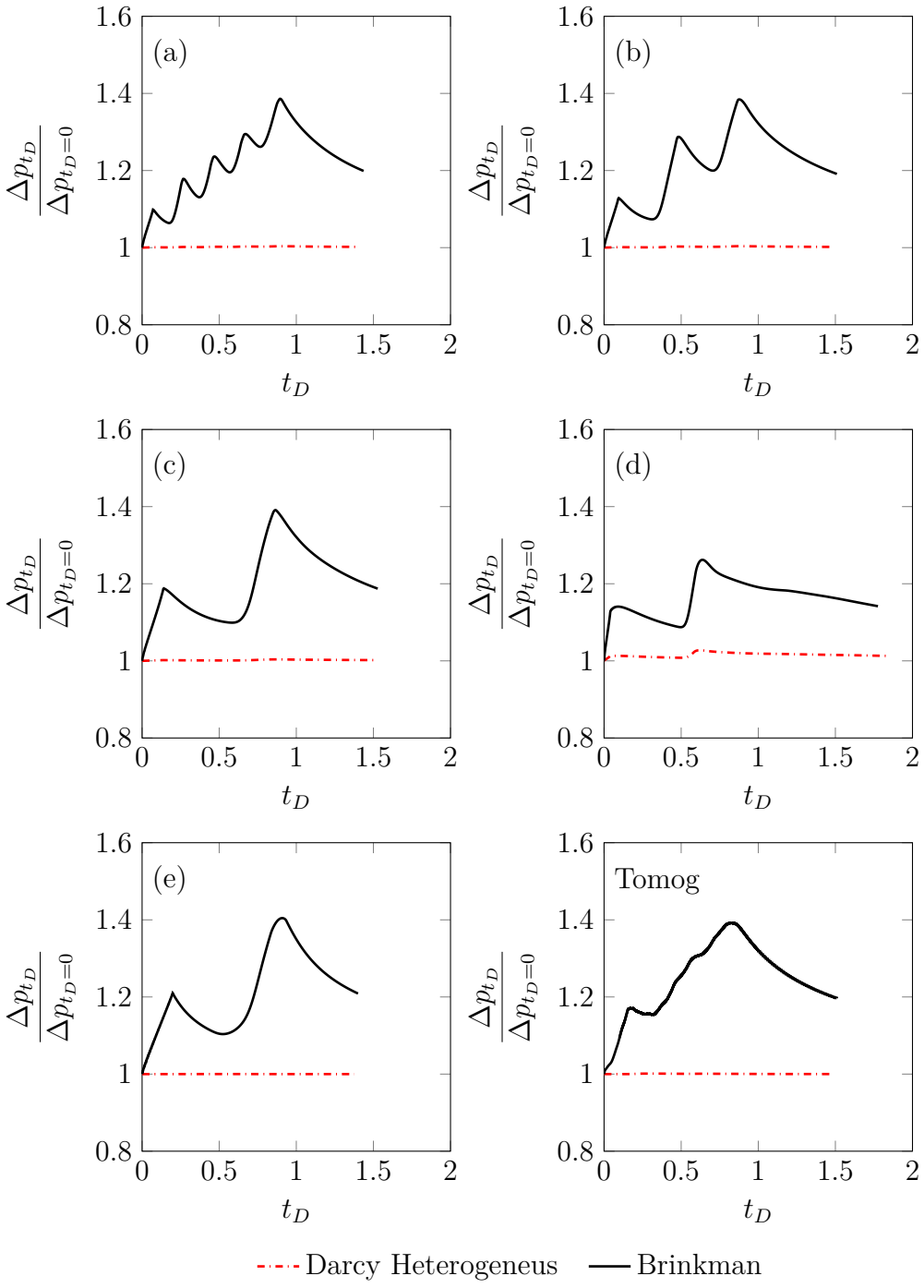

Figure 4.21: The impact of the two-phase flow is examined by evaluating the dimensionless pressure difference as a function of the injected porous volume for both the Brinkman and heterogeneous $1\phi 1k$ Darcy models. This analysis is conducted for the vug configurations (a)-(e) and the micro tomography image.

Darcy model. These curves are obtained by an optimization procedure, as explained before. The Corey's exponents and the relative permeability water end-point of the equivalent relative permeability curves are determined such that the difference between the water flow rate at the outlet boundary predicted by the Brinkman and homogeneous Darcy models is minimized. The water production curves predicted by the Brinkman model and the optimized homogeneous Darcy model are presented in Fig.(4.22). In the homogeneous Darcy results, the water cut curves exhibit a sudden change due to uniform water saturation along the vertical direction. In the Brinkman model predictions, the water cut increase occurs slower in response to a non-uniform water front. Despite this small difference in behavior, the homogeneous Darcy model describes the overall behavior for the synthetic geometries (a)-(c), (e), and the micro tomography image domain. For the case with a long vug aligned to the flow direction, the evolution of water production obtained with Brinkman model presents two distinct inclinations, which is directly related to the early breakthrough of the water front. This behavior cannot be accurately captured by an homogeneous model. Furthermore, this behavior is not physically coherent, since a homogeneous medium is expected to have an abrupt evolution of the injected water saturation. The optimized Corey's parameters and the corresponding RMSE value, defined in eq.(3-96), for each case are presented in Tab.4.7. As expected, the higher RMSE value is for case (d).

Figure 4.23 presents the evolution of the pressure difference during oil displacement for the Brinkman and the homogeneous $1\phi 1k$ Darcy model. In cases (a)-(c), the pressure difference between inlet and outlet follows the same pattern as in the Brinkman model. In the homogeneous model for $1\phi 1k$, the same phenomenon is not observed. Sample (a) differs significantly from cases (b) and (c). An explanation for this discrepancy can be found in the occurrence of local minimums during History Matching. Nevertheless, despite these variations, it can be concluded that the homogeneous $1\phi 1k$ model effectively captures fine-scale effects on a coarse scale. This is particularly evident in case micro tomography vug configuration, where the equivalent pressure gradient closely matches throughout the operational range.

Consistency tests in numerical optimization are designed to determine whether an optimization algorithm consistently produces dependable results under different conditions. In general, consistency refers to the algorithm's ability to reach an optimal solution, or a close proximity to one, regardless of minor changes in the parameter values or initial conditions. Evaluations of this type are vital to ensuring the robustness and reliability of an optimization

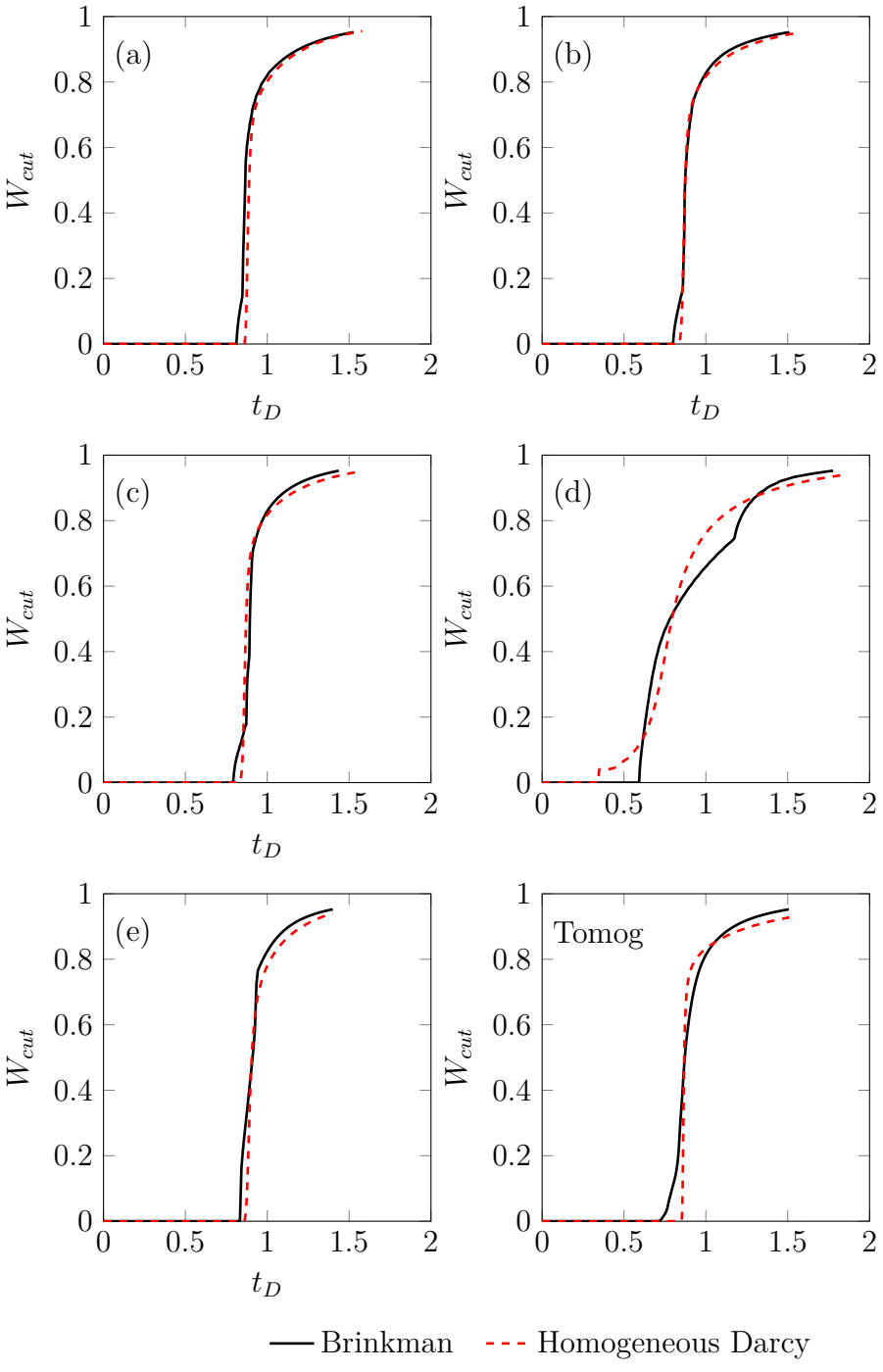

Figure 4.22: Comparative analysis of the homogeneous $1\phi 1k$ Darcy model based on the new pseudo-relative permeability curves and the Brinkman model for vug configuration (a)-(e) and the micro tomography image.

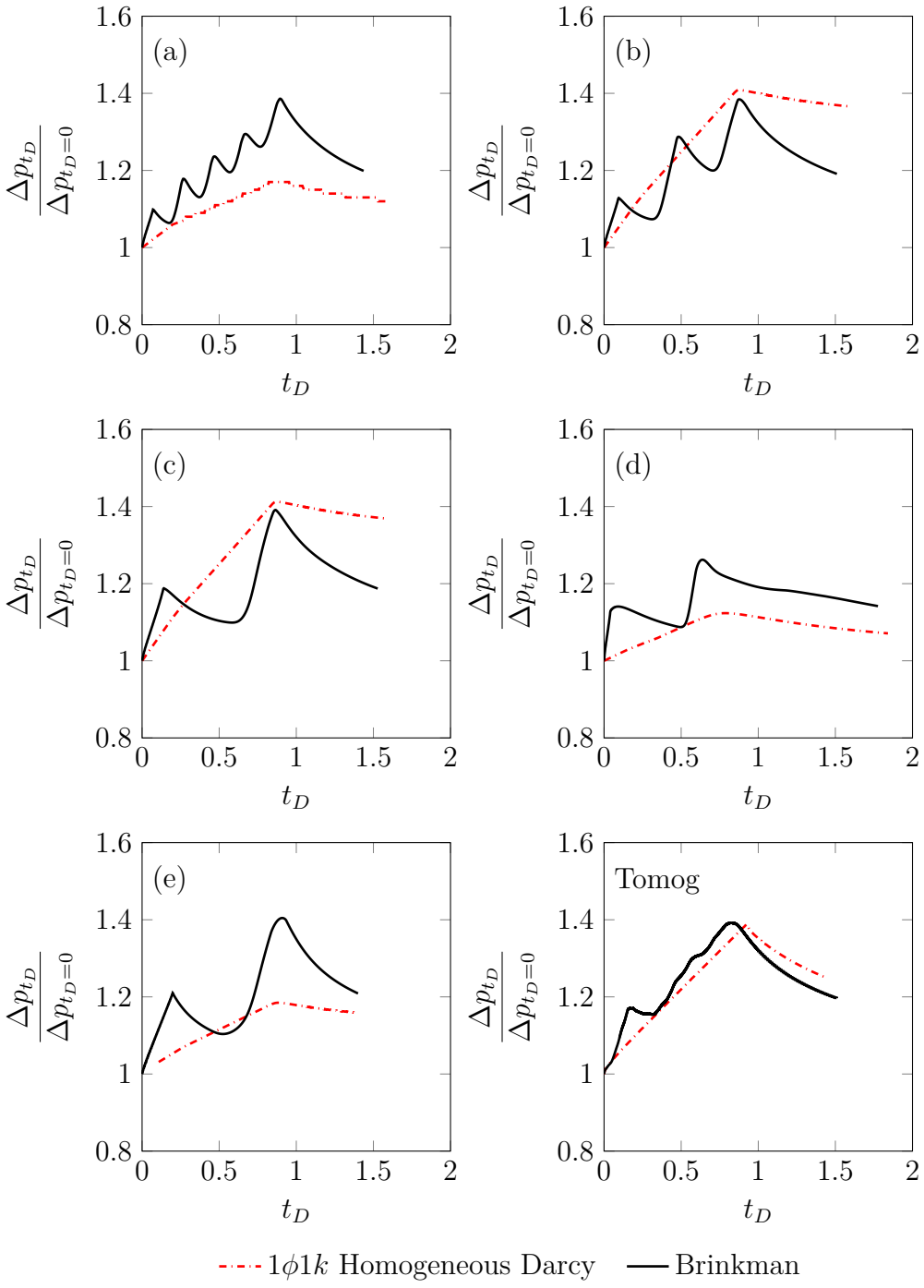

Figure 4.23: The impact of the two-phase flow on the dimensionless pressure difference as a function of the injected porous volume for both the Brinkman and homogeneous $1\phi 1k$ Darcy models. This analysis is conducted for the vug configurations (a)-(e) and the micro tomography image

	Ω_M		Ω_V		$\Omega^{eq}_{1\phi 1k}$			
Case	n_o	n_w	n_o	n_w	n_o	n_w	k^0_{rw}	RMSE
a	2.00	2.00	1.00	1.00	1.40	1.16	0.91	3.10
b	2.00	2.00	1.00	1.00	1.58	1.00	0.76	1.90
c	2.00	2.00	1.00	1.00	1.59	1.00	0.76	0.98
d	2.00	2.00	1.00	1.00	1.89	0.77	1.00	5.77
e	2.00	2.00	1.00	1.00	1.38	1.00	0.88	3.12
Tomog	2.00	2.00	1.00	1.00	1.88	1.28	0.90	0.11

Table 4.7: The relative permeability parameters for each vug scenario for the homogeneous $1\phi 1k$ Darcy model to determine $\Omega^{eq}_{1\phi 1k}$.

algorithm, as they enable the detection of potential issues such as numerical instabilities, sensitivity to disruptions, or oscillatory behavior. Typically, these assessments involve assigning the algorithm to a series of well-defined test scenarios, where the optimal solution is either known or estimable, and analyzing its performance in relation to each scenario. Aside from offering valuable insight into the effectiveness and applicability of an optimization algorithm across a variety of problem types, these assessments are also helpful in determining which method is most appropriate for particular problems.

For this study, a consistency test is conducted on vug configuration (c), where the inlet velocity in Γ_1 is systematically altered on two additional occasions. Specifically, concerning the velocity ascertained in the preceding experiments, velocities are appraised in increments of five ($\mathbf{u}_{in} = [5 \times 10^{-6}, 0.0]$ m/s) and ten ($\mathbf{u}_{in} = [10^{-5}, 0.0]$ m/s) times the initially evaluated velocity. All other parameters remain consistent with those delineated in table 4.1.

		$\Omega^{eq}_{1\phi 1k}$		
Vug Configuration	Inlet Velocity (m/s)	n_w	n_o	k^0_{rw}
(d)	10^{-6}	1.00	1.59	0.98
(d)	5×10^{-6}	0.96	1.57	1.00
(d)	10^{-5}	0.91	1.67	1.00

Table 4.8: The relative permeability parameters for vug configuration (d) and for the homogeneous $1\phi 1k$ Darcy model to determine $\Omega^{eq}_{1\phi 1k}$ for three different inlet velocities.

Figure 4.25 illustrates the outcomes of altering the inlet velocity concerning W_{cut} and $\dfrac{\Delta p_{t_D}}{\Delta p_{t_D=0}}$ as a function of t_D. Brinkman model demonstrate notable consistency, indicating that changes in the inlet velocity do not directly influence the results of W_{cut} and $\dfrac{\Delta p_{t_D}}{\Delta p_{t_D=0}}$. Following the analysis of the

numerical optimization process performed by CMOST, historical matching is again implemented to validate the results obtained by the Brinkman model in the $1\phi1k$ model. For the new inlet velocities, the same history matching procedure is followed. Table 4.8 summarizes the Corey parameters and figure 4.25 illustrates the relative permeability curve and fractional flow. As can be seen from the Table 4.8 , the values of k_{rw}, n_w, and n_o did not differ significantly between the cases. The variations on f_w curves are also minimal. Considering the lack of a momentum transport term in the Brinkman equation, compared to the Navier-Stokes equation, it would seem that the differences between scenarios altering the velocity at the inlet would be negligible. As for the history matching, there is also a satisfactory representation due to the alteration in inlet velocity, as both the relative permeability curves and the fractional water flow are closely aligned.

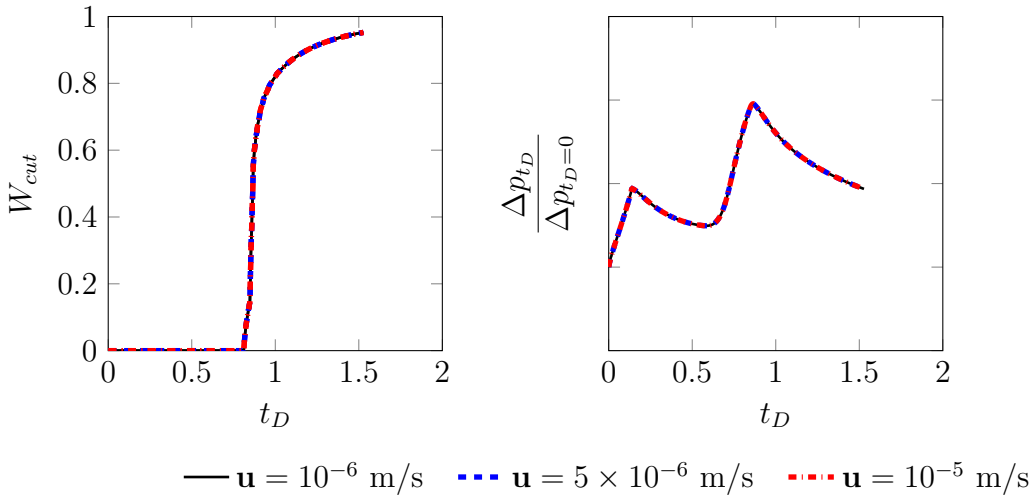

Figure 4.24: A comparison of relative permeability curves and fractional flow under three different inlet velocities for vug configuration (d).

4.5 Discussion

Initially, the heterogeneous $1\phi1k$ model is analysed. Arbitrarily assigning a value to K_{Vug} impacts the model outcomes. Selecting these values thoughtfully is essential, taking into account the distribution of geometries across the domain. Where vugs are dispersed within porous matrix and exhibit a low flow anisotropy, their permeability must be approximately five orders of magnitude higher than that of the matrix. Adopting this practice may, however, lead to challenges associated with poorly conditioned matrices in the numerical solver.

Machado et al. (2020) [110] proposed that karst formations exhibit constant absolute permeability in two-phase flow scenarios while the porous ma-

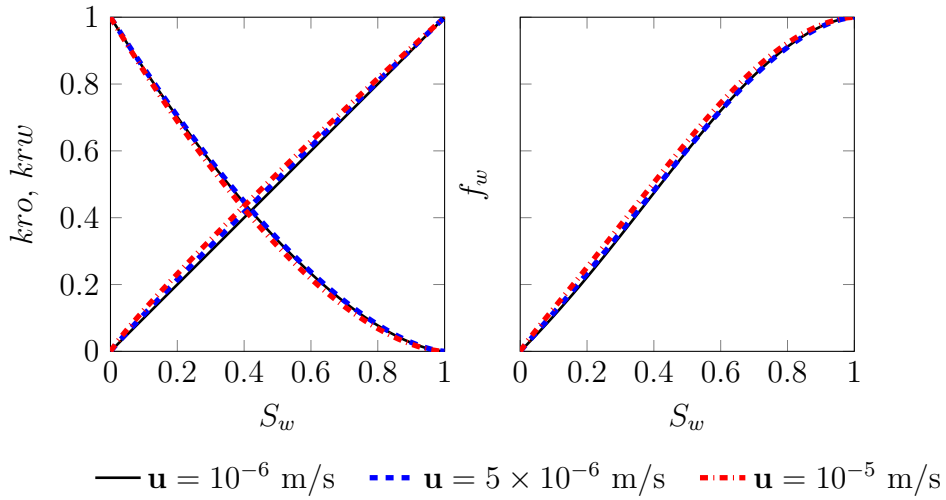

Figure 4.25: A comparison of relative permeability curves and fractional flow under three different inlet velocities for vug configuration (d).

trix absolute permeability varies. This assumption cannot be inconsistent or high K_{Vug}/K_M ratios. However, for less pronounced ratios, noticeable effects on two-phase flow become apparent. The saturation field reveals significant changes, altering saturation distribution across the domains in [110]. Nevertheless, the Brinkman model reveals that the porous matrix influences pressure drop in free-flow regions. Consequently, the ratio K_{Vug}/K_M remains constant for all porous matrix permeabilities. Since this ratio remains unchanged, there is no discernible impact on two-phase flow, as evidenced in this study. Assuming independent behavior of the free-flow region relative to the matrix may lead misrepresentation of the flow dynamics, which results in over optimistic conclusions in terms of oil and water productions, particularly when the porous matrix exhibits favorable petrophysical properties. The reason for this is that the porous medium becomes less heterogeneous, increasing recovery and delaying the arrival of water. The K_{Vug}/K_M ratio is expected to change when advection effects are comparable to momentum diffusion ones; however it is not the scope of this study.

Campos (2022) [60] compared the Brikman and Darcy models for a transient single-phase flow. The author made a similar assumption to that of [110], that is, the permeability of the vug remained unchanged while the permeability of the matrix were altered. The flow difference between the Brinkman and Darcy models is observed to increase with increasing matrix permeability, particularly with the lowest ratio of K_{Vug}/K_M. Due to the smaller difference in permeability between the vugular region and the matrix, the single-phase flow is distorted in a pronounced manner. This may be due to the fact that the permeability of the vug depends on the permeability of the

matrix as explores in this chapter.

Another consideration when analysing the Brinkman model with the $1\phi1k$ heterogeneous model is the challenge of simultaneously establishing equivalent saturation and pressure fields. An approach similar to that used in the homogeneous $1\phi1k$ case might be feasible to address this issue. It may be necessary to adjust the endpoints of the relative permeability curves or modify the shape of the curves themselves in order to influence the system's total mobility. It may be possible to achieve saturation and pressure fields similar to those observed in the Brinkman model by inducing a greater pressure drop in the vugular region. However, this approach would still require the use of the Brinkman model for numerical optimization. Therefore, this option does not provide a compelling means of simplifying problem.

It is clear that diffusive aspects contribute to the development of the saturation field in both Hallack et al. (2019) [45] and Coclite et al. (2014) [42]. In this study, this influence does not manifest clearly in the saturation field, but in the pressure field. As illustrated in figure 4.26, the saturation field results obtained by the Brinkman model are compared to those obtained by the heterogeneous $1\phi1k$ model. Saturation distributions at the water front show a slight disparity. When compared with Hallack et al. (2019) [45] and Coclite et al. (2014) [42] studies, the difference are significantly and may be directly related to boundary conditions. Due to the fact that Hallack et al. (2019) [45] and Coclite et al. (2014) [42] do not perform the pressure analysis in the same way as here, it is not possible to directly compare the results between the two.

In section 3.6.4 using a quarter-five-spot configuration with a central karst region, a simulation similar to Hallack's proposal was conducted to investigate influence of imposing of different boundary conditions. Figure 3.15 illustrates that modifying the injection point has a notable impact on the saturation field, highlighting the distinct variations between the Brinkman and Darcy models concerning saturation. The Brinkman model exhibits more pronounced channeling of the injected fluids and reduced sweep efficiency. These findings align with the conclusions drawn by Hallack et al. (2019) [45].

In the examination of the six scenarios presented in this chapter, it is demonstrated that the homogenization of a karstified porous medium within a single-porosity model is achievable under conditions of low anisotropy and a porous medium that does not exhibit pronounced channeling. Conversely, in situations characterized by significant channeling, an alternative methodology is necessary for modeling an equivalent porous medium. The next chapter explores the modeling of such mediums through the dual-continuum model.

There are some limitations on the methodology described in this study.

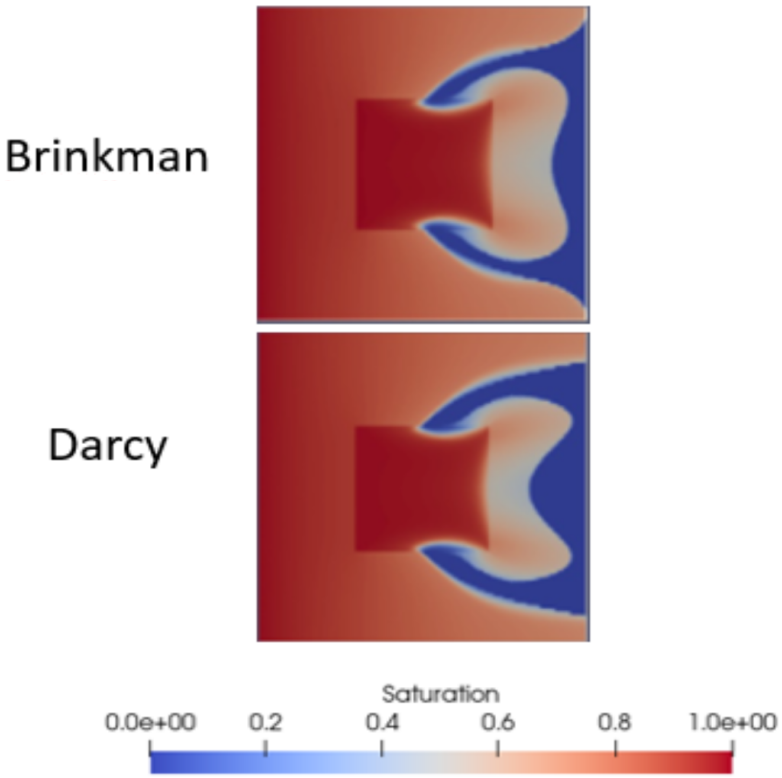

Figure 4.26: Comparison of the saturation field between a the Brinkman model and the Darcy models at vug configuration (d). This scenarios is analyzed at $t_D = 0.8$ in order to examine the impact of water injection on the saturation field.

It is common to treat relative permeability as the same in all directions on a domain. In the case of homogenization of the domain, it is evident that the flow pattern is different between cases (d) and (e) and the same relative permeability curve cannot be used to describe both flow patterns. There is only one difference between the two cases: the direction of the flow, which leads to significant differences in the coarse-scale modeling of the two cases. It remains an open issue to develop a comprehensive analysis that takes into account both cases using a unified methodology. An alternative approach involves treating relative permeability as a tensor quantity, as suggested by [114]. Nevertheless, this particular approach is not explored in the present study.

5
Comparison Between Brinkman and Dual-Continuum Models

5.1
Lajedo Arapuá Outcrop

Lajedo Arapuá is an outcrop from Jandaíra formation located in the Potiguar Basin, Rio Grande do Norte. This formation has an intense fractured system associated with karst features making the porous media highly heterogeneous. Quadros (2019) [22] proposed a complete geological model, modeling faceis, fractures and karsts. To characterize discrete faults and determine Lajedo's length, it was used a high-resolution aerial image captured by a drone and a scanning line survey. The depositional facies and karst features were modeled based on the Tijubina Outcrop, which exhibits a three-meter-thick Jandara Formation exposure. Since both outcrops are in the same geological context and are 380 meters apart, the author considered a suitable correlation between them. Quadros (2019) [22] developed the karst model based on the structural framework established for facies and fractures. Additionally, he gathered insight from both the Tijubina Outcrop and Lajedo Arapuá. In the Tijubina Outcrop, he differentiated zones with significant dissolution from those without. This facilitated the characterization of permeability anisotropy and helped the selection of preferential pathways within the simulation model. In the Lajedo Arapuá, areas with intense fractures were associated with vegetation because they indicated water infiltration points. Additional infiltration points were established based on the water table variation. Moreover, the model encompassed the hypogenic karst features, highlighting a single deep infiltration point and a shallow exfiltration point. Figure 5.1 illustrates the 3D karst model of Lajedo Arapuá.

The choice of the Lajedo Arapuá outcrop for this study is motivated by two reasons. Firstly, its configuration corresponds to a real-world scenario, adding complexity to the analysis. Secondly, the model is readily available for numerical implementation. Quadros (2019) [22] elaborated a 3D geological model which includes intricate karst features, fractures, and a porous matrix. Machado (2020) [110] constructed the flow model for the Lajedo Arapuá site using the IMEX software, relying on the geological model by Quadros (2019)

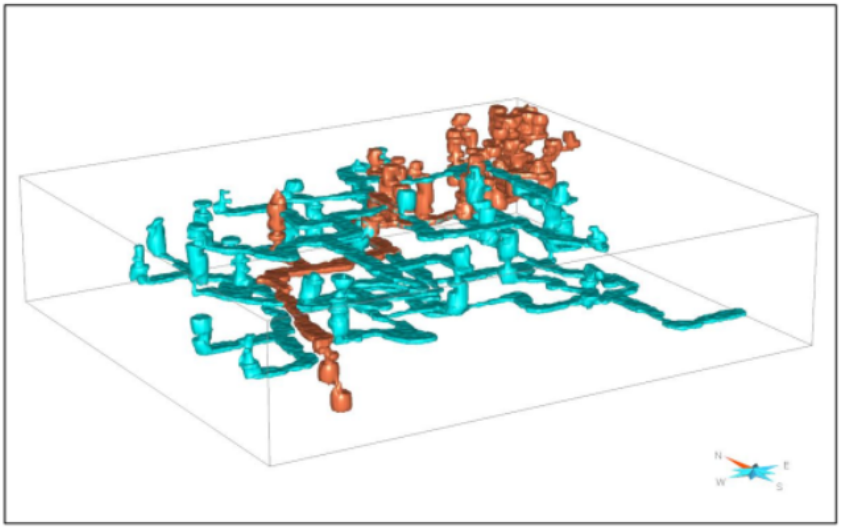

Figure 5.1: Epigenetic (orange) and hypogenic (light blue) karst model of the Arapuá area [22]. The figure has a vertical direction scalled by 20×.

[22]. Furthermore, Campos (2022) [60], based on the 3D geological model, derived 2D geometries from Lajedo Arapuá layers. His study investigated transient single-phase flow, employing both the Brinkman single-phase flow model and an IMEX model. The convergence of these factors significantly contributes to the development of scenarios.

Figure 5.2 illustrates three distinct vug configurations inspired by the Lajedo Arapuá outcrop. In the study by Campos (2022) [60], due to convergence issues at the field scale as reported by Quadros (2019) [22], the computational domain had to be scaled down significantly, from hundreds of meters to 2.36 m × 2.06 m. Each vug configuration corresponds to a distinct layer within this outcrop and emulates a particular geological formation observed in nature. The Arapua10 model features poorly connected and dispersed vugs embedded in the porous matrix. Arapua24 represents a karstified medium of the channel type, where all macropores are interconnected. Arapua17 combines elements of the two aforementioned configurations, with the majority of macroporosity interconnected and a small volume of isolated elements within the porous matrix.

Throughout this chapter, the porous matrix porosity and permeability are assumed to be constant across the domain. The petrophysical properties used in this study is summarized in table 5.1. The inlet velocity and outlet pressure remain constant in all numerical experiments, with $\mathbf{u}_{in} = [10^{-6}, 0.0]\ m/s$ and $p_{out} = 1\ atm$. At the inlet boundary, water is injected at a constant velocity, meaning $S_w = 1$ and $\mathbf{u} = \mathbf{u}_{in}$ on Γ_1. The layout of the boundary conditions is the same as in the figure 3.3.

Parameter	Value
ϕ_M^ϵ	0.2
K_{ii}^ϵ	100 mD
Relative Permeability Model	Corey
n_w^ϵ	2
n_o^ϵ	2
S_{wi}^ϵ	0
S_{or}^ϵ	0
k_{ro}^ϵ at $S_w = 0$	1
k_{rw}^ϵ at $S_w = 1$	1
μ_o	1 cp
μ_w	1 cp
$\mathbf{u}$ at Γ_1	$[10^{-6}, 0.0]$ m/s
p at Γ_2	1 atm
S_w at Γ_1	1

Table 5.1: Porous matrix and fluid parameters for the Arapua10, Arapua17, and Arapua24 vug cenarios in the Brinkman fine scale model.

5.2 Mesh Test

Arapuá vug configurations meshes are examined to achieve an optimal representation of flow dynamics while ensuring computational efficiency. This analysis is conducted to identify suitable meshes for two-phase flow solutions. The consistency of meshes across the two solvers is performed as the same in chapter four. In both scenarios, mesh refinement is evaluated as an enhancement to the solution based on the available computing resources. As the FEniCS models are run on a laptop with a simple configuration, they are consistently limited in all cases, whereas the IMEX software has access to the Petrobras Cluster. Consequently, FeniCS mesh selection is performed first. The IMEX mesh is comparable to the FEniCS mesh in terms of size. Furthermore, an investigation is conducted to determine whether mesh refinement in IMEX would improve results. Simulations conducted in IMEX do not benefit from mesh refinement. Coarsening meshes, also known as upgridding, is not considered. Similarly to chapter four, this approach is intentionally omitted in this study. Since two-phase flow can be significantly affected by scale transformation when meshes are coarse, this aspect of the study has been excluded.

The mesh selection for the Arapuá cases is conducted according to the same methodology presented in section 4. Table (5.2) and (5.3) details the meshes evaluated for each configuration and the numerical performance for them. The mesh generation parameters include the target mesh size for boundaries (cl_1), the target mesh size for the porous matrix-vug interface (cl_2),

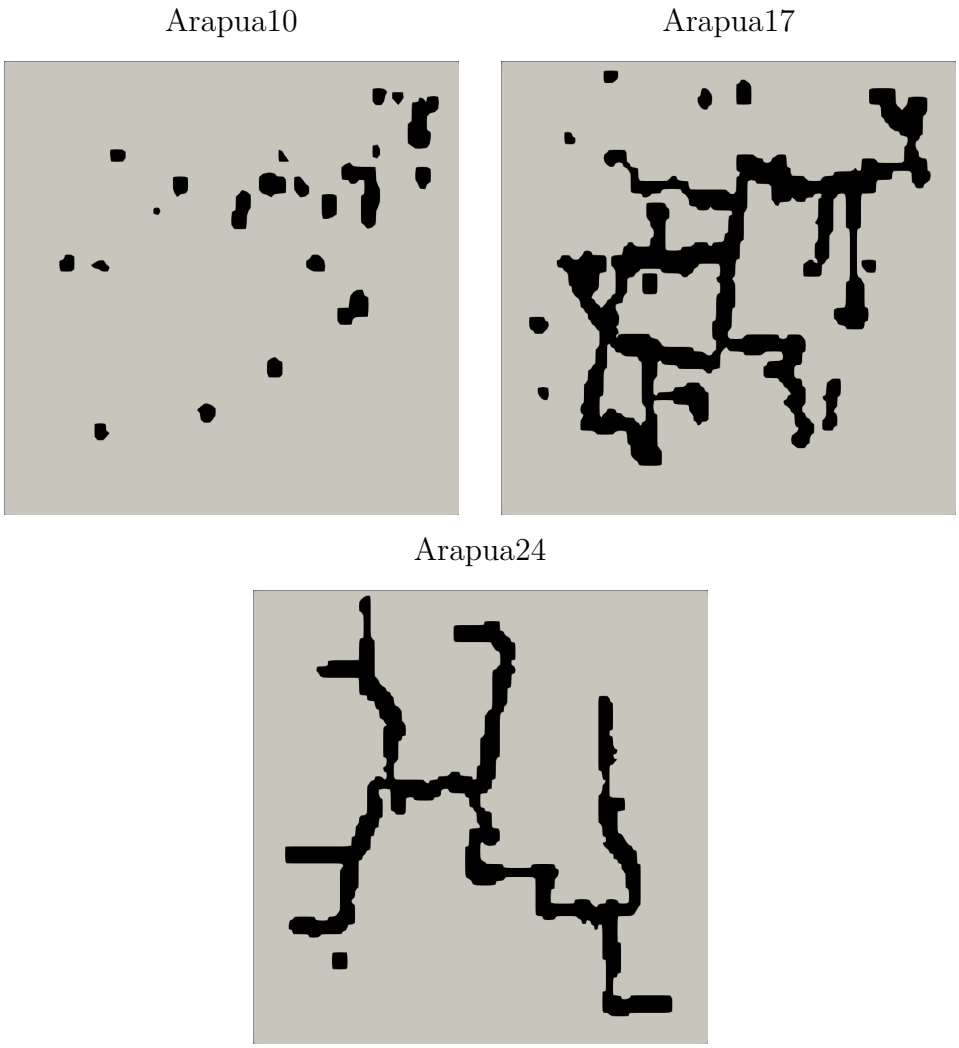

Figure 5.2: The three different vug configuration base on the Lajedo Arapua outcrop (Arapua10, Arapua17 and Arapua24) where the geometry and position of Ω_V (black) is varied on the domain and in Ω_M (gray).

and the maximum characteristic length (cl_{max}).

A comparative evaluation between the Brinkman model and the $2\phi 2k$ model is conducted for Arapuá vug configurations. Thus, careful consideration is given to mesh selection. It is intended to ensure that unstructured meshes generated by Gmsh and structured meshes created by IMEX are equivalent. The consistency of meshes across the two solvers is assessed as follows. Based on the constraints imposed by the available computing resources, mesh refinement is evaluated in both scenarios as a potential enhancement to the solution. The FEniCS models are consistently limiting in all cases, since simulations are run on a laptop with a simple configuration, whereas the IMEX software has access to the Petrobras Cluster. As a result, FeniCS mesh selection is performed first. In terms of size, IMEX meshes are comparable to FEniCS meshes. In addition, an investigation is conducted to determine whether mesh refinement

				Number of Elements		
Mesh	cl_1 (m)	cl_2 (m)	cl_{max}(m)	Arapua10	Arapua17	Arapua24
Mesh a	0.100	0.100	0.100	1,424	2,144	1,480
Mesh b	0.060	0.060	0.060	3,730	5,080	2,824
Mesh c	0.030	0.030	0.030	14,210	18,116	14,446
Mesh d	0.017	0.017	0.017	43,932	52,034	44,082
Mesh e	0.015	0.015	0.015	56,086	75,280	56,508
Mesh f	0.100	0.015	0.100	2,218	23,136	19,770
Mesh g	0.050	0.015	0.050	5,978	27,136	24,634

Table 5.2: Mesh parameters used for the mesh test in the Arapua configurations.

in IMEX would lead to improved results. When mesh refinement is applied to simulations conducted in IMEX, no significant improvements in solution quality are observed. Alternatively, coarsening meshes, known as upgriding, is not considered. This approach is frequently used in upscaling studies, but is intentionally omitted in this study. Two-phase flow can be significantly affected by scale transformation when meshes are coarser. Consequently, this aspect of the study has been excluded. Due to this, both fine and coarse scales exhibit the same mesh size.

The mesh quality is assessed by comparing the area of triangular mesh elements with that of IMEX's structured mesh elements. Each square within the IMEX grid has a 0.01 m length, i.e., each dimension of equation (3-111) (L_x, L_y, and L_z) has a 0.01 m length.

Figure 5.3 represents the W_{cut} variation as function of t_D for the three Arapuá cases for seven mesh configurations. For the Arapua17 and Arapua24 scenarios, Mesh-g is selected. In the Arapua10 scenario, Mesh-d is selected. Compared to Mesh-e, the numerical solution differed only marginally, but the computation cost is significantly increased.

Figures 5.4, 5.5, and 5.6 show the selected meshes for the Arapua10, Arapua17 and Arapua24 vug configurations, respectively. The primary difference between these cases lies in the porous matrix discretization. In Arapua10 the vugs are sparsely distributed across the porous matrix and occupy less area than in the other cases. So cl_1 and cl_{max} have a bigger impact than cl_2. Comparing Mesh-g and Mesh-f, when cl_1 and cl_{max} are modified, the number of elements are increased significantly. The porous matrix contains more elements, causing this difference in element counts. Conversely, in the Arapua17 and Arapua24 configurations, the cl_2 parameter is the dominant factor in de-

	Arapua10		Arapua17		Arapua24	
Mesh	Δt (s)	C.T (s)	Δt (s)	C.T (s)	Δt (s)	C.T (s)
Mesh-a	200	2.3×10^3	100	3.7×10^3	100	3.9×10^3
Mesh-b	200	9.4×10^3	100	1.4×10^3	100	1.6×10^4
Mesh-c	200	7.9×10^4	100	1.1×10^5	100	1.3×10^5
Mesh-d	200	1.8×10^5	100	1.3×10^6	100	6.2×10^5
Mesh-e	100	7.2×10^5	100	2.6×10^6	100	1.2×10^6
Mesh-f	200	2.1×10^3	100	1.7×10^5	100	1.2×10^5
Mesh-g	200	9.6×10^3	100	2.4×10^5	100	1.6×10^5

Table 5.3: Computational times (C.T) and the Δt used on the Arapuá vug configurations.

termining the mesh structure. The mesh inside the vug and near the porous matrix is controlled by this parameter. Therefore, the porous matrix regions bordering the vugs are also refined. Due to the extensive area of the vug region adjacent to the porous matrix, it significantly influences mesh generation within the matrix. This is evident in Figures 5.5 and 5.6. In these situations, cl_1 and cl_{max} primarily affect regions near model boundaries.

On the IMEX, all meshes are structured square meshes with uniform edge dimensions. The IMEX program generates these meshes based on parameters defining the number of cells in each direction as well as the size of the edges. In the Lajedo Arapuá cases, the mesh has Nx = 232, Ny = 206, and Nz = 1, with an edge size of 0.01 m. Figure 5.7 shows the mesh generated by IMEX for the porous matrix. Figure 5.8 illustrates the meshes in the homogeneous $2\phi2k$ fracture grid model. All three Lajedo Arapuá scenarios use the same mesh.

IMEX models use different boundary conditions when compared to those employed in the Brinkman and Darcy models developed with the FEM using the Dolfin library. IMEX directly imposes impermeable conditions on all boundaries, with mass exchange occurring through well-surface coupling. In essence, to emulate the inlet condition at Γ_1 and the outlet condition at Γ_2, a producer well and an injector well are used, respectively.

These differences result in variations between the results obtained from the finite element models and those generated by IMEX. Primarily, these discrepancies arise because the well is coupled to the center of each cell, leading to inaccuracies. To mitigate these differences, it is employed refined meshes on the wells. It is advisable to refine the mesh within the edge cell that contains the well and move the well to the refined cell at the model boundary. This

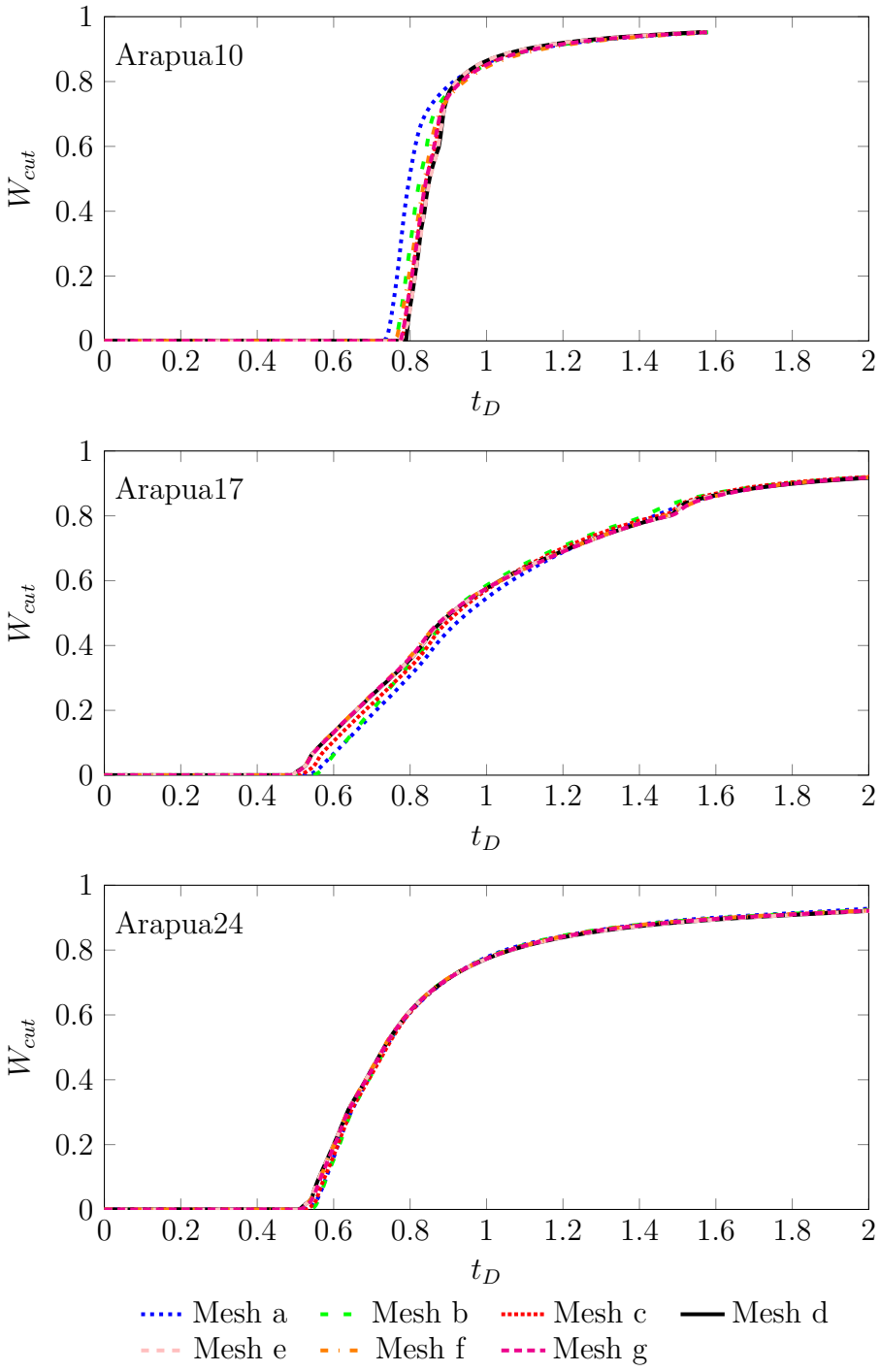

Figure 5.3: Analyses of mesh impact on Lajedo Arapuá cases. It is presented the influence of mesh refinement on W_{cut} as a function of t_D.

approach is implemented in this study, as illustrated in figure 5.7. It can be seen in figure 5.7 that the first cell is subdivided five times in the direction of the flow (horizontal direction). Another good practice used here is to set a high permeability value in the cells containing the wells. This is done to ensure uniform injection. In this study, these cells have 10 D of absolute permeability. On both the matrix grid and fracture grid, this procedure is

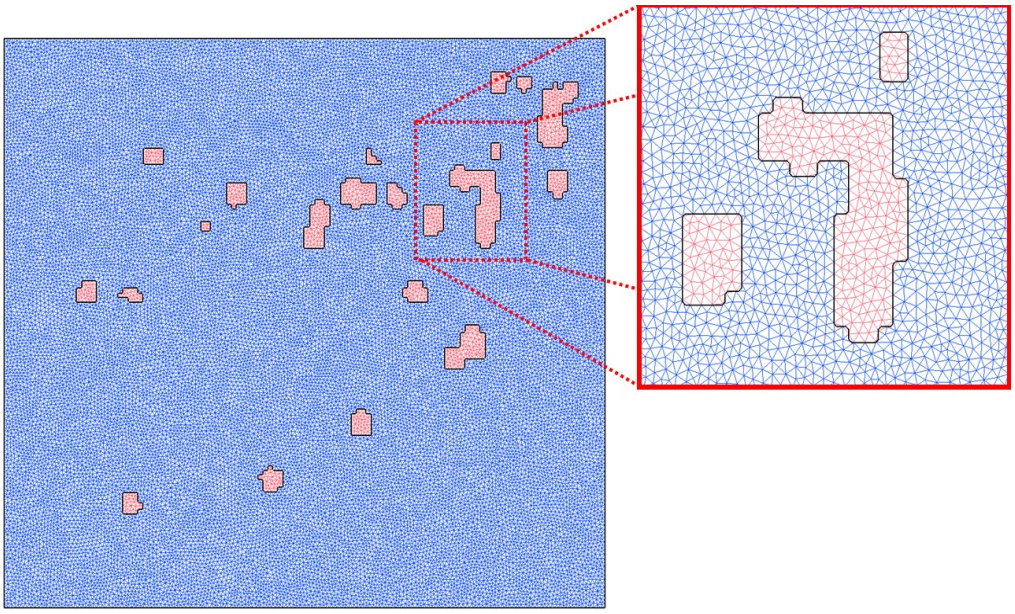

Figure 5.4: Mesh of the Arapua10 vug configuration (mesh d).

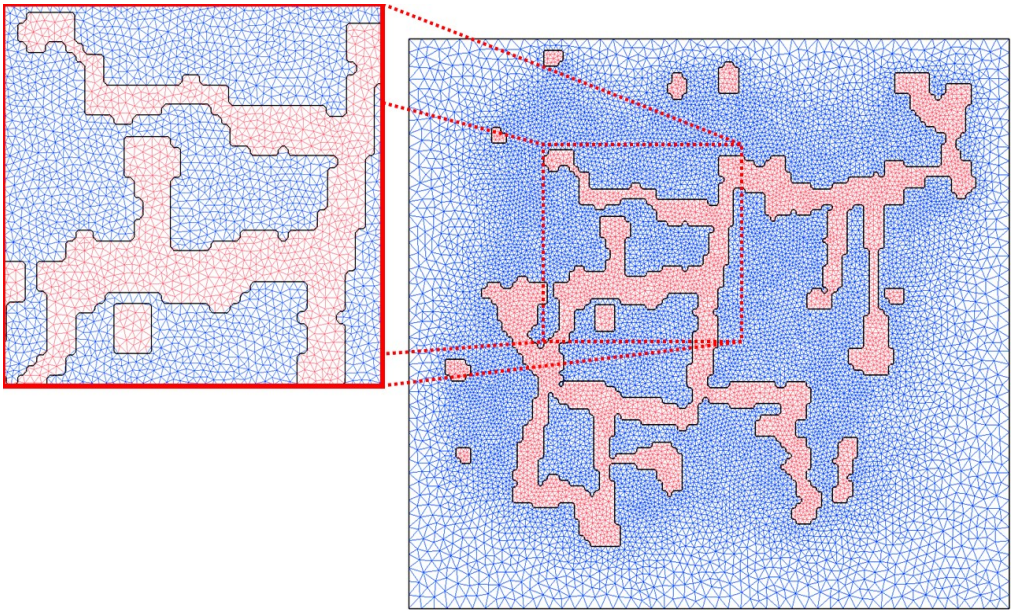

Figure 5.5: Mesh of the Arapua17 vug configuration (mesh g).

conducted. Additionally, in the $2\phi 2k$ model, the wells are opened to flow in for the fracture grid and the matrix grid. As result the mesh configuration, σ is calculated by the (3-111), where L_x, L_y, and L_z has a 0.01 m length. Thus, the base case value for σ is equal to 1.2 $\times 10^5$ m^{-2}. Due to its low sensitivity in this study, sigma remains unchanged during the upscaling process. This is discussed in section 5.3.3, where the sensitivity of this parameter is examined.

In equation (3-86), the γ parameter can be affected by the mesh. Therefore, the same evaluation as in chapter 4 is repeated. This chapter

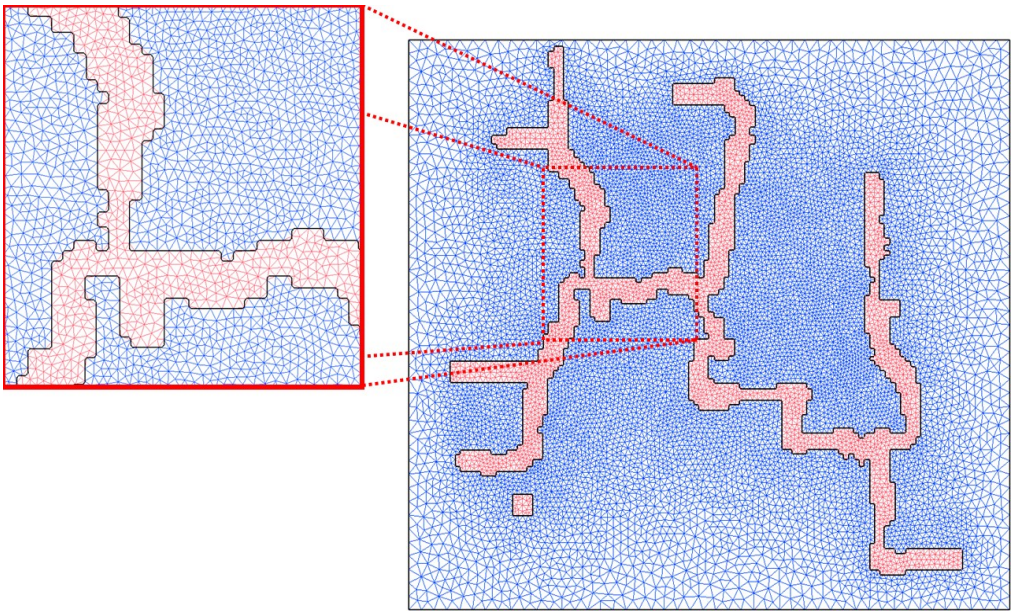

Figure 5.6: Mesh of the Arapua24 vug configuration (mesh g).

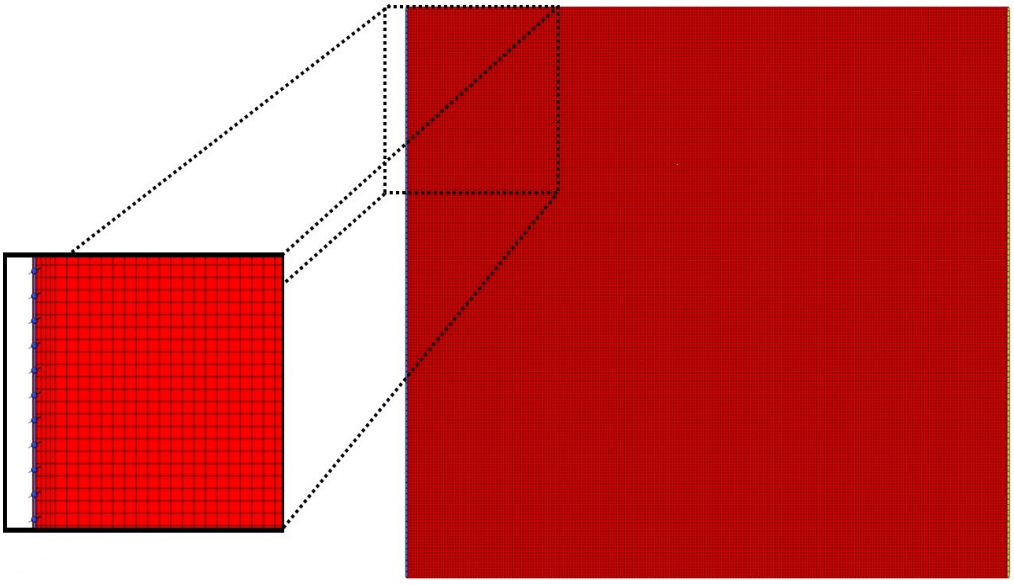

Figure 5.7: Porous matrix or matrix grid mesh configuration. This mesh configuration is used for homogeneous $2\phi 2k$ model. It is created by IMEX software. Their differences are primarily the size of the domain and the number of cells.

presents the computations for Arapua17 with γ varied according to table 5.4. As before, the results of the sensitive analysis to this parameter indicate that it has negligible impact on the results. As an example, the relative difference in permeability between $\gamma = 1$ and $\gamma = 35$, for example, is 6.59×10^{-9}. Therefore, throughout this chapter $\gamma = 35$ is assumed.

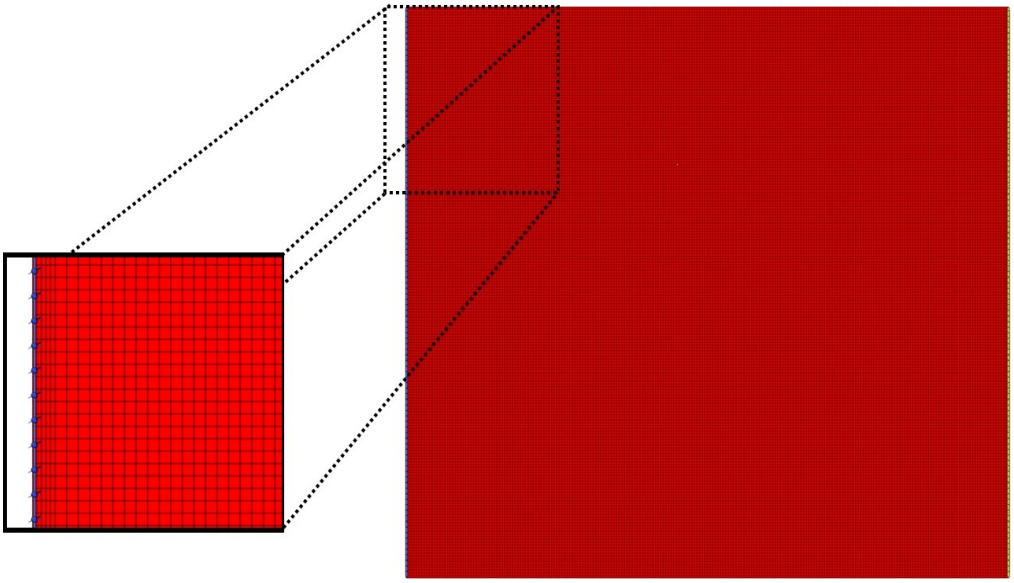

Figure 5.8: Here is an illustration of the mesh generated by IMEX for the analysis of Arapuá scenarios. It represents the fracture grid of the homogeneous $2\phi 2k$ model and is used for the three Arapuá scenarios.

γ	K [mD]
1	311.212
10	311.212
35	311.212
100	311.212

Table 5.4: The influence of γ on the absolute permeability of the Arapua17 vug configuration.

5.3 Arapuá Results

This section presents the results of the analysis conducted to determine the equivalent absolute permeability and the equivalent relative permeability curves for the homogeneous $2\phi 2k$ Darcy model using the Arapuá vug configurations (section 5.1). Absolute permeability for the fracture grid is deduced based on the single-phase steady state Brinkman model. Subsequently, a comparative analysis is carried out between the Brinkman model and the homogeneous $2\phi 2k$ Darcy model in the context of two-phase flow. The generation of equivalent porous media for the Arapuá models is accomplished through the use of equivalent absolute permeability and equivalent relative permeability curves. Additionally, the impact of shape factor on the generation of these equivalent porous media is assessed. Finally, it is investigated the influence of viscosity on equivalent relative permeability curves.

5.3.1 Single-Phase Flow

Figure 5.9, 5.10, and 5.11 present the steady-state, single-phase flow velocity magnitude field predicted by the Brinkman model across the three Arapuá vug configurations. The velocity profile along the cuts CC and DD is also presented in the figures. A distinct disparity is evident in the velocity profile of the Arapua10 case when compared to other cases. In this sample, the vugs are dispersed within the porous matrix and compose a relatively minor portion of the total porous volume, which results in less pronounced variations in the velocity field. Notably, the most significant variations in velocity are observed at the interfaces between vugs and porous matrix. Similar phenomena have been observed in synthetic vugs (section 4.4.1). Velocity differences can be as large as five orders of magnitude. In the Arapua17 and Arapua24 scenarios, it becomes evident that the velocity is significantly reduced in the central region of the porous matrix surrounded by fractures. In contrast, vugs are characterized by high velocity areas. Essentially, the predominant fluid flow between Γ_1 and Γ_2 occurs within the vugs. Based on the velocity data, the Reynolds number can be estimated in order to determine whether the simplifying assumptions are valid. Based on water properties at standard temperature, the Reynolds is 6.4 $\times 10^{-1}$ Arapua24 vug configuration. Thus, it is possible to consider that the hypotheses are valid.

Figures 5.12, 5.13, and 5.14 show the steady-state, single-phase flow pressure distribution across the three Arapuá scenarios. The pressure along the lenght (cut CC) is also shown. In Arapua10, vugs have a limited impact on the pressure gradient. The gradient in this scenario is similar to the pressure gradient in a porous matrix and it is only slightly distorted by the vugs. For Arapua17 and Arapua24, the vugs and fractures significantly influence the pressure gradient. It is particularly evident in the central regions of these cases. Within the central porous matrix regions of these domains, the pressure gradient is similarly low. Consequently, consistent with the velocity analysis of these regions, it is evident that these areas make a limited contribution to overall flow dynamics. As a result, the vug regions emerge as the dominant pathways for flow in these vuggy porous media configurations.

Figure 5.15 shows the relative difference between the equivalent permeability obtained from the homogeneous $2\phi 2k$ model and that derived from the Brinkman model ($K^{eq}_{1\phi 1k}$) as function to the fracture grid permeability (K^f). The equivalent permeability of the $2\phi 2k$ model on the coarse scale ($K^{eq}_{2\phi 2k}$) is a function of the relationship between K^f and K^m. The assumption of a sufficiently high absolute permeability value in the vuggy region leads to misrepre-

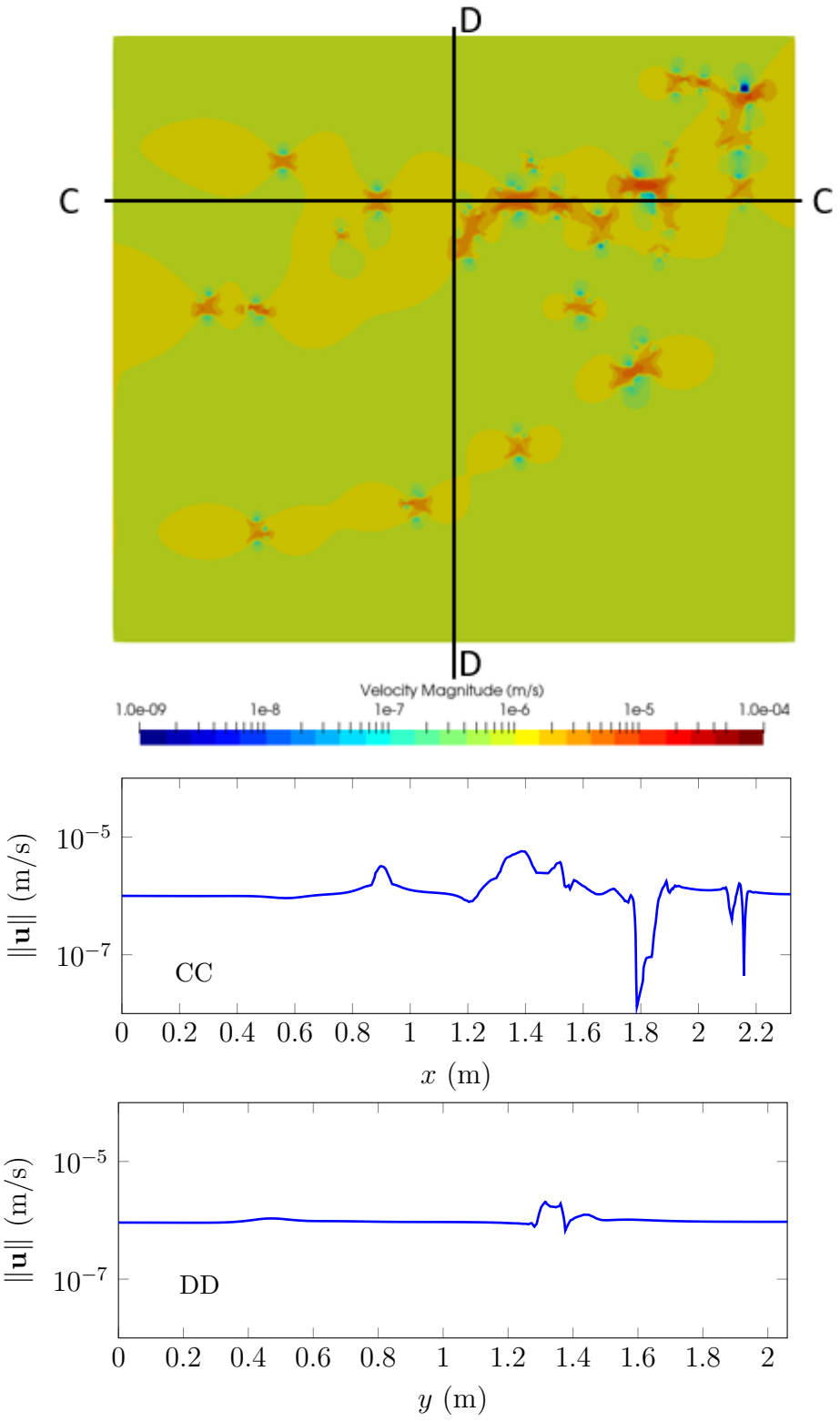

Figure 5.9: Velocity magnitude field (m/s) on the single-phase steady-state regime for the vug configuration Arapua10. It is presented the velocity profile on cuts CC and DD.

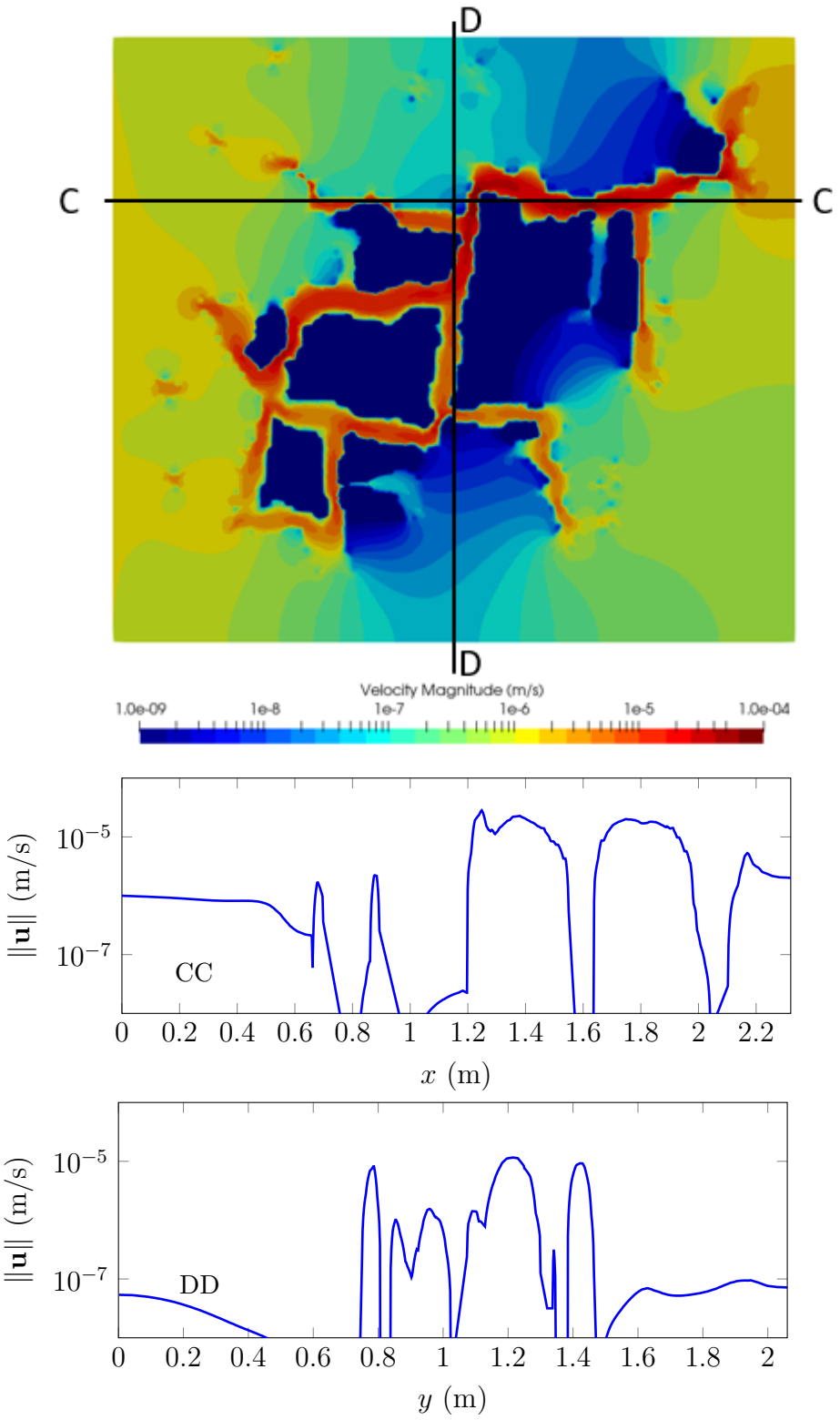

Figure 5.10: Velocity magnitude field (m/s) on the single-phase steady-state regime for the vug configuration Arapua17. It is presented the velocity profile on cuts CC and DD.

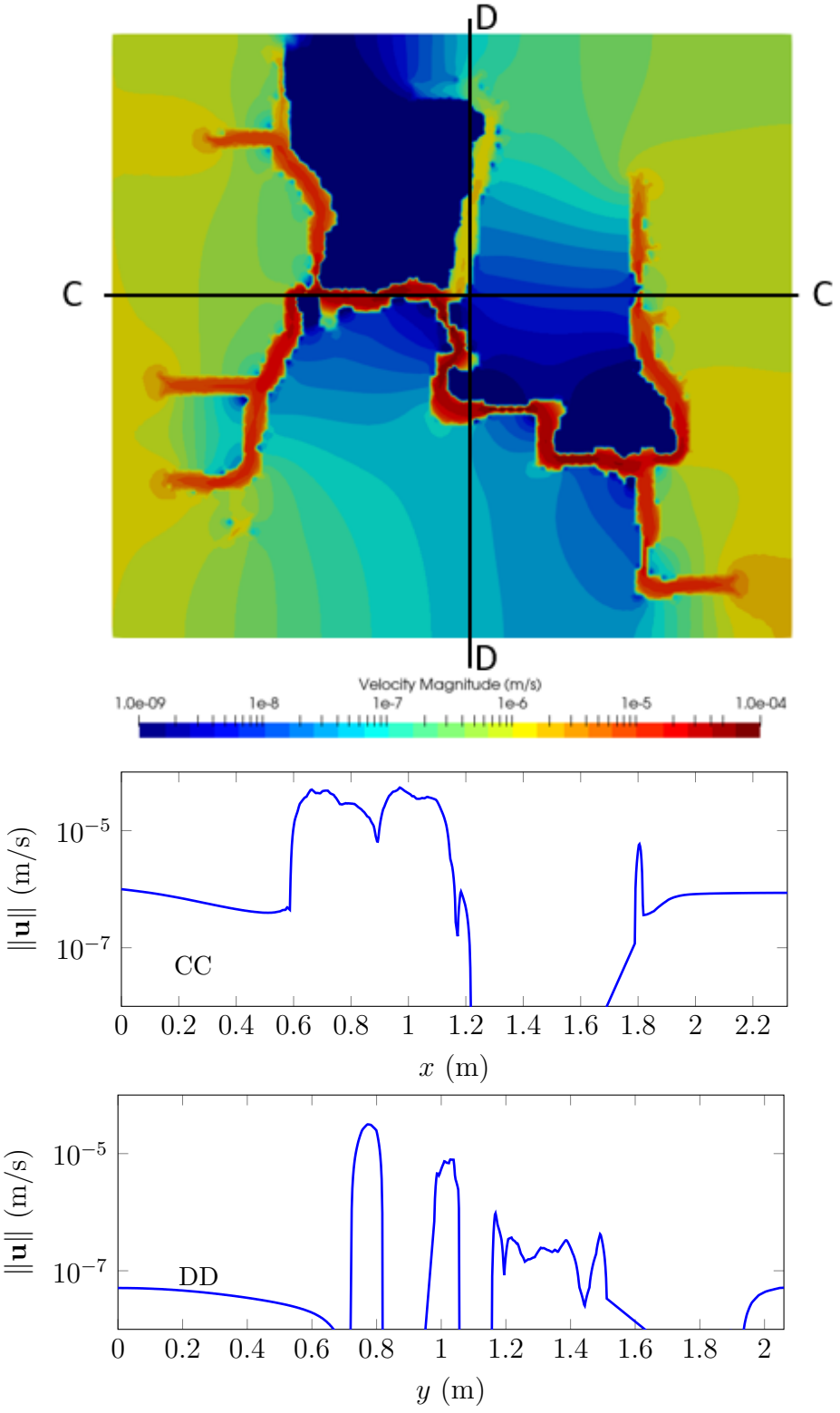

Figure 5.11: Velocity magnitude field (m/s) on the single-phase steady-state regime for the vug configuration Arapua24. It is presented the velocity profile on cuts CC and DD.

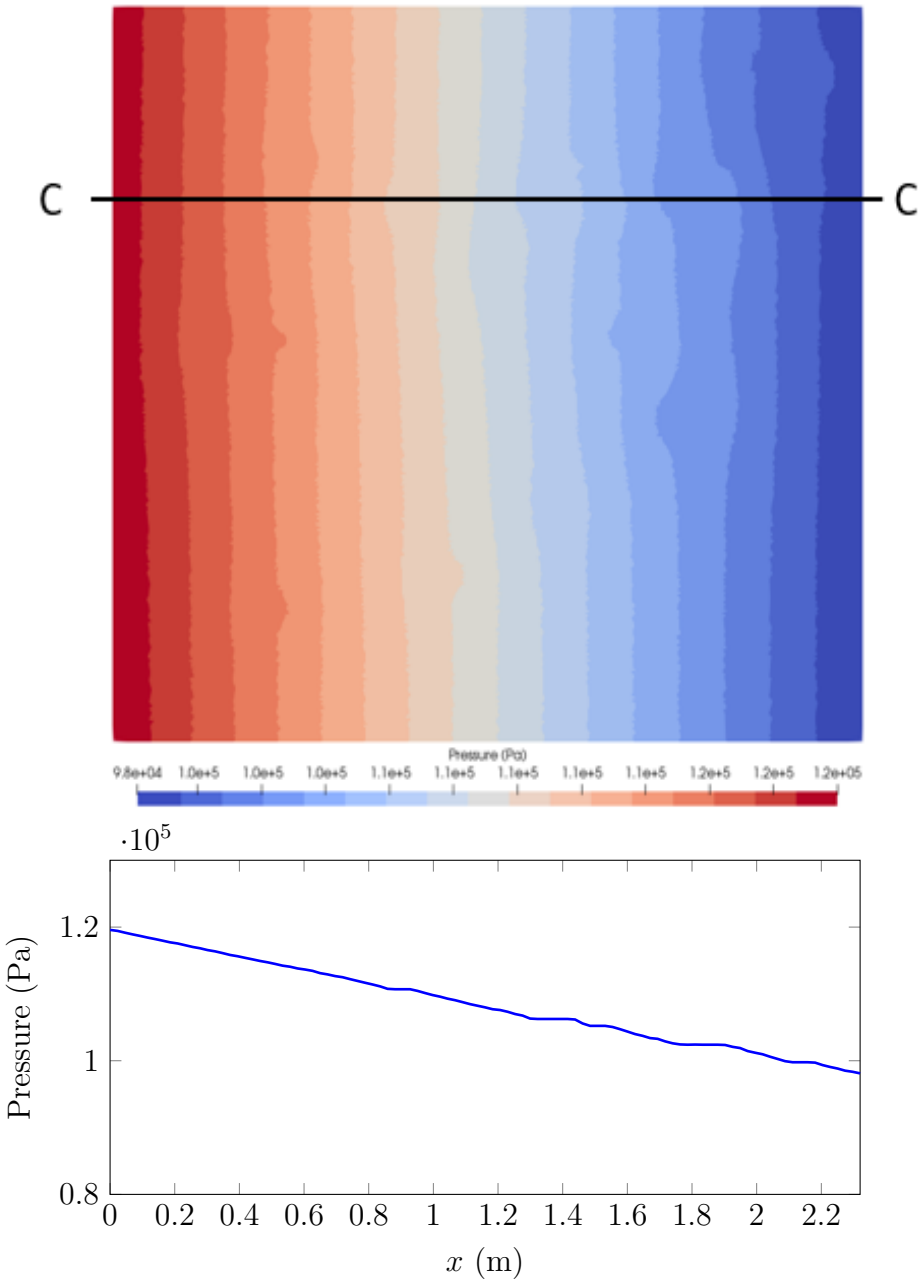

Figure 5.12: Pressure (Pa) field on the single-phase steady-state regime for the vug configuration Arapua10 using the Brinkman model. It is presented the pressure profile on section CC.

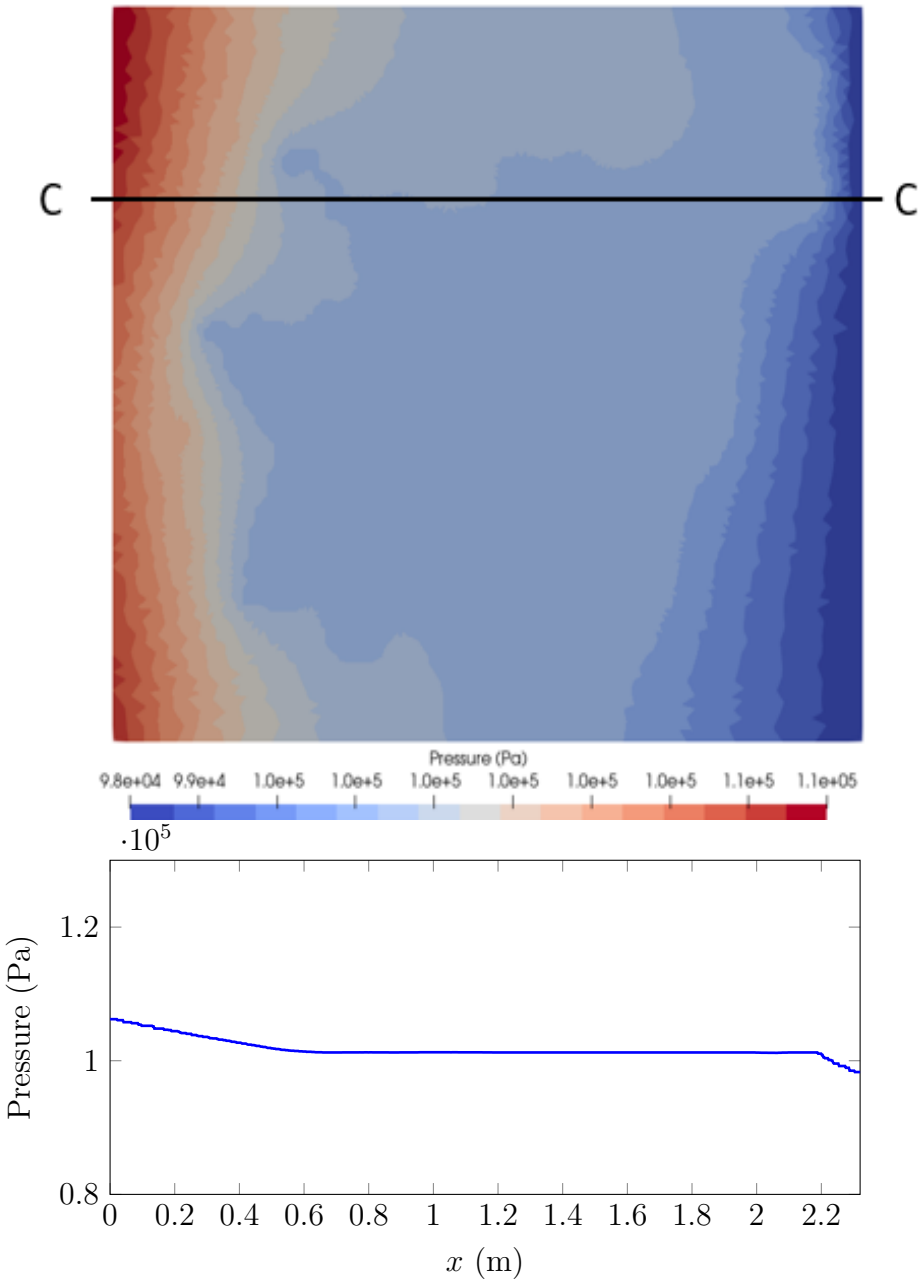

Figure 5.13: Pressure (Pa) field on the single-phase steady-state regime for the vug configuration Arapua17 using the Brinkman model. It is presented the pressure profile on section CC.

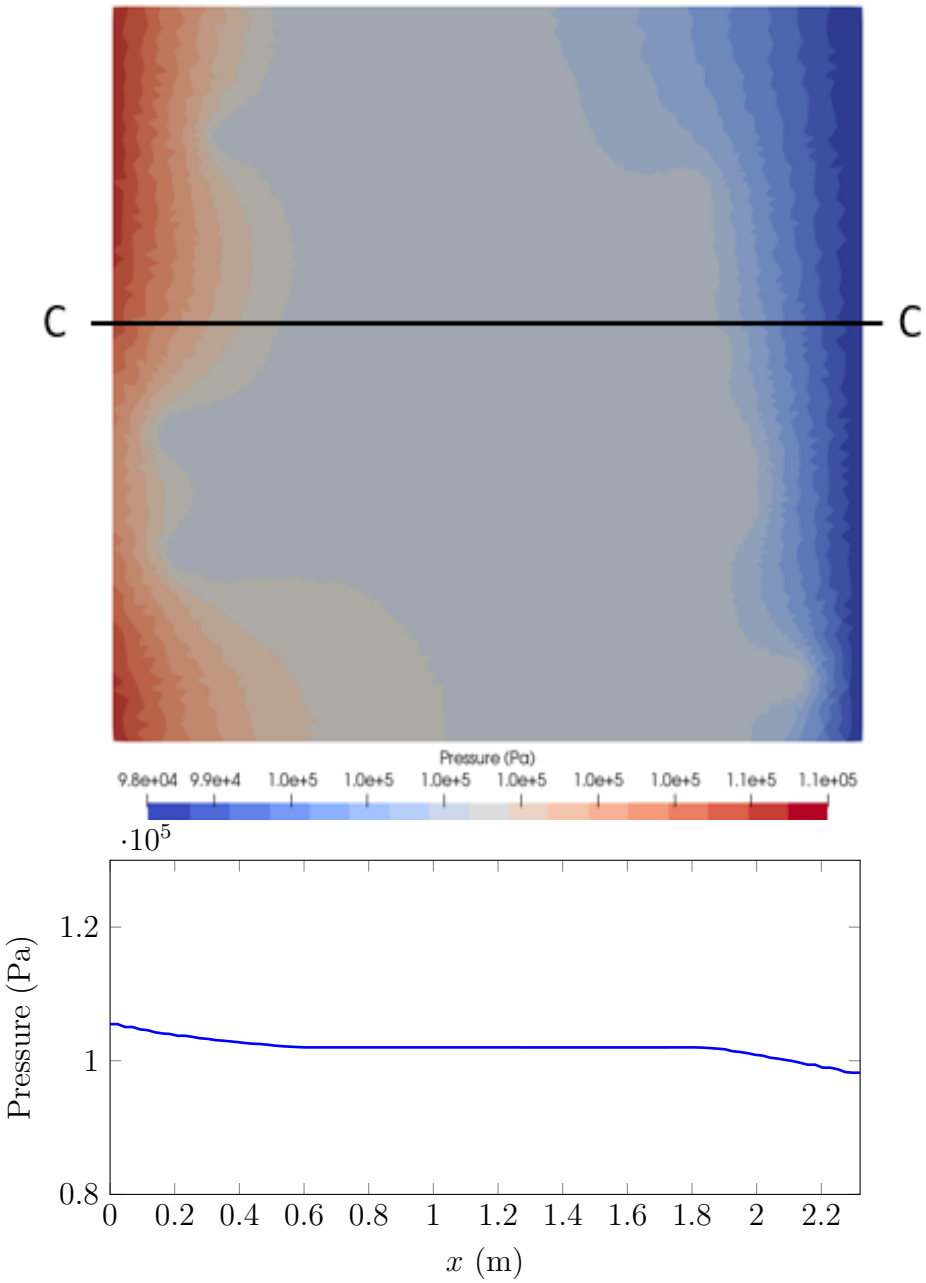

Figure 5.14: Pressure (Pa) field on the single-phase steady-state regime for the vug configuration Arapua24 using the Brinkman model. It is presented the pressure profile on section CC.

sentation of fluid flow, as shown in section (4.4.1). Notably, for each scenario, there is a distinct value of K^f that minimizes error. The optimal K^f value for each Arapuá scenario is presented in Table (5.5). K^f is a critical factor for the homogeneous $2\phi2k$ model. An arbitrary selection of these parameters can lead to inaccuracies when establishing equivalent permeability. This model is highly sensitive to fracture permeability variations.

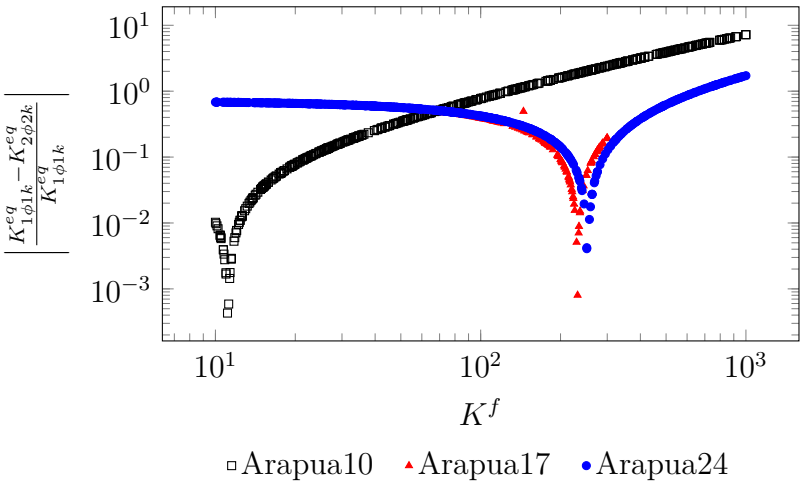

Figure 5.15: An analysis of the relative error between the single-phase steady state flow obtained by the Brinkman model and the homogeneous $2\phi2k$ Darcy model for Arapua10, Arapua17, and Arapua24 vug configurations as a function of fracture permeability (K^f).

Arapua10 configuration is characterized by a dispersed and poorly interconnected vug configuration. Consequently, this vug configuration exhibits a notably lower value of K^f than other scenarios. Furthermore, K^f is much lower than the absolute permeability of the porous matrix. According to Barenblatt et al., (1960) [19], fracture absolute permeability should be higher than porous matrix absolute permeability. However, Arapua10 fails to meet this criteria. In this case, the porous matrix dominates the fluid flow. As a result, the fracture/vug flow becomes negligible. Consequently, employing the $2\phi2k$ model under such conditions is not recommended.

On the other hand, Arapua17 and Arapua24 configurations present high K^f values compared with K^m. The cause of this is the conduit-type macroporosity. In this scenarios, the optimum value of K^f is approximately twice as high as matrix absolute permeability. This substantial difference emphasizes the influential contribution made by flow through fractures, thus supporting the adoption of a dual continuum model.

Sample	V_V $[m^3]$	V_m $[m^3]$	$K^{eq}_{1\phi 1k}$ [mD]	K^f [mD]
Arapua10	0.18	0.96	108.98	11.11
Arapua17	0.78	0.79	311.21	231.97
Arapua24	0.55	0.85	322.68	251.24

Table 5.5: Properties for Arapua10, Arapua17, and Arapua24: porous volume for matrix and vug domain, absolute permeability obtained through the Brinkman model ($K^{eq}_{1\phi 1k}$), and optimal fracture absolute permeability (K^f).

5.3.2 Two-Phase Flow

Figures 5.16, 5.17, and 5.18 show the comparative two-phase flow results for the Brinkman model and the homogeneous $2\phi 2k$ Darcy models. There are two cases for the homogeneous $2\phi 2k$ model. In the reference scenario, the absolute permeability is taken from table (5.5) and the relative permeability curve is $\times$ type, where the phase mobility is linearly proportional to the phase saturation. This scenario is chosen because it is common configuration found in literature to model the karst features [108, 62, 110]. The second scenario is after the history matching has been performed. The absolute fracture permeability is obtained from table (5.5) and the equivalent relative permeability curve is obtained through numerical optimization to provide a more accurate representation of the Brinkman results. The results are presented as accumulated oil production (Np_D), water cut (W_{cut}) and the pressure difference (Δp). In dual-continuum models analysis, the pressure difference is not normalized at $t_D = 0$ because at the initial simulation steps in the IMEX simulator, the pressure difference is highly sensitive and fluctuates significantly. It occurs due to pressure equilibrium between the two continuum domains. Consequently, the pressure reference at $t_D = 0$ lacks consistency between the Brinkman model and the $2\phi 2k$ model.

Generally, there are two distinct trends for the reference case in the homogeneous $2\phi 2k$ vug scenarios. For the homogeneous $2\phi 2k$ reference case, there is a relative small discrepancy in terms of Np_D, W_{cut}, and Δp in relation to the Brinkman model for the Arapua10 vug case, while the other two cases differ significantly. In Arapua10 configuration, the porous matrix significantly influences flow behavior due to the diffuse vug configuration. Since fracture permeability is significantly lower than matrix permeability and fracture porous volume is much smaller than the porous matrix, fluid flow is dominated by matrix flow.

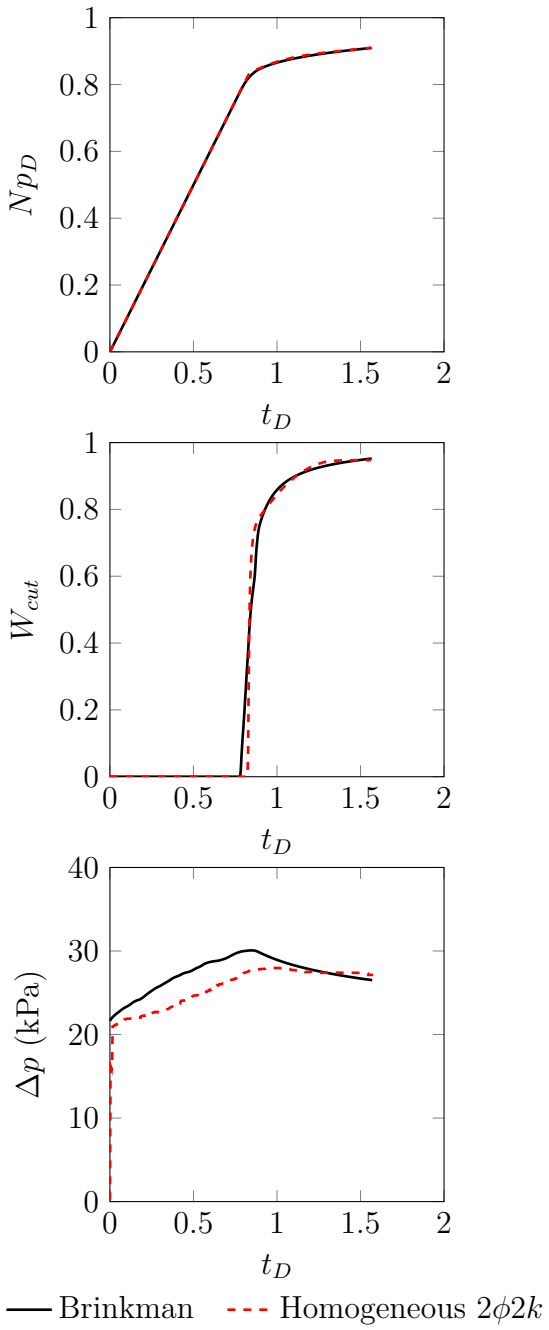

Figure 5.16: It is presented here the Np_D, W_{cut}, and Δp as function of t_D for Brinkman model and the reference homogeneous $2\phi 2k$ Darcy model for the Arapua10 scenario.

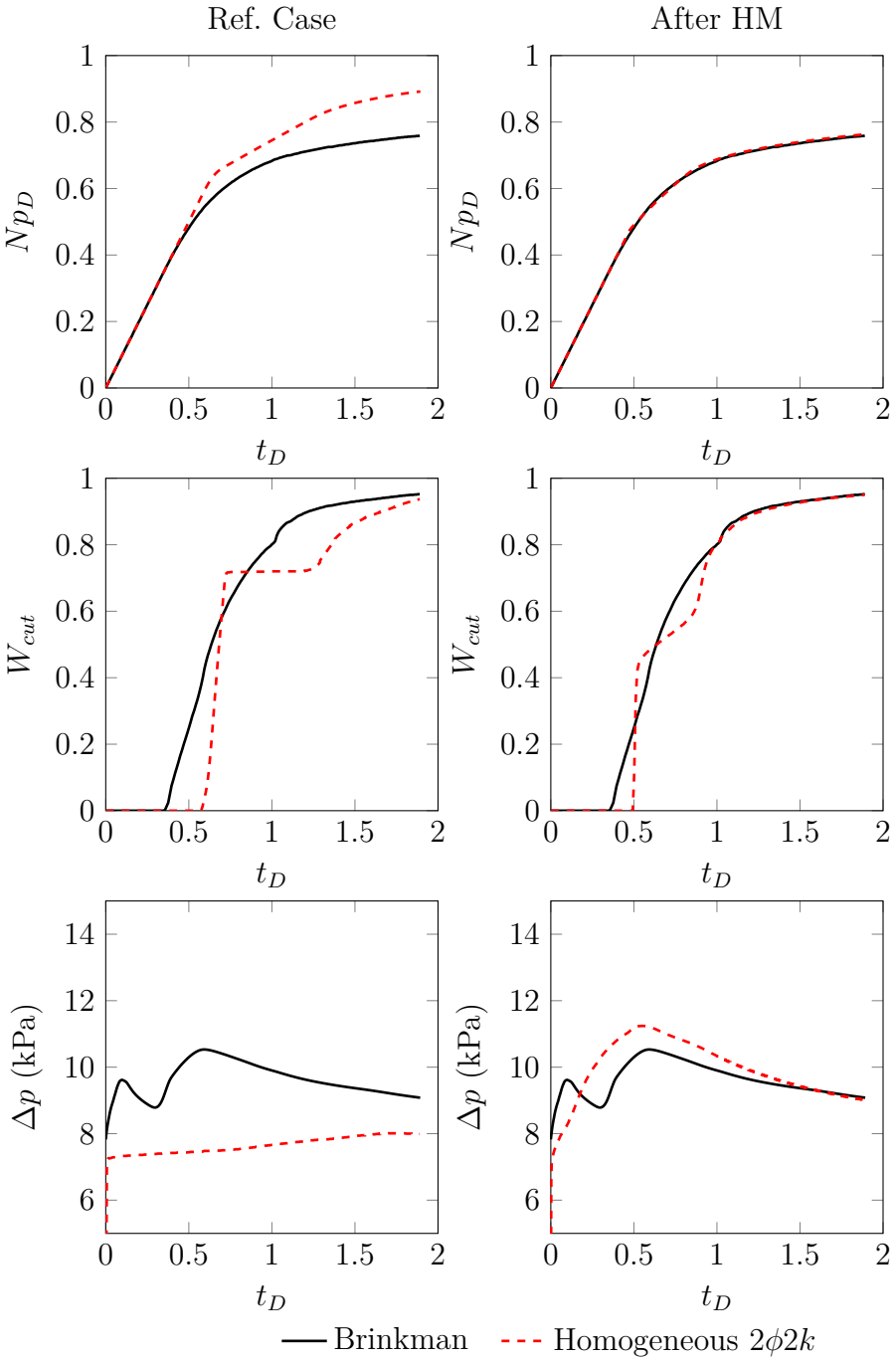

Figure 5.17: It is presented the Np_D and W_{cut} as function of t_D for Brinkman model and the homogeneous $2\phi 2k$ model for the Arapua17 scenario. It is shown the results of the reference scenario and the modification of the curves of relative permeability using the History Matching method.

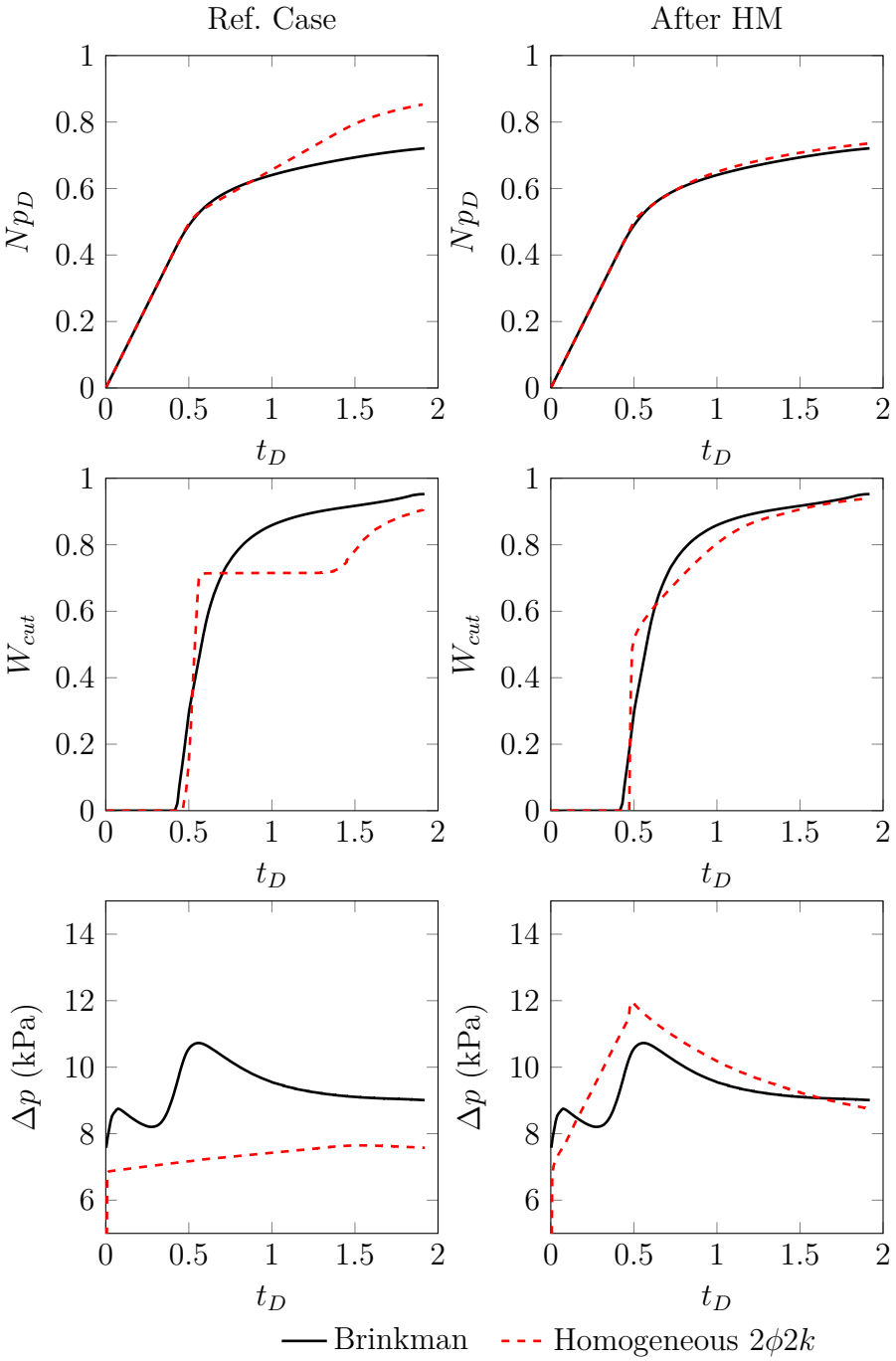

Figure 5.18: It is presented the Np_D, W_{cut}. and Δp as function of t_D for Brinkman model and the homogeneous $2\phi 2k$ model for the Arapua24 scenario. It is shown the results of the reference scenario and the modification of the curves of relative permeability using the History Matching method.

Arapua17 and Arapua24 scenarios exhibit substantial differences in terms of cumulative oil production, water cut evolution and the pressure difference between the Brinkman and the reference $2\phi2k$ homogeneous Darcy model. Comparing the both models, there are significant discrepancies in Np_D final recovery, with deviations of 14.89 % and 15.97 %, respectively. The discrepancies are even more pronounced in W_{cut}, indicating that the modeling approach fails to adequately capture fluid flow behavior. Also, the outcomes differ significantly in terms of Δp.

Np_D, W_{cut} and Δp predictions are significantly improved when History Matching is applied to the Arapua17 and Arapua24 scenarios. Figures 5.17 and 5.18 demonstrate how the optimized relative permeability curves of the fracture grid improves the Np_D, W_{cut} and Δp predictions. In the Arapua17 scenario the discrepancy compared to the Brinkman model or the Np_D final recovery decreased from 17.49 % on the reference scenario to 0.52 % in the case after the HM. For the Arapua24 scenario there is a reduction from 18.30 % on the reference scenario to 2.00 % in the case after the HM. History matching also improved W_{cut} and Δp prediction. Despite the discrepancy between the Brinkman model and the homogeneous $2\phi2k$ model for the Arapua17 and Arapua24 scenarios, W_{cut} and Δp disparity are within an acceptable range. An adequate representation of a highly heterogeneous vugular porous medium can be achieved by incorporating a dual-continuum model with equivalent absolute permeability and equivalent relative permeability curves for the fracture grid.

Figures 5.19, 5.20, and 5.21 display the saturation distribution for the Arapua10, Arapua17, and Arapua24 configurations at three distinct t_D values, respectively. Brinkman's model is compared with the homogeneous $2\phi2k$ models after HM. Arapua10 case exhibits a different behavior from the other two cases. Considering that the porous matrix contains dispersed vugs, the porous matrix serves as the primary conduit for fluid flow within the porous medium. The vugs has high permeability and porosity when compared with the the porous matrix, causing smooth distortion of the advancing water front. In the Arapua10 homogeneous $2\phi2k$ model the water advances simultaneous within both the matrix grid and fracture grid, indicating simultaneous breakthroughs in both the porous matrix and fracture network.

Conversely, the flow patterns observed in Arapua17 and Arapua24 are significantly influenced by the interconnected vug system, forming extensive channels throughout the domain. This configuration creates zones of low flow resistance, which serve as preferred pathways for fluid flow. Additionally, after the History Matching process, Arapua17 and Arapua24 exhibit distinct behaviors in the homogeneous $2\phi2k$ model. In these cases, the fracture grid

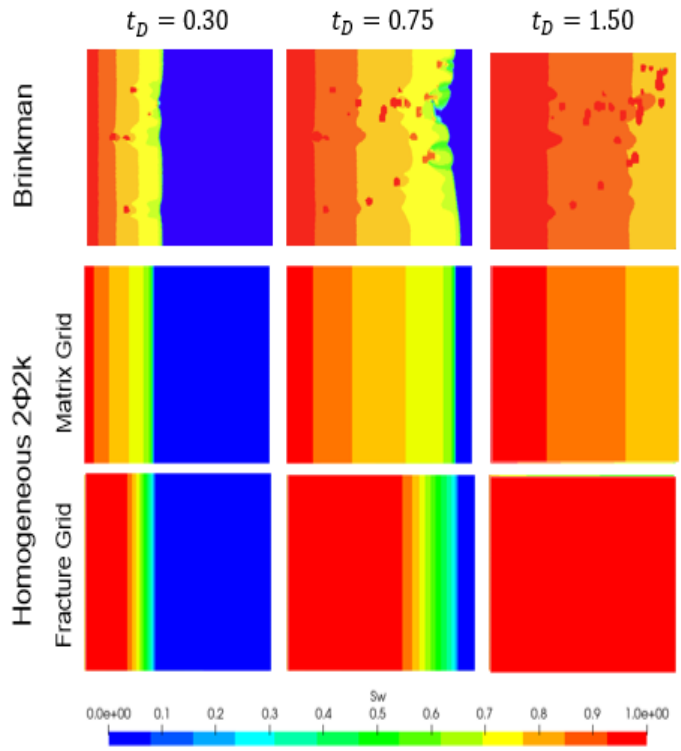

Figure 5.19: Saturation map of the Arapua10 scenario for three different t_D for Brinkman model and the reference homogeneous $2\phi 2k$ Darcy model.

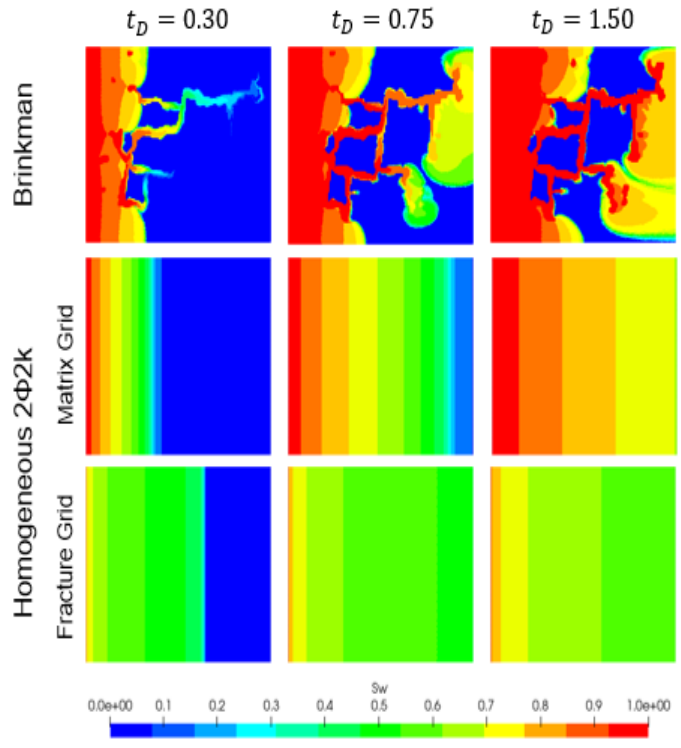

Figure 5.20: Saturation map of the Arapua17 scenario for three different t_D for Brinkman model and the homogeneous $2\phi 2k$ Darcy model after HM.

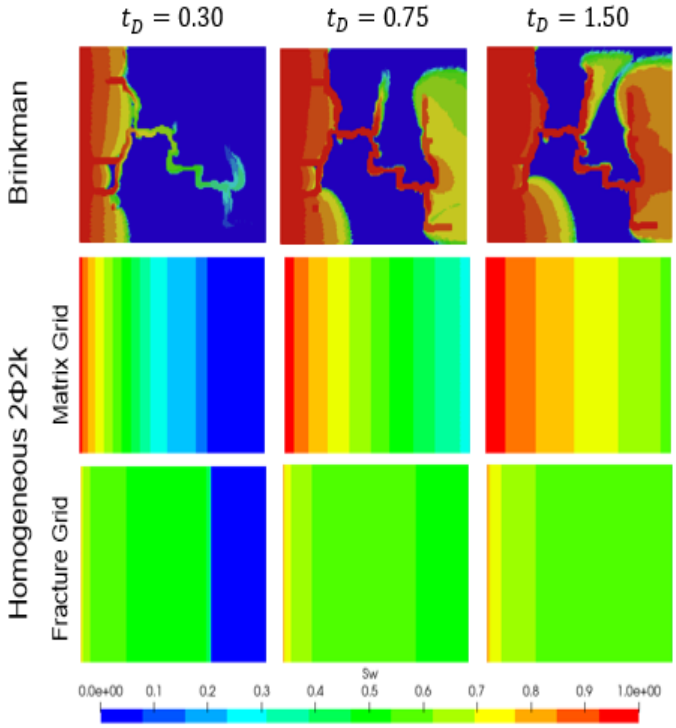

Figure 5.21: Saturation map of the Arapua24 scenario for three different t_D for Brinkman model and the homogeneous $2\phi 2k$ Darcy model after HM.

plays a significant role, resulting in two distinct water-front advancement rates across the porous and fracture grids. Moreover, the saturation distributions differ significantly between these two grids due to variations in their equivalent relative permeability curves. The combination of these factors closely resembles the outcomes predicted by the Brinkman model for two-phase flow.

The homogeneous $2\phi 2k$ Darcy model significantly modifies the computational domain because all the vugular features are replaced for an homogeneous domain. As a result, the equivalent absolute permeability and the equivalent relative permeability curves not only incorporate the viscous diffusivity effects that the Brinkman model incorporates into the model, but also encapsulated the intricate geometry of the vug network.

Figure 5.22 illustrates the equivalent relative permeability curves and the fractional flow after History Matching for the fracture domain. Arapua17 and Arapua24 exhibit different equivalent relative permeability curves for homogeneous $2\phi 2k$ models. This is explained by the fact that both scenarios show differences in macroporosity distribution throughout the domain. Consequently, numerical optimization is required to accurately capture the unique characteristics of each domain. Table (5.6) summarizes the LET parameters for the equivalent relative permeability curves for each geological scenario.

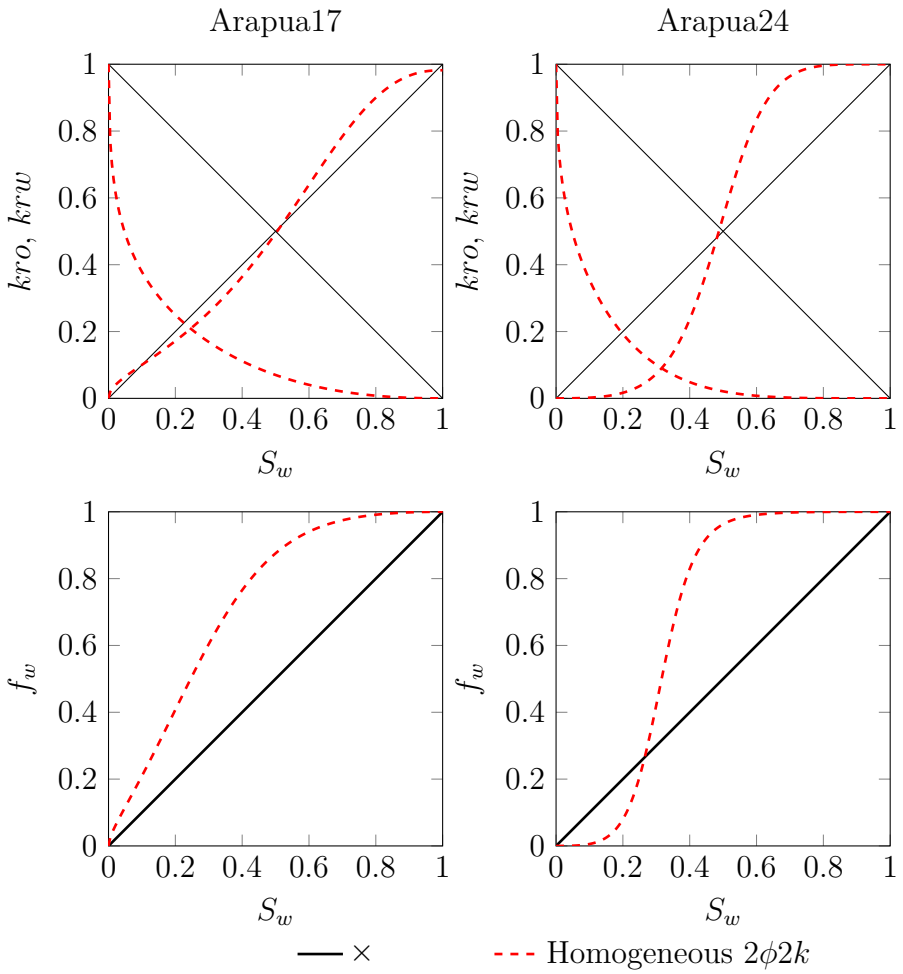

Figure 5.22: The × relative permeability curve and equivalent relative permeability curves and the f_w as function t_D for homogeneous $2\phi 2k$ Darcy model for the Arapua17 and Arapua24 scenario.

5.3.3 Effect of Transfer Function

This section discusses how shape factor affects two-phase flow dynamics. In order to achieve this, σ is varied from 1.2×10^3 to 1.2×10^7 m^{-2} across the three geological configurations in the homogeneous $2\phi 2k$ Darcy models. Each of these sigma values corresponds to the characteristic length in each direction (L_x, L_y, and L_z) multiplied by ten and divided by ten, respectively. The absolute and relative permeability curves of the porous matrix and the fracture domain are kept constant.

Figure 5.23 present the Np_D and the W_{cut} as functions of the t_D for the reference scenario of homogeneous $2\phi 2k$ Darcy models. It is observed that two-phase flow dynamics are not affected by shape factor value. The two-phase flow is only marginally affected by σ the Arapua10 scenario. Therefore, the shape factor has no effect on the two-phase flow and is not considered in further

evaluation.

5.3.4 Effect of viscosity

This section discusses how the oil viscosity affects the determination of fracture equivalent relative permeability curves. Three different viscosity scenarios are tested for the Arapua17 configuration. Oil viscosity is evaluated additionally at 2 cp, 5 cp, and 20 cp, while the water viscosity remains constant at 1 cp. Figure 5.24 illustrates the relation between Np_D as a function of t_D on the reference scenario and after HM for the three viscosity scenarios. As a result of the HM, the homogeneous fracture configuration shows significant improvements. For all viscosity scenarios, figure 5.24 clearly illustrates the enhanced adherence of Np_D from the reference scenario to the after HM case. Each of these case can be quantified by comparing the final recovery Np_D to the Brinkman model. Accordingly, the difference between the Brinkman model from the reference scenario and the after-HM scenario is reduced as follows: from 15.33 % to 2.31 % for μ_o of 2 cp, from 11.70 % to 5.85 % for μ_o of 5 cp, and from 8.37 % to 0.57 % for μ_o of 20 cp.

Configuration	μ_o [cp]	L_o	E_o	T_o	L_w	E_w	T_w	k_{rw}
Arapua24	1.00	4.15	3.72	0.50	2.28	4.19	4.60	1.00
Arapua17	1.00	2.19	4.13	0.50	0.50	3.56	2.35	0.98
Arapua17	2.00	0.50	4.68	1.04	0.50	2.98	1.60	1.00
Arapua17	5.00	1.04	4.33	0.77	0.50	5.00	2.32	1.00
Arapua17	20.00	1.51	4.28	3.08	0.91	1.54	3.20	0.82

Table 5.6: Influence of fluid viscosity and $2\phi 2k$ models on LET parameters for Arupa24 and Arapua17 vug scenarios.

Figure 5.25 illustrates the equivalent relative permeability curves and the fractional flow obtained after history matching for the homogeneous $2\phi 2k$ models. Overall, there is discrepancy between the equivalent relative permeability curves for the viscosity scenarios presented, which are directly related to the fluid viscosity. Table (5.6) presents the LET parameters for the equivalent relative permeability curves associated with the vug configurations of Arapua17 and Arapua24, as well as the homogeneous $2\phi 2k$ models, considering three different values of μ_o. Hence, to define an equivalent porous medium, it is imperative to account for the characteristics of the fluids.

Consistency tests are also conducted for the $2\phi 2k$ models, as explained in chapter four. For these tests, the Arapua24 model is selected, and the inlet

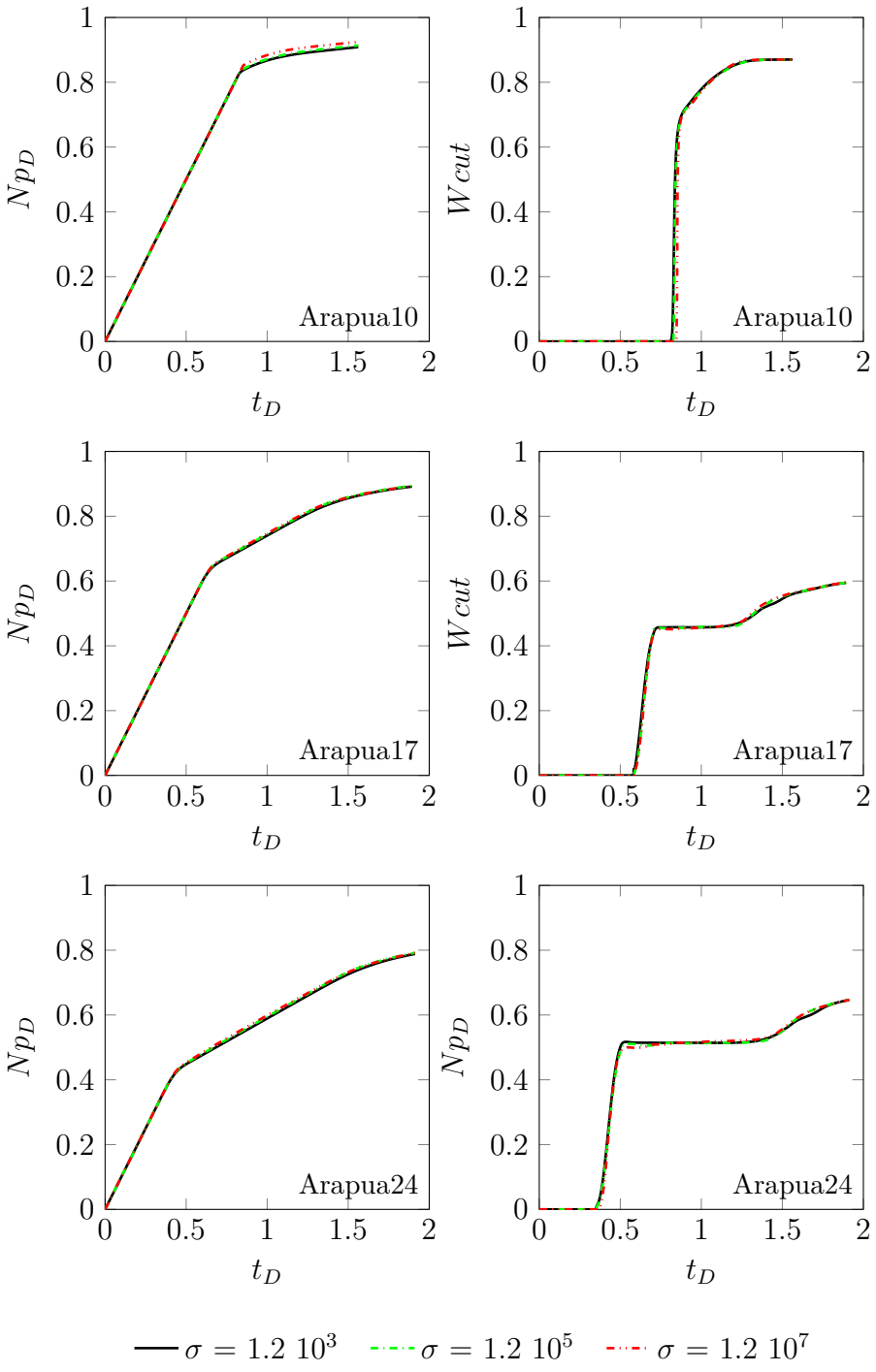

Figure 5.23: An sensitivity analysis of three scenarios of σ is presented for the homogeneous $2\phi 2k$ Darcy model.

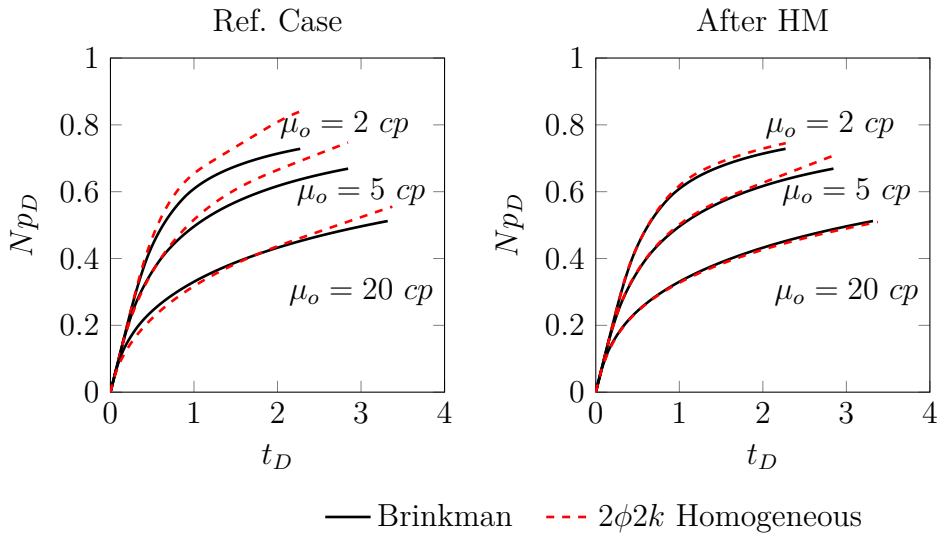

Figure 5.24: Influence of viscosity on Np_D as a function of t_D for the Arapua17 configuration on the homogeneous $2\phi 2k$ Darcy models.

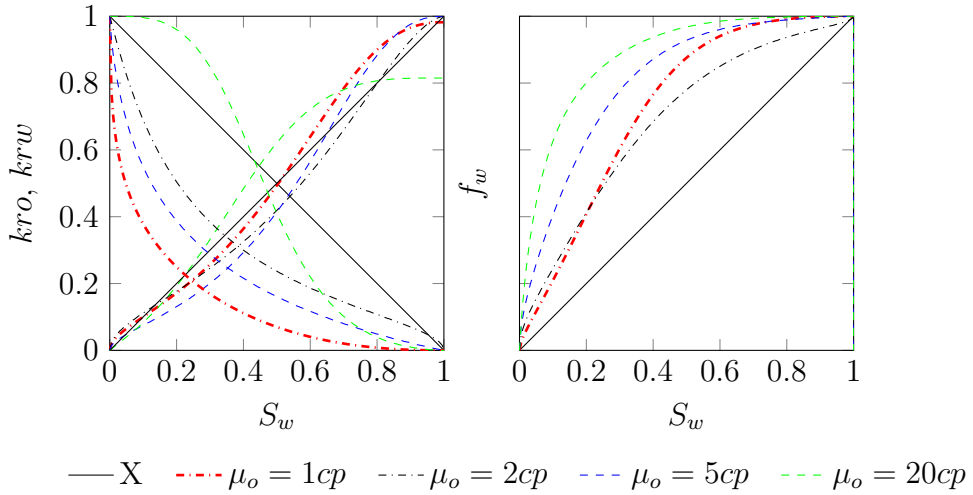

Figure 5.25: The × relative permeability and equivalent relative permeability curves for homogeneous $2\phi 2k$ Darcy model for three different oil viscosity are evaluated at Arapua17 scenario.

velocity is modified to two additional values. It is observed that the W_{cut} and $\frac{\Delta p_{t_D}}{\Delta p_{t_D=0}}$ curves remain unchanged as the inlet velocity varies. This is attributed to the absence of a momentum transport term in the Brinkman equation, which distinguishes it from the Navier-Stokes equation. As a result, disparities caused by varying inlet velocities are small. Hence, no significant alterations in the outcomes are expected due to the velocity variation at the inlet.

In the Arapua24 scenario, the influence of the velocity at the inlet has little effect on the overall result for the establishment of a homogeneous $2\phi 2k$ model. Figure 5.26 presents the fractional flow curves for the fracture, indicating that variations in the LET parameters have little effect on the water

Configuration	$\mathbf{u}_{\Gamma_1}$ [m/s]	L_o	E_o	T_o	L_w	E_w	T_w	k_{rw}
Arapua24	5×10^{-7}	4.43	3.43	0.50	2.24	4.06	4.14	1.00
Arapua24	5×10^{-6}	4.68	3.92	0.53	2.42	4.40	4.68	1.00
Arapua24	10^{-5}	4.53	3.7	0.59	2.49	4.30	4.53	1.00

Table 5.7: Influence of the inlet velocity on Arapua24 $2\phi2k$ models on LET parameters.

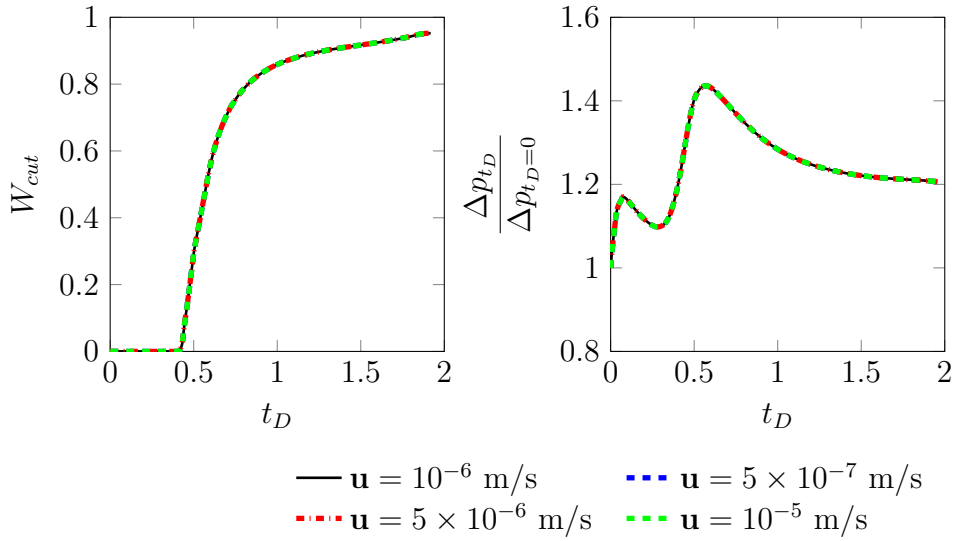

Figure 5.26: For the Brinkman model, an analysis of the influence of inlet velocity is presented on the vug configuration Arapua24.

fractional flow. This can be attributed to the choice of methodology and the low Reynolds number of the flow. Due to the absence of a momentum transport term in the Brinkman equation, as opposed to the Navier-Stokes equation, it appears that the variations resulting from modifing the inlet velocity would be relatively small. The LET parameters responsible for generating these curves are depicted in Table 5.7.

5.4 Discussion

In a manner similar to what has been done here, Campos (2023) [60] compares the Brinkman model with a homogeneous $2\phi2k$ model in single-phase flow. Both studies utilized the same vug geometric system derived from Lajedo Arapuá. Employing an optimization procedure, Campos established equivalent petrophysical properties for the fracture grid. Initially comparing the results derived from the Brinkman models, there was a reasonable agreement on the equivalent permeability between both studies. Regarding the determination of fracture absolute permeability, Campos utilized a porous matrix with 10

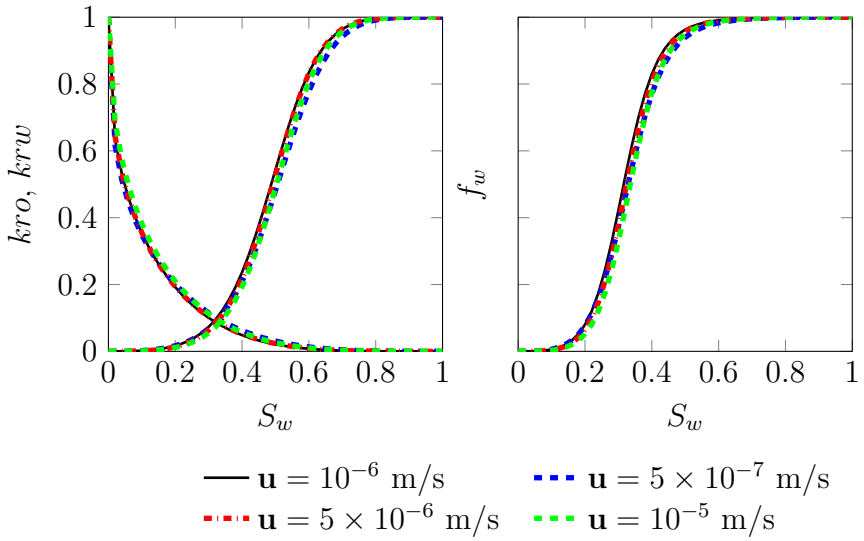

Figure 5.27: A comparison of relative permeability curves and fractional flow under four different inlet velocities for Arapua24 vug configuration on the $2\phi 2k$ homogeneous Darcy model.

mD, differing from this study (100 mD). However, considering the K^f/K^m ratio, both studies yielded similar results. Based on the results of chapter four, it has been demonstrated that the porous matrix affects the pressure drop in the free-flow region and that the relationship between the porous matrix and the vug region remains constant. In a homogeneous model of $2\phi 2k$, where the porous matrix remains constant, and the fracture permeability is numerically calculated, this conclusion of section 4.4.1 can be extended. Both studies have thus reached similar conclusions in terms of establishing equivalent petrophysical properties for a $2\phi 2k$ model.

Campos (2023) [60] presented similar findings to the shape factor sensitivity analysis. The study examined the impact of homogenization on a single-phase transient problem, where σ had negligible influence on calculating equivalent permeabilities in homogeneous scenarios. Similarly, in the current study, this parameter demonstrated no influence on two-phase flow behavior. The shape factor is intricately linked to the numerical mesh configuration. This study does not involve upscaling the grid block (or upgriding), which means there are no modification in the mesh cell dimensions. Therefore, this parameter is not upscaled. In addition, the sensitivity analysis indicates that the numerical solution is not affected by the choice of σ within the established range.

The methodologies presented in this study and those presented in Rios (2020) [90] might be complementary at the reservoir scale. The heterogeneous $1\phi 1k$ model fails to capture the outcomes derived from the Brinkman model, as

discussed in chapters four and five. Thus, even if regions of high flow capacity are approximated at a finer scale in the $2\phi2k$ mode may not accurately reflect flow dynamics in this scale. Thus, it is necessary to use the Brinkman model in the fine scale to correctly model fluid flow. Thus, after using the methodology proposed here, an upscaling can be conducted at the reservoir scale. Thus, it is possible to evaluate flow capacity at a field scale.

Kumar et al. (1997) [80] presents a critical discussion regarding the impact of capillary and gravitational forces on the upscaling procedure. Over chapter four and five, the capillary force is ignored. Thus, the viscous forces is the main drive force in the cases presented here. As evidenced by the findings in Arapua17 and Arapua24, this assumption is suitable because the flow occurs predominantly in the free-flow region. It should be noted that in such instances, minimal flow takes place within the porous matrix. The flow within this matrix is typically directed towards the vug, where the majority of the flow takes place. In the free-flow region, capillary forces are essentially absent. Hence, the viscous forces are predominately over the capillary forces even in scenarios considering capillary forces in the porous matrix. However, for vugs dispersed in porous matrix, such as Arapua10 (or vug configuration (a)-(c), (e) and the micortomography presented in chapter four) it is necessary to evaluate on a case-by-case basis whether these capillary forces modeling may be appropriate for the problem at hand. It is important to take into account gravitational forces, which can be particularly significant in areas of free flow. Particularly important is the establishment of equivalent properties vertically within the reservoir. The omission of this intrinsic physics component must be carefully assessed in order to avoid significant distortions in the application of this methodology. This is one of the limitations of the proposed methodology, which did not considered the gravitational effect. The present study does not address this aspect, however, future research should explore this issue.

The homogeneous $2\phi2k$ Darcy model is a suitable option for homogenizing porous media characterized by substantial channeling effects. As a result of the enhanced degrees of freedom inherent in $2\phi2k$ models, highly intricate media can be homogenized effectively. Combining two distinct porous media creates optimal conditions for the accurate representation of such complex systems. As a result, the modeling approach proposed in this study, which incorporates a $2\phi2k$ model provides a robust alternative for modeling karstified and fractured porous media. Furthermore, its implementation is straightforward, necessitating numerical optimization process for generating the equivalent petrophysical properties for the fracture grid.

6
Final Remarks

Brinkman equation is used to describe single and two-phase flows within highly heterogeneous porous media, where vugs are embedded within a porous matrix.

The single-continnum model is analyzed on two different scales. On the fine scale, the heterogeneous $1\phi1k$ Darcy model is used to determine the equivalent properties using the results obtained by Brinkman's modeling. In this case, the vug permeability K^{ϵ}_{Vug} is obtained through numerical computations to recover the equivalent permeability predicted by the Brinkman solution ($K^{eq}_{1\phi1k}$). In all cases, it was possible to find a K^{ϵ}_{Vug} value that minimized the error compared to the Brinkman model on the single-phase flow. The geometry and distribution of the vugs within the domain affect the optimal value of K^{ϵ}_{Vug}. For the vug configurations (a)-(c) and (e), setting an arbitrary high value does not result in significant errors. Nevertheless, for the configuration with a single vug aligned with the flow direction, the error was as high as 9 %. The micro tomography sample has a similar behavior to cases (a)-(c); however, K^{ϵ}_{Vug} has an asymptotic behavior that minimizes the error to an acceptable level. Considering two-phase flow, Brinkman and heterogeneous $1\phi1k$ model exhibits similar W_{cut} behavior for all vug configurations. Notwithstanding, a notable disparity arises in the pressure dynamics during two-phase flow between the Brinkman model and heterogeneous Darcy model. This divergence may be attributed to the fluid viscous dissipation within the vugs, not considered in the homogeneous Darcy model. Thus, the heterogeneous $1\phi1k$ Darcy model can not recover the results obtained on Brinkman model.

A homogeneous Darcy model is constructed through an optimization procedure to reproduce the complex two-phase flow through a vugular porous medium. Homogenization is effectively applied to all vug configurations except for configuration (d). Using appropriate equivalent absolute and relative permeability curves, the differences between the Brinkman model and the homogeneous Darcy model are minimized.

The Brinkman model exhibits significant disparities compared to the reference homogeneous $2\phi2k$ model for the case where there is a strong channelling effect. The homogenization of vugs yields significant differences from

the Brinkman model to the reference homogeneous $2\phi 2k$ Darcy model. These results show that arbitrarily setting the relative permeability as a $\times$-shape can lead to inaccurate results. Thus History Matching is necessary to obtain the equivalent relative permeability curves. To achieve homogenization in these cases, it is essential to develop equivalent permeability curves. Moreover, the equivalent relative permeability curves not only take into account the physical differences between the Stokes and the Darcy terms, but also the effects of flow through the intricate vug network. The great advantage of homogenization is that it reduces the complexity of the geometry of the vugs, which are treated through equivalent petrophysical properties. Fluid viscosity has effect on the determination of equivalent relative permeability curves since there are significant differences in relative permeability curves when fluid viscosity ratios vary.

For karstified and fractured media, the current modeling paradigm involves the emergence of the multi-porosity medium [115]. These models, however, introduces complexities not only by increasing degrees of freedom, given the presence of three or more porous media, but also by enhancing modeling uncertainty, which are result of the transfer functions that link matrix, fracture, and karst. It is possible that this increase in uncertainties could compromise the accuracy of the model. Moreover, the introduction of more degrees of freedom increases the computational expenses associated with these models.

In conclusion, Brinkman model can be used to establish equivalent properties for single-continuum and dual-continuum models. Single-continuum model are suitable to homogenize dispersed vugs in the porous matrix an vug configurations with low degree of channeling. On the other hand, dual-continuum are indicated for vug configurations with strong channeling. It is possible to determine properties such as absolute permeability and relative equivalent permeability by using more reliable data. By adopting this approach, the models can be improved in terms of accuracy and reliability.

6.1 Future Studies

As a recommendation for future studies, there are direct implications for reservoir engineers who require equivalent properties in their models. Further scientific investigations are needed to gain a more profound understanding of the physical phenomena associated with flow in highly heterogeneous porous media.

In practical applications, it is necessary to efficiently and accurately

generate equivalent properties. Machine learning models and convolutional neural networks [116] hold significant promise in this area. By leveraging a database of vuggy porous media images, these techniques can rapidly produce equivalent properties for everyday use. However, it's worthwhile to acknowledge that generating the initial data set poses a challenge due to the extensive computational time required for each scenario. This may be mitigated through some optimization.

Models that take into account the modeling of three-phase flows or compositional fluid models are highly relevant to pre-salt field scenarios, where the injection of CO_2-rich streams is common practice. As well as the extension to a 3-D model to capture gravitational effects. It is necessary to evaluate the modified IMPES method [117] to improve the code performance. Moreover, it is necessary to implement a effective tool to establish the Δt. Another possibility is to use parallel computing. FEniCS project has the possibility to easy implement parallel computing because this tool is readily available.

Another aspect worthy of attention is the interaction between flow phases within the free-flow region. While there has been an attempt to assess the existing literature on phase interaction in fractured media, it is noteworthy that references in this domain are scarce. Moreover, relying on the assumption that the velocity of each phase is directly proportional to its saturation is a simplification. To address this gap, a more comprehensive and refined literature review is essential, encompassing insights from other fields that investigate liquid-liquid phase interaction. The utilization of such models can be of immense value in offering a more detailed representation of flow dynamics within vugs. This is especially relevant to gas-liquid flows. Given the significantly higher mobility of gas than liquid, it is even more important to model this type of flow accurately. In order to integrate the nuances of the fine scale into the broader context of the coarse scale, homogenization theory can be regarded as an invaluable tool. As a result, it is essential to explore fine-scale models in more depth, in order to elucidate the underlying physics and integrate these features into coarse-scale models.

Bibliography

[1] EGGENWEILER, E.; RYBAK, I.. **Unsuitability of the beavers–joseph interface condition for filtration problems**. Journal of Fluid Mechanics, 892:A10, 6 2020.

[2] ILIEV, O.; LAPTEV, V.. **On numerical simulation of flow through oil filters**. Computing and Visualization in Science, 6:139–146, 3 2004.

[3] CHABANON, M.; VALDÉS-PARADA, F. J.; OCHOA-TAPIA, J. A. ; GOYEAU, B.. **Large-scale model of flow in heterogeneous and hierarchical porous media**. Advances in Water Resources, 109:41–57, 11 2017.

[4] MOSTHAF, K.; BABER, K.; FLEMISCH, B.; HELMIG, R.; LEIJNSE, A.; RYBAK, I. ; WOHLMUTH, B.. **A coupling concept for two-phase compositional porous-medium and single-phase compositional free flow**. Water Resources Research, 47, 10 2011.

[5] VERLEYE, B.; CROCE, R.; GRIEBEL, M.; KLITZ, M.; LOMOV, S.; MORREN, G.; SOL, H.; VERPOEST, I. ; ROOSE, D.. **Permeability of textile reinforcements: Simulation, influence of shear and validation**. Composites Science and Technology, 68:2804–2810, 10 2008.

[6] KHALED, A. R.; VAFAI, K.. **The role of porous media in modeling flow and heat transfer in biological tissues**. International Journal of Heat and Mass Transfer, 46:4989–5003, 2003.

[7] KHVATOVA, I.; RENAUD, A.; MALYUTINA, G.-B.; SANSIEV, G. ; KUZILOV, I.. **Simulation of Complex Carbonate Field: Double Media vs. Single Media Kharyaga Field Case**. All Days:SPE–160585–MS, 10 2012.

[8] PENG, X.; DU, Z.; LIANG, B. ; QI, Z.. **Darcy-stokes streamline simulation for the tahe-fractured reservoir with cavities**. SPE Journal, 14:543–552, 9 2009.

[9] DABBOUK, C.; ALI, L.; WILLIAMS, G. ; BEATTIE, G.. **Waterflood in vuggy layer of a middle east reservoir - displacement physics understood**. All Days, 10 2002.

[10] HERLINGER, R.; ZAMBONATO, E. E. ; ROS, L. F. D.. **Influence of diagenesis on the quality of lower cretaceous pre-salt lacustrine carbonate reservoirs from northern campos basin, offshore brazil**. Journal of Sedimentary Research, 87:1285–1313, 12 2017.

[11] ANP. **Boletim mensal de monitoramento da produção nacional de petróleo e gás natural**. https://www.gov.br/anp/pt-br/centrais-de-conteudo/publicacoes/boletins-anp/boletins/arquivos-bmppgn/2023/boletim-setembro.pdf, Acessado em: 19/11/2023.

[12] CHOQUEHE, P. W.; LITTLETON, L. C. P.. **Geologic nomenclature and classification of porosity in sedimentary carbonates**. The American Association of Petroleum Geologists Bulletin V, 54:207–250, 1970.

[13] WAYNE, M. A.; DAVID, A.; AUSTIN, B.; NATE, B. H.; TONY, S.; CLERKE, E. A.; KAIS, B.; KENNETH, H. J.; CHALLA, R. K. M.; HISHAM, Z. ; RAGHU, R.. **Confronting the carbonate conundrum**. 2005.

[14] POPOV, P.; EFENDIEV, Y. ; QIN, G.. **Multiscale modeling and simulations of flows in naturally fractured karst reservoirs**. Communications in Computational Physics, p. 162–184, 2009.

[15] YAO, J.; HUANG, Z.-Q.. **Fractured Vuggy Carbonate Reservoir Simulation**. Springer Berlin Heidelberg, Berlin, Heidelberg, 2017.

[16] BRINKMAN, H.. **A calculation of the viscosity and the sedimentation constant for solutions of large chain molecules taking into account the hampered flow of the solvent through these molecules**. Physica D: Nonlinear Phenomena, 13:447–448, 1947.

[17] QIN, G.; BI, L.; POPOV, P.; EFENDIEV, Y. ; ESPEDAL, M. S.. **An efficient upscaling process based on a unified fine-scale multi-physics model for flow simulation in naturally fracture carbonate karst reservoirs**. SPE, 6 2010.

[18] KROTKIEWSKI, M.; LIGAARDEN, I. S.; LIE, K. A. ; SCHMID, D. W.. **On the importance of the stokes-brinkman equations for computing effective permeability in karst reservoirs**. Communications in Computational Physics, 10:1315–1332, 2011.

[19] BARENBLATT, G.; ZHELTOV, I. ; KOCHINA, I.. **Basic concepts in the theory of seepage of homogeneous liquids in fissured rocks [strata]**. Journal of Applied Mathematics and Mechanics, 24:1286–1303, 1 1960.

[20] NICHOLS, G.. **Sedimentology and stratigraphy**. John Wiley & Sons, 2 edition, 2009.

[21] MEYERS, W. J.. **Paleokarstic Features in Mississippian Limestones, New Mexico**. Springer, 1 edition, 1988.

[22] QUADROS, F. B.. **Modelagem geológica numérica do sistema cárstico do lajedo arapuá, formação jandaíra, bacia potiguar**. Master's thesis, Pontifícia Universidade Católica do Rio de Janeiro, 2019.

[23] ZERFASS, H.; JUNIOR, F. C.. **Geologia estrutural em ambiente rúptil: fundamentos físicos, mecânica de fraturas e sistemas de falhas naturais**. Terrae Didatica, 7:61, 6 2015.

[24] FOSSEN, H.. **Structural Geology**, volumen 1. Cambridge University Press, 2nd edition, 2016.

[25] BEAVERS, G. S.; JOSEPH, D. D.. **Boundary conditions at a naturally permeable wall**. Journal of Fluid Mechanics, 30:197–207, 10 1967.

[26] BEAVERS GS, G.; SPARROW EM, E. ; MAGNUSON RA, R.. **Experiments on coupled parallel flows in a channel and a bounding porous medium**. J Basic Eng Trans ASME, 92 Ser D(4):843–848, Jan. 1970.

[27] TAYLOR, G. I.. **A model for the boundary condition of a porous material. part 1**, 12 1971.

[28] GOYEAU, B.; LHUILLIER, D.; GOBIN, D. ; VELARDE, M.. **Momentum transport at a fluid–porous interface**. International Journal of Heat and Mass Transfer, 46:4071–4081, 10 2003.

[29] ZHANG, Q.; PROSPERETTI, A.. **Pressure-driven flow in a two-dimensional channel with porous walls**. Journal of Fluid Mechanics, 631:1–21, 7 2009.

[30] LIU, Q.; PROSPERETTI, A.. **Pressure-driven flow in a channel with porous walls**. Journal of Fluid Mechanics, 679:77–100, 7 2011.

[31] SAFFMAN, P. G.. **On the boundary condition at the surface of a porous medium**. Studies in Applied Mathematics, 50:93–101, 6 1971.

[32] DAGAN, G.. **The generalization of darcy's law for nonuniform flows**. Water Resources Research, 15:1–7, 2 1979.

[33] RICHARDSON, S.. **A model for the boundary condition of a porous material. part 2**. Journal of Fluid Mechanics, 49:327–336, 9 1971.

[34] JONES, I. P.. **Low reynolds number flow past a porous spherical shell**. Mathematical Proceedings of the Cambridge Philosophical Society, 73:231–238, 1 1973.

[35] GRAY, W. G.; O'NEILL, K.. **On the general equations for flow in porous media and their reduction to darcy's law**. Water Resources Research, 12:148–154, 4 1976.

[36] WHITAKER, S.. **The Method of Volume Averaging**, volumen 13. Springer Netherlands, 1 edition, 1999.

[37] NEALE, G.; NADER, W.. **Practical significance of brinkman's extension of darcy's law: Coupled parallel flows within a channel and a bounding porous medium**. The Canadian Journal of Chemical Engineering, 52:475–478, 8 1974.

[38] OKABE, H.; BLUNT, M. J.. **Pore space reconstruction of vuggy carbonates using microtomography and multiple-point statistics**. volumen 43, 12 2007.

[39] GOLFIER, F.; LASSEUX, D. ; QUINTARD, M.. **Investigation of the effective permeability of vuggy or fractured porous media from a darcy-brinkman approach**. Computational Geosciences, 19:63–78, 2 2015.

[40] DALI, M. F.. **Flow in porous media with macropores using brinkman´s model**. Master's thesis, Pontifícia Universidade Católica Do Rio De Janeiro, 4 2019.

[41] CRUZ, R. F. M.. **Numerical evaluation of equivalent permeability in 3d vuggy porous media using brinkman model**. p. 1–97, 2020.

[42] COCLITE, G. M.; MISHRA, S.; RISEBRO, N. H. ; WEBER, F.. **Analysis and numerical approximation of brinkman regularization of two-phase flows in porous media**. Computational Geosciences, 18:637–659, 2014.

[43] BÜRGER, R.; KUMAR, S.; KUMAR, K. S. ; RUIZ-BAIER, R.. **Discontinuous approximation of viscous two-phase flow in heterogeneous porous media**. Journal of Computational Physics, 321:126–150, 2016.

[44] DINE, H. N. E.; SAAD, M.. **Analysis of a finite volume–finite element method for darcy–brinkman two-phase flows in porous media**. Journal of Computational and Applied Mathematics, 337:51–72, 2018.

[45] HALLACK, D. M. C.; CAVALCANTE FILHO, J. S. D. A. ; COUTO, P.. **Implementation of a Two-Phase Simulator Based on the Brinkman's Equation for Vuggy-Karstified Reservoirs**. volumen Day 2 Wed, October 30, 2019 de **Offshore Technology Conference Brasil**, p. D021S026R005, 10 2019.

[46] BELHAJ, H.; MUSTAFIZ, S.; MA, F. ; ISLAM, M. R.. **A new two phase extension of modified brinkman formulation for fluid flow through porous media**. p. 843–848. ASMEDC, 1 2005.

[47] ARMITI-JUBER, A.; ROHDE, C.. **On darcy- and brinkman-type models for two-phase flow in asymptotically flat domains**. Computational Geosciences, 23:285–303, 4 2019.

[48] ARMITI-JUBER, A.; ROHDE, C.. **Existence of weak solutions for a nonlocal pseudo-parabolic model for brinkman two-phase flow in asymptotically flat porous media**. Journal of Mathematical Analysis and Applications, 477:592–612, 9 2019.

[49] ARMITI-JUBER, A.. **On the limit of a two-phase flow problem in thin porous media domains of brinkman type**. Mathematical Methods in the Applied Sciences, 45:2563–2581, 3 2022.

[50] ELKADY, M.; ABDELAZIZ, G. B.; SHARSHIR, S. W.; MOHAMED, A. Y.; ELSAID, A. M.; EL-SAID, E. M.; MOHAMED, S. M.; ABDELGAIED, M. ; KABEEL, A.. **Non-darcian immiscible two-phase flow through porous materials (darcy–forchheimer–brinkman model)**. Thermal Science and Engineering Progress, 29:101204, 3.

[51] BHATTI, M.; ZEESHAN, A.; ELLAHI, R. ; SHIT, G.. **Mathematical modeling of heat and mass transfer effects on mhd peristaltic propulsion of two-phase flow through a darcy-brinkman-forchheimer porous medium**. Advanced Powder Technology, 29:1189–1197, 5 2018.

[52] KHAN, D.; ULLAH, S.; KUMAM, P.; WATTHAYU, W.; ULLAH, Z. ; GALAL, A. M.. **A generalized dusty brinkman type fluid of mhd**

free convection two phase flow between parallel plates. Physics Letters A, 450:128368, 10 2022.

[53] ARBOGAST, T.; BRUNSON, D. S.; AC, S. L. B. ; JENNINGS, J. W. D.. **A preliminary computational investigation of a macro-model for vuggy porous media**. Developments in Water Science, 55:267–278, 2004.

[54] ARBOGAST, T.; LEHR, H. L.. **Homogenization of a darcy–stokes system modeling vuggy porous media**. Computational Geosciences, 10:291–302, 9 2006.

[55] ARBOGAST, T.; GOMEZ, M. S. M.. **A discretization and multigrid solver for a darcy-stokes system of three dimensional vuggy porous media**. Computational Geosciences, 13:331–348, 9 2009.

[56] HUANG, Z.; YAO, J.; LI, Y.; WANG, C. ; LÜ, X.. **Permeability analysis of fractured vuggy porous media based on homogenization theory**. Science China Technological Sciences, 53:839–847, 3 2010.

[57] QIN, G.; BI, L.; POPOV, P.; EFENDIEV, Y. ; ESPEDAL, M. S.. **An efficient upscaling process based on a unified fine-scale multi-physics model for flow simulation in naturally fracture carbonate karst reservoirs**. SPE, 6 2010.

[58] GULBRANSEN, A. F.; HAUGE, V. L. ; LIE, K.-A.. **A multiscale mixed finite-element method for vuggy and naturally fractured reservoirs**. SPE Journal, 15:395–403, 6 2010.

[59] HE, J.; KILLOUGH, J. E.; FADLELMULA F., M. M. ; FRAIM, M.. **A Unified Finite Difference Model for The Simulation of Transient Flow in Naturally Fractured Carbonate Karst Reservoirs**. Day 2 Tue, February 24, 2015:D022S002R007, 02 2015.

[60] CAMPOS, D. V.. **Equivalência entre modelos de brinkman e de mono e duplo contínuo na representação do escoamento monofásico em meios porosos 2d carstificados**. Master's thesis, Pontifícia Universidade Católica Do Rio De Janeiro, 3 2022.

[61] HUANG, Z.-Q.; YAO, J. ; WANG, Y.-Y.. **An efficient numerical model for immiscible two-phase flow in fractured karst reservoirs**. Communications in Computational Physics, 13:540–558, 2 2013.

[62] YAN, X.; HUANG, Z.; YAO, J.; LI, Y. ; FAN, D.. **An efficient hybrid model for fractured-vuggy reservoir based on discrete fracture-vug network model**. 8 2016.

[63] WARREN, J.; ROOT, P.. **The behavior of naturally fractured reservoirs**. Society of Petroleum Engineers Journal, 3:245–255, 9 1963.

[64] KAZEMI, H.; MERRILL, L.; PORTERFIELD, K. ; ZEMAN, P.. **Numerical simulation of water-oil flow in naturally fractured reservoirs**. Society of Petroleum Engineers Journal, 16:317–326, 12 1976.

[65] THOMAS, L. K.; DIXON, T. N. ; PIERSON, R. G.. **Fractured reservoir simulation**. Society of Petroleum Engineers Journal, 23:42–54, 2 1983.

[66] GILMAN, J. R.; KAZEMI, H.. **Improvements in simulation of naturally fractured reservoirs**. Society of Petroleum Engineers Journal, 23:695–707, 8 1983.

[67] GILMAN, J. R.. **An efficient finite-difference method for simulating phase segregation in the matrix blocks in double-porosity reservoirs**. SPE Reservoir Engineering, 1:403–413, 7 1986.

[68] QUANDALLE, P.; SABATHIER, J. C.. **Typical features of a multipurpose reservoir simulator**. SPE Reservoir Engineering, 4:475–480, 11 1989.

[69] GILMAN, J.; KAZEMI, H.. **Improved calculations for viscous and gravity displacement in matrix blocks in dual-porosity simulators (includes associated papers 17851, 17921, 18017, 18018, 18939, 19038, 19361 and 20174)**. Journal of Petroleum Technology, 40:60–70, 1 1988.

[70] DEAN, R. H.; LO, L. L.. **Simulations of naturally fractured reservoirs**. SPE Reservoir Engineering, 3:638–648, 5 1988.

[71] SONIER, F.; SOUILLARD, P. ; BLASKOVICH, F. T.. **Numerical simulation of naturally fractured reservoirs**. SPE Reservoir Engineering, 3:1114–1122, 11 1988.

[72] COATS, K.. **Implicit compositional simulation of single-porosity and dual-porosity reservoirs**. SPE, 2 1989.

[74] UEDA, Y.; MURATA, S.; WATANABE, Y. ; FUNATSU, K.. **Investigation of the shape factor used in the dual-porosity reservoir simulator**. Society of Petroleum Engineers, 4 1989.

[74] FUNG, L. S.-K.. **Simulation of block-to-block processes in naturally fractured reservoirs**. SPE Reservoir Engineering, 6:477–484, 11 1991.

[75] ULEBERG, K.; KLEPPE, J.. **Dual porosity, dual permeability formulation for fractured reser- voir simulation**. 1996.

[76] LU, H.; BLUNT, M. J.. **General fracture/matrix transfer functions for mixed-wet systems**. SPE, 6 2007.

[77] DURLOFSKY, L. J.. **Upscaling of geocellular models for flow simulation**. European Association of Geoscientists & Engineers, 2004.

[78] CHRISTIE, M.. **Upscaling for reservoir simulation**. Journal of Petroleum Technology, 48:1004–1010, 11 1996.

[79] CARDWELL, W.; PARSONS, R.. **Average permeabilities of heterogeneous oil sands**. Transactions of the AIME, 160:34–42, 12 1945.

[80] KUMAR, A.; FARMER, C.; JERAULD, G. ; LI, D.. **Efficient upscaling from cores to simulation models**. SPE, 10 1997.

[81] WEN, X.-H.; GÓMEZ-HERNÁNDEZ, J.. **Upscaling hydraulic conductivities in heterogeneous media: An overview**. Journal of Hydrology, 183:ix–xxxii, 8 1996.

[82] RENARD, P.; DE MARSILY, G.. **Calculating equivalent permeability: a review**. Advances in Water Resources, 20:253–278, 10 1997.

[83] FARMER, C. L.. **Upscaling: a review**. International Journal for Numerical Methods in Fluids, 40:63–78, 9 2002.

[84] BARKER, J. W.; FAYERS, F. J.. **Transport coefficients for compositional simulation with coarse grids in heterogeneous media**. SPE Advanced Technology Series, 2:103–112, 4 1994.

[85] BARKER, J. W.; THIBEAU, S.. **A critical review of the use of pseudorelative permeabilities for upscaling**. SPE Reservoir Engineering, 12:138–143, 5 1997.

[86] CHEN, Y.; DURLOFSKY, L.; GERRITSEN, M. ; WEN, X.. **A coupled local–global upscaling approach for simulating flow in highly heterogeneous formations**. Advances in Water Resources, 26:1041–1060, 10 2003.

[88] ZHANG, P.; PICKUP, G. ; CHRISTIE, M.. **A new practical method for upscaling in highly heterogeneous reservoir models**. SPE Journal, 13:68–76, 3 2008.

[89] EVAZI, M.; JESSEN, K.. **Dual-porosity coarse-scale modeling and simulation of highly heterogeneous geomodels**. Transport in Porous Media, 105:211–233, 10 2014.

[90] RIOS, V. S.; SANTOS, L. O. S. ; SCHIOZER, D. J.. **Upscaling technique for highly heterogeneous reservoirs based on flow and storage capacity and the lorenz coefficient**. SPE Journal, 25:1981–1999, 8 2020.

[91] ROSA, A. J.; DE SOUZA CARVALHO, R. ; XAVIER, J. A. D.. **Engenharia de Reservatório de Petróleo**. Editora Interciência, 2006.

[92] BROOKS, R.; COREY, A.. **Hydraulic properties of porous media**. Hydrology Papers, 3:1–37, 1964.

[93] LOMELAND, F.; EBELTOFT, E. ; THOMAS, W. H.. **A new versatile relative permeability correlation**. 2005.

[94] BUCKLEY, S.; LEVERETT, M.. **Mechanism of fluid displacement in sands**. Transactions of the AIME, 146:107–116, 12 1942.

[95] MARTYS, N.; BENTZ, D. P. ; GARBOCZI, E. J.. **Computer simulation study of the effective viscosity in brinkman's equation**. Physics of Fluids, 6:1434–1439, 4 1994.

[96] LUNDGREN, T. S.. **Slow flow through stationary random beds and suspensions of spheres**. Journal of Fluid Mechanics, 51:273–299, 1 1972.

[97] KOPLIK, J.; LEVINE, H. ; ZEE, A.. **Viscosity renormalization in the brinkman equation**. The Physics of Fluids, 26:2864–2870, 10 1983.

[98] AURIAULT, J.-L.. **On the domain of validity of brinkman's equation**. Transport in Porous Media, 79:215–223, 9 2009.

[99] ROMM, E.. **Fluid flow in fractured rocks**. Nedra Publishing House, 1966.

[100] GIVLER, R. C.; ALTOBELLI, S. A.. **A determination of the effective viscosity for the brinkman–forchheimer flow model**. Journal of Fluid Mechanics, 258:355–370, 1 1994.

[101] PARK, J. S. R.; CHEUNG, S. W.; MAI, T. ; HOANG, V. H.. **Multiscale simulations for upscaled multi-continuum flows**. Journal of Computational and Applied Mathematics, 374:112782, 8 2020.

[101] SHELDON, J.; CARDWELL, W.. **One-dimensional, incompressible, noncapillary, two-phase fluid flow in a porous medium**. Transactions of the AIME, 216:290–296, 12 1959.

[102] ILIEV, O.; LAZAROV, R. ; WILLEMS, J.. **Variational multiscale finite element method for flows in highly porous media**. Multiscale Modeling and Simulation, 9:1350–1372, 10 2011.

[103] RIVIÈRE, B.. **Discontinuous Galerkin (DG) methods for Solving Partial Differential Equations**, volumen 1. Society for Industrial and Applied Mathematics, 1 edition, 2008.

[104] STONE, H.; GARDER, A.. **Analysis of gas-cap or dissolved-gas drive reservoirs**. Society of Petroleum Engineers Journal, 1:92–104, 6 1961.

[105] LOGG, A.; WELLS, G. N.. **Dolfin: Automated finite element computing**. ACM Trans. Math. Softw., 37(2), apr 2010.

[106] Logg, A.; Mardal, K.-A. ; Wells, G., editors. **Automated Solution of Differential Equations by the Finite Element Method**, volumen 84. Springer Berlin Heidelberg, 2012.

[107] DOUGLAS, J.; PEACEMAN, D. ; RACHFORD, H.. **A method for calculating multi-dimensional immiscible displacement**. Transactions of the AIME, 216:297–308, 12 1959.

[108] HUSSIEN, A. Z.. **The effect of vugy fractions on oil recovery factor and breakthrough time for two phase radial flow by mean of reservoir simulater**. p. 1–5. IEEE, 11 2012.

[109] NITSCHE, J.. **Über ein variationsprinzip zur lösung von dirichletproblemen bei verwendung von teilräumen, die keinen randbedingungen unterworfen sind**. Abhandlungen aus dem Mathematischen Seminar der Universität Hamburg, 36:9–15, 7 1971.

[110] MACHADO, M.; QUADROS, F.; BRITO, D. ; MORAES, R.. **Investigation of modeling options for numerical simulation of fractured and karstified reservoirs**. p. 1–5. European Association of Geoscientists and Engineers, 2020.

[111] KÖNNÖ, J.; STENBERG, R.. **H(div)-conforming finite elements for the brinkman problem**. Mathematical Models and Methods in Applied Sciences, 21:2227–2248, 11 2011.

[112] GEUZAINE, C.; REMACLE, J.-F.. **Gmsh: A 3-d finite element mesh generator with built-in pre- and post-processing facilities**. International Journal for Numerical Methods in Engineering, 79:1309–1331, 9 2009.

[113] CMG. **CMOST-AI User Guide: Intelligent optimization and analysis tool**, 2020.

[114] PICKUP, G. E.; SORBIE, K. S.. **The scaleup of two-phase flow using permeability tensors**. European Association of Geoscientists & Engineers, 1994.

[115] AIFANTIS, E. C.. **On the problem of diffusion in solids**. Acta Mechanica, 37:265–296, 9 1980.

[116] MOTTA, G.; DALI, M.; RIBEIRO, S. ; CARVALHO, M.. **Permeability prediction of karst porous media using convolutional neural networks**. 01 2022.

[117] CHEN, Z.; HUAN, G. ; LI, B.. **An improved impes method for two-phase flow in porous media**. Transport in Porous Media, 54:361–376, 3 2004.

A
Codes

A.1
Brinkman Two-Phase

```
from fenics import *
import time
import ufl
import os


class PiecewiseConstant(UserExpression):
    def __init__(self, values, markers, **kwargs):
        self._values = values
        self._markers = markers
        super().__init__(**kwargs)

    def eval_cell(self, values, x, cell):
        values[0] = self._values[self._markers[cell.index]]

    def value_shape(self):
        return tuple()


def tensor_jump(v, n):
    return ufl.outer(v, n)("+") + ufl.outer(v, n)("-")


def lmbdainv(s, mu_w, mu_o, no, nw):
    return 1.0 / ((s**nw) / mu_w + ((1.0 - s) ** no) / mu_o)


# Fractional flow function
def F(s, mu_rel, no, nw):
```

```
30      return s**nw / (s**nw + mu_rel * (1.0 - s) ** no)
31
32
33  def F_vugg(s):
34      return s
35
36
37  def mu_brinkman(s, mu_o, mu_w):
38      return s * mu_w + (1.0 - s) * mu_o
39
40
41  def BrinkmanIMPESGsmh(_folder_base, mu_w, mu_o, perm_darcy,
    ↪  dt):
42      dir1 = _folder_base + "/dir1"
43      dir2 = _folder_base + "/dir2"
44
45      try:
46          os.mkdir(dir1)
47      except OSError as error:
48          print(error)
49
50      try:
51          os.mkdir(dir2)
52      except OSError as error:
53          print(error)
54
55      mu = (mu_o + mu_w) / 2  # Pa.s
56      mu_b = (mu_o + mu_w) / 2  # Pa.s
57
58      mili_darcy = 9.86923e-16  # Porous media permeability
        ↪  convertion factor md [m2] (1 Darcy = E-12 m2)
59
60      k_matriz = perm_darcy * mili_darcy
61
62      kgf_cm2_to_Pa = 98066.5
63      pin = 2 * kgf_cm2_to_Pa  # Pa
64      pout = kgf_cm2_to_Pa  # Pa
65
66      dt = Constant(dt)  # s
```

```
67
68      phi = 0.2
69      mu_rel = mu_w / mu_o
70
71      sbar = Constant(1)
72
73      Kinv = Constant(1 / k_matriz)
74
75      mu = Constant(mu)
76      mu_b = Constant(mu_b)
77      t = 0
78      T = 5 * float(dt)
79
80      mesh = Mesh()
81      with XDMFFile(_folder_base + "/mesh/mesh.xdmf") as infile:
82          infile.read(mesh)
83
84      mvc = MeshValueCollection("size_t", mesh, 2)
85      with XDMFFile(_folder_base + "/mesh/domains.xdmf") as
        ↪  infile:
86          infile.read(mvc)
87      Markers = cpp.mesh.MeshFunctionSizet(mesh, mvc)
88
89      mvc = MeshValueCollection("size_t", mesh, 1)
90      with XDMFFile(_folder_base + "/mesh/boundaries.xdmf") as
        ↪  infile:
91          infile.read(mvc)
92      boundaries = cpp.mesh.MeshFunctionSizet(mesh, mvc)
93
94      order = 1
95      V = FiniteElement("BDM", mesh.ufl_cell(), order)
96      Q = FiniteElement("DG", mesh.ufl_cell(), order - 1)
97      R1 = FiniteElement("DG", mesh.ufl_cell(), order - 1)
98
99      Element = V * Q
100     W = FunctionSpace(mesh, Element)
101     R = FunctionSpace(mesh, R1)
102
103     (u, p) = TrialFunctions(W)
```

```
104     (v, q) = TestFunctions(W)
105
106     s = TrialFunction(R)
107     r = TestFunction(R)
108
109     U = Function(W)
110     (u_, p_) = U.split()
111     S = Function(R)
112     s0 = Function(R)
113
114     s0.vector()[:] = 0.0
115
116     # ============= DEFINITION OF SPATIALLY-VARYING PARAMETERS
        ↪  ======================
117     marker_inner = 1
118     marker_outer = 0
119
120     no_outer = 2
121     nw_outer = 2
122     no_inner = 1
123     nw_inner = 1
124
125     no = {marker_inner: no_inner, marker_outer: no_outer}
126     nw = {marker_inner: nw_inner, marker_outer: nw_outer}
127
128     VVV = FunctionSpace(mesh, "DG", 0)
129
130     noo = PiecewiseConstant(no, Markers)
131     noo_proj = project(noo, VVV)
132     nww = PiecewiseConstant(nw, Markers)
133     nww_proj = project(nww, VVV)
134
135     # ============ END DEFINITION OF SPATIALLY-VARYING
        ↪  PARAMETERS ===================
136
137     bc1 = DirichletBC(W.sub(0), Constant((1.0e-6, 0.0)),
        ↪  boundaries, 1)
138     bc2 = DirichletBC(W.sub(0), Constant((0.0, 0.0)),
        ↪  boundaries, 2)
```

```
    # # # bc3 = DirichletBC(VQ.sub(0), Constant((0.0, 0.0)),
    ↪ boundaries, 3)
    bc4 = DirichletBC(W.sub(0), Constant((0.0, 0.0)),
    ↪ boundaries, 4)

    bcs = [bc1, bc2, bc4]  # velocity BC

    ds = Measure("ds", domain=mesh, subdomain_data=boundaries)
    dx = Measure("dx", domain=mesh, subdomain_data=Markers)

    alpha = 35
    h = CellDiameter(mesh)
    h2 = ufl.Min(h("+"), h("-"))

    f = Constant((0.0, 0.0))
    n = FacetNormal(mesh)

    stab = (
        mu * (alpha / h2) * inner(tensor_jump(u, n),
        ↪ tensor_jump(v, n)) * dS
        - mu * inner(avg(grad(u)), tensor_jump(v, n)) * dS
        - mu * inner(avg(grad(v)), tensor_jump(u, n)) * dS
    )

    a = (
        mu_brinkman(s0, mu_o=mu_o, mu_w=mu_w) * inner(grad(u),
        ↪ grad(v)) * dx(1)
        + inner(v, lmbdainv(s0, mu_w, mu_o, no_outer, nw_outer)
        ↪ * Kinv * u) * dx(0)
        - div(v) * p * dx(1)
        - div(v) * p * dx(0)
        + div(u) * q * dx(0)
        + div(u) * q * dx(1)
        + stab
    )

    L = (
        inner(f, v) * dx(0)
        + inner(f, v) * dx(1)
```

```
        # - pin * dot(v, n) * ds(1)
        - pout * dot(v, n) * ds(3)
    )

    un = 0.5 * (inner(u_, n) + abs(inner(u_, n)))
    un_h = 0.5 * (inner(u_, n) - abs(inner(u_, n)))

    stabilisation = (
        dt("+") * inner(jump(r), jump(un * F(s0, mu_rel,
        ↪  noo_proj, nww_proj))) * dS
    )

    L3 = (
        phi * r * (s - s0) * dx(0)
        + r * (s - s0) * dx(1)
        - dt * inner(grad(r), F(s0, mu_rel, noo_proj, nww_proj)
        ↪  * u_) * dx(0)
        - dt * inner(grad(r), F_vugg(s0) * u_) * dx(1)
        + dt * r * F(s0, mu_rel, no_outer, nw_outer) * un * ds
        + stabilisation
        + dt * r * un_h * sbar * ds(1)
    )

    a_s, L_f = lhs(L3), rhs(L3)

    u_file = XDMFFile(dir2 + "/velocity.xdmf")
    p_file = XDMFFile(dir2 + "/pressure.xdmf")
    s_file = XDMFFile(dir2 + "/saturation.xdmf")

    step = 0
    parada = 1

    # while t < T:
    while step < 1e6:
        # ===
        _start_time = time.time()
        t += float(dt)
        solve(a == L, U, bcs)
        solve(a_s == L_f, S)
```

```
        s0.assign(S)

        if step % 2 == 0:
            p_file.write(p_, t)
            s_file.write(S, t)
            u_file.write(u_, t)

        step = step + 1
```

A.2 Darcy Two-Phase

```
from fenics import *
import time
import ufl
import os


class PiecewiseConstant(UserExpression):
    def __init__(self, values, markers, **kwargs):
        self._values = values
        self._markers = markers
        super().__init__(**kwargs)

    def eval_cell(self, values, x, cell):
        values[0] = self._values[self._markers[cell.index]]

    def value_shape(self):
        return tuple()


class Obstacle(SubDomain):
    def inside(self, x, on_boundary):
        return between(x[1], (0.3, 0.7)) and between(x[0],
        ↪  (0.3, 0.7))


def tensor_jump(v, n):
    return ufl.outer(v, n)("+") + ufl.outer(v, n)("-")
```

```
27
28
29  def lmbdainv(s, mu_w, mu_o, no, nw):
30      return 1.0 / ((s ** nw) / mu_w + ((1.0 - s) ** no) / mu_o)
31
32
33  # Fractional flow function
34  def F(s, mu_rel, no, nw):
35      return s ** nw / (s ** nw + mu_rel * (1.0 - s) ** no)
36
37
38  def DarcyIMPESRT(Nx, _folder_base, mu_w, mu_o, perm_darcy,
    ↪  perm_vugg, dt):
39
40      Ny = Nx
41      dir0 = _folder_base + "/Darcy_2_domai_RT"
42      dir1 = dir0 + "/dir1"
43      dir2 = dir0 + "/dir2"
44
45      try:
46          os.mkdir(dir0)
47      except OSError as error:
48          print(error)
49
50      try:
51          os.mkdir(dir1)
52      except OSError as error:
53          print(error)
54
55      try:
56          os.mkdir(dir2)
57      except OSError as error:
58          print(error)
59
60      mu = (mu_o + mu_w) / 2  # Pa.s
61
62
63      mili_darcy = 9.86923e-16  # Porous media permeability
        ↪  convertion factor md [m2] (1 Darcy = E-12 m2)
```

```
64
65      k_matriz = perm_darcy * mili_darcy
66      k_vugg = perm_vugg * mili_darcy
67
68      kgf_cm2_to_Pa = 98066.5
69      pin = 2 * kgf_cm2_to_Pa  # Pa
70      pout = kgf_cm2_to_Pa  # Pa
71
72      dt = Constant(dt)  # s
73
74      phi = 0.2
75      mu_rel = mu_w / mu_o
76
77      sbar = Constant(1)
78
79      Kinv_matriz = Constant(1 / k_matriz)
80      Kinv_vugg = Constant(1 / k_vugg)
81
82      mu = Constant(mu)
83
84      t = 0
85      T = 5 * float(dt)
86
87      mesh = mesh = UnitSquareMesh(Nx, Ny, "crossed")
88
89      order = 1
90      V = FiniteElement("RT", mesh.ufl_cell(), order)
91      Q = FiniteElement("DG", mesh.ufl_cell(), order - 1)
92      R1 = FiniteElement("DG", mesh.ufl_cell(), order - 1)
93
94      Element = V * Q
95      W = FunctionSpace(mesh, Element)
96      R = FunctionSpace(mesh, R1)
97
98      (u, p) = TrialFunctions(W)
99      (v, q) = TestFunctions(W)
100
101     s = TrialFunction(R)
102     r = TestFunction(R)
```

```
103
104     U = Function(W)
105     (u_, p_) = U.split()
106     S = Function(R)
107     s0 = Function(R)
108
109     s0.vector()[:] = 0.0
110
111     # ============= DEFINITION OF SPATIALLY-VARYING PARAMETERS
        ↪  =====================
112     marker_inner = 1
113     marker_outer = 0
114
115     no_outer = 2
116     nw_outer = 2
117     no_inner = 1
118     nw_inner = 1
119
120     obstacle = Obstacle()
121
122     Markers = MeshFunction("size_t", mesh,
        ↪  mesh.topology().dim())
123     Markers.set_all(marker_outer)
124     obstacle.mark(Markers, marker_inner)
125
126     no = {marker_inner: no_inner, marker_outer: no_outer}
127     nw = {marker_inner: nw_inner, marker_outer: nw_outer}
128
129     VVV = FunctionSpace(mesh, "DG", 0)
130
131     noo = PiecewiseConstant(no, Markers)
132     noo_proj = project(noo, VVV)
133     nww = PiecewiseConstant(nw, Markers)
134     nww_proj = project(nww, VVV)
135
136     boundaries = MeshFunction("size_t", mesh,
        ↪  mesh.topology().dim() - 1)
137
138     left = AutoSubDomain(lambda x: near(x[0], 0.0))
```

```
    right = AutoSubDomain(lambda x: near(x[0], 1.0))
    bottom = AutoSubDomain(lambda x: near(x[1], 0.0))
    top = AutoSubDomain(lambda x: near(x[1], 1.0))

    # Define boundary markers
    left.mark(boundaries, 1)
    top.mark(boundaries, 2)
    right.mark(boundaries, 3)
    bottom.mark(boundaries, 4)

    # =========== END DEFINITION OF SPATIALLY-VARYING PARAMETERS ===================

    bc1 = DirichletBC(W.sub(0), Constant((1.0e-6, 0.0)), boundaries, 1)
    bc2 = DirichletBC(W.sub(0), Constant((0.0, 0.0)), boundaries, 2)
    # # # bc3 = DirichletBC(VQ.sub(0), Constant((0.0, 0.0)), boundaries, 3)
    bc4 = DirichletBC(W.sub(0), Constant((0.0, 0.0)), boundaries, 4)

    bcs = [bc1, bc2, bc4]  # velocity BC

    ds = Measure("ds", domain=mesh, subdomain_data=boundaries)
    dx = Measure("dx", domain=mesh, subdomain_data=Markers)

    File(dir1 + "/domains.pvd") << Markers

    alpha = 35
    h = CellDiameter(mesh)


    f = Constant((0.0, 0.0))
    n = FacetNormal(mesh)


    a = (
```

```
        inner(v, lmbdainv(s0, mu_w, mu_o, no_inner, nw_inner) *
        ↪  Kinv_matriz * u) * dx(0)
        + inner(v, lmbdainv(s0, mu_w, mu_o, no_outer, nw_outer)
        ↪  * Kinv_vugg * u) * dx(1)
        - div(v) * p * dx(1)
        - div(v) * p * dx(0)
        + div(u) * q * dx(0)
        + div(u) * q * dx(1)

    )

    L = (
        inner(f, v) * dx(0)
        + inner(f, v) * dx(1)
        # - pin * dot(v, n) * ds(1)
        - pout * dot(v, n) * ds(3)
    )

    un = 0.5 * (inner(u_, n) + abs(inner(u_, n)))
    un_h = 0.5 * (inner(u_, n) - abs(inner(u_, n)))

    stabilisation = (
        dt("+") * inner(jump(r), jump(un * F(s0, mu_rel,
        ↪  noo_proj, nww_proj))) * dS
    )

    L3 = (
        phi * r * (s - s0) * dx(0)
        + r * (s - s0) * dx(1)
        - dt * inner(grad(r), F(s0, mu_rel, noo_proj, nww_proj)
        ↪  * u_) * dx
        + dt * r * F(s0, mu_rel, no_outer, nw_outer) * un * ds
        + stabilisation
        + dt * r * un_h * sbar * ds(1)
    )

    a_s, L_f = lhs(L3), rhs(L3)

    u_file = XDMFFile(dir2 + "/velocity.xdmf")
```

```
    p_file = XDMFFile(dir2 + "/pressure.xdmf")
    s_file = XDMFFile(dir2 + "/saturation.xdmf")


    step = 0

    while step < 1e5:
        # ===
        t += float(dt)
        solve(a == L, U, bcs)
        solve(a_s == L_f, S)
        s0.assign(S)
        if step % 50 == 0:
            p_file.write(p_, t)
            s_file.write(S, t)
            u_file.write(u_, t)

        step = step + 1
```

A.3 Stokes

This code is exclusively used for the validation of the Stokes model using the implementation of the BDM_1 basis functions as presented in section 3.6.2.

```
from dolfin import *
import ufl
import numpy as np
import matplotlib.pyplot as plt

Nx = 50
Ny = 400
# Load mesh and subdomains
mesh = UnitSquareMesh(Nx, Ny)
n = FacetNormal(mesh)

order = 1
V = FiniteElement("BDM", mesh.ufl_cell(), order)
Q = FiniteElement("DG", mesh.ufl_cell(), order - 1)
Element = MixedElement([V, Q])
```

```
W = FunctionSpace(mesh, Element)


boundaries = MeshFunction("size_t", mesh, mesh.topology().dim() - 1)
left = AutoSubDomain(lambda x: near(x[0], 0.0))
right = AutoSubDomain(lambda x: near(x[0], 1.0))
bottom = AutoSubDomain(lambda x: near(x[1], 0.0))
top = AutoSubDomain(lambda x: near(x[1], 1.0))

# Define boundary markers
left.mark(boundaries, 1)
top.mark(boundaries, 2)
right.mark(boundaries, 3)
bottom.mark(boundaries, 4)

ds = Measure("ds", domain=mesh, subdomain_data=boundaries)


bc2 = DirichletBC(W.sub(0), Constant((0.0, 0.0)), boundaries, 2)
bc4 = DirichletBC(W.sub(0), Constant((0.0, 0.0)), boundaries, 4)


# Collect boundary conditions
bcs = [bc2, bc4]

# Define variational problem
(u, p) = TrialFunctions(W)
(v, q) = TestFunctions(W)
f = Constant((0, 0))
mu = 1
pin = 10  # 1.0
pout = 0.0

alpha = 35
h = CellDiameter(mesh)
h2 = ufl.Min(h("+"), h("-"))
```

```
52
53
54  def tensor_jump(v, n):
55      return ufl.outer(v, n)("+") + ufl.outer(v, n)("-")
56
57
58  stab = (
59      mu * (alpha / h2) * inner(tensor_jump(u, n), tensor_jump(v,
        ↪  n)) * dS
60      - mu * inner(avg(grad(u)), tensor_jump(v, n)) * dS
61      - mu * inner(avg(grad(v)), tensor_jump(u, n)) * dS
62  )
63
64  nitche = (
65      alpha / h * inner(outer(v, n), outer(u, n)) * ds(2)
66      - inner(grad(u), outer(v, n)) * ds(2)
67      - inner(grad(v), outer(u, n)) * ds(2)
68      + alpha / h * inner(outer(v, n), outer(u, n)) * ds(4)
69      - inner(grad(u), outer(v, n)) * ds(4)
70      - inner(grad(v), outer(u, n)) * ds(4)
71  )
72
73  a = (
74      mu * inner(grad(u), grad(v)) * dx
75      - div(v) * p * dx
76      + div(u) * q * dx
77      + stab
78      + nitche
79  )
80  L = inner(f, v) * dx - pin * dot(v, n) * ds(1) - pout * dot(v,
    ↪  n) * ds(3)
81
82
83  # Compute solution
84  w = Function(W)
85  solve(a == L, w, bcs)
86
87  # Split the mixed solution using deepcopy
88  # (needed for further computation on coefficient vector)
```

```
89 (u, p) = w.split(True)
90
91 # Save solution in VTK format
92 ufile_pvd = File("u.pvd")
93 ufile_pvd << u
94 pfile_pvd = File("p.pvd")
95 pfile_pvd << p
```